**The Dissertation Committee for Yae In Cho Certifies that this is the approved version of the following dissertation:**

# Bioinspired Ligand Designs for Cobalt, Iron and Manganese Complexes: Understanding Mono-Iron Hydrogenase (Hmd)

**Committee:**

Michael J. Rose, Supervisor

Emily Que

Simon M. Humphrey

Jonathan L. Sessler

Benjamin K. Keitz

# Bioinspired Ligand Designs for Cobalt, Iron and Manganese Complexes: Understanding Mono-Iron Hydrogenase (Hmd)

**by**

**Yae In Cho**

**Dissertation**

Presented to the Faculty of the Graduate School of

The University of Texas at Austin

in Partial Fulfillment

of the Requirements

for the Degree of

**Doctor of Philosophy**

**The University of Texas at Austin**

**May 2018**

# Dedication

For my parents, Dr. Lee and Dr. Cho.

# Acknowledgements

I would first like to deeply thank Prof. Michael J. Rose, who has been a wonderful mentor not only as a scholar, but also as someone who has already been through it all. He never hesitated to help me overcome any struggles I had by sharing his own experience and opinion. It was a great privilege to be his first student.

I was fortunate to be part of such a supporting and fun group, and the friends I made here will be my dear friends for the rest of my life. I also thank Meredith for her passionate work on the fluoride(s)-bridged dicobalt project as an undergraduate researcher, which was a great experience for both of us as a mentor and mentee.

Within the Department of Chemistry, I appreciate the help from the technical staffs, Vince, Angela and Steve, for their expertise in X-ray diffraction and NMR spectroscopy, as well as the administrative staff, Betsy, for her indispensable role for graduate students.

I thank my lovely friends, Jihee, Soohyun and Sunkyong, for their beautiful and artistic inspirations through our journey towards a PhD together in God's love; Sunmin and Leehyun for being the best roommates during my time in Austin. I would like give special thanks to Jason for being my chemistry chalkboard, a flower fairy and other half.

Last but not least, I am grateful for my parents who have been the greatest support from the furthest.

# Bioinspired Ligand Designs for Cobalt, Iron and Manganese Complexes: Understanding Mono-Iron Hydrogenase (Hmd)

Yae In Cho, PhD.

The University of Texas at Austin, 2018

Supervisor: Michael J. Rose

Mono-iron hydrogenase is one of three types of hydrogenases, catalyzing reversible hydride transfer to the substrate (methenyl-$H_4MPT^+$) by heterolytically cleaving molecular hydrogen into a proton and a hydride. The key features of the enzyme's active site include a pyridone moiety, an acyl unit and facial ligation of $C^{acyl}N^{pyridone}S^{Cys}$ donors. Each feature was independently incorporated into a selected ligand system (Schiff-base N4, pincer and thianthrene scaffold, respectively), in efforts to *i)* develop possible bioinspired catalysts for $H_2$ activation using earth abundant metals (iron, cobalt, manganese) and *ii)* make synthetic models of the enzyme active site for deeper understanding of the architecture of the active site and catalytic mechanism. Synthetic routes for making pyridone-based Schiff-base N4 and NNS type ligands were explored: although not isolated, the ligands were spectroscopically detected. On the other hand, the simpler version—pyridine-based Schiff-base N4 ligands—afforded dinuclear cobalt complexes upon metalations with cobalt(II) precursors. Depending on the length of the diamine-linker as well as the substituents on the pyridine rings, either spontaneous $O_2$ activation or B–F activation was observed, yielding $\mu$-peroxo dicobalt(III) complexes or $\mu$-fluoride bridged dicobalt(II) complexes, respectively. In particular, two $\mu$-fluoride bridged dicobalt complexes showed antiferromagnetic coupling between the two cobalt(II) centers. From the pincer ligands

featuring the unique acyl moiety within $C^{acyl}N^{pyridine}S^{thioehter}$ and $C^{acyl}N^{pyridine}P^{Ph2}$ donor set, the (expected) meridional and an (unexpected) facial iron-acyl complexes were isolated, respectively. Upon deprotonation (pyridine→pyridinate dearomatization), both complexes showed reactivity towards $H_2$ activation; no evidence for hydride-transfer was observed. For the facial ligation, thianthrene-scaffolded manganese system was examined as a more flexible version of the anthracene-scaffolded systems. Preliminary results of the kinetic studies support the correlation between the flexibility of the scaffold and the reactivity of the metal complex, without greatly altering the electronic environment of the metal center.

# Table of Contents

# List of Tables

# List of Figures

# List of Schemes

# Chapter 1: Introduction

## 1.1 Hydrogen Activation

### 1.1.1 Nature of Hydrogen

Hydrogen is the lightest and most abundant element in the universe.[1] On earth, hydrogen is found mostly as part of compounds such as hydrocarbons and water, rather than as $H_2$ gas.[2] Molecular $H_2$ has a strong covalent bond of 103 kcal/mol[3] and is unreactive under ambient temperature and pressure.

About 50 million tons ($260 B, 2006) of $H_2$ is annually *produced* from industrial processes (steam methane reformers, partial oxidation of heavy hydrocarbon fractions, coal/biomass gasification, water electrolysis etc.).[1] Separately, $H_2$ is *used* in industry primarily for hydrogenation reactions using precious metals (for example, platinum and ruthenium for ketone hydrogenation[4,5]). More recently, scientists began to consider using $H_2$ as energy carrier for fuel cells and combustion engines for transportation.[1,2]

### 1.1.2 Utilizing Hydrogen

Figure 1.1 shows the transition of the global energy systems from solid- and liquid-based energy system in the past to more gases-based energy system in the future over the span of 300 years.[6] Hydrogen gas is considered as a sustainable "green" fuel that is environmentally and climatically clean.[1] The only byproduct of $H_2$ combustion is $H_2O$, and $H_2O$ can be electrolyzed into $O_2$ and $H_2$ for the reverse reaction. Therefore, it is free of $CO_2$ emission, avoiding greenhouse effects, unlike the case of conventional fossil fuels.[1] In addition, hydrogen is ubiquitous from the geographical point of view, meaning that no nation or continent is excluded from being a hydrogen producer, hydrogen trader, or hydrogen user.[1] Moreover, shifting from a carbon-rich coal and fossil fuel energy economy to a hydrogen-rich energy economy supports the dematerialization process.[1] (Figure 1.2)

Simply comparing the molar mass of hydrogen versus carbon (1.008 versus 12.01 g/mol, respectively) explains how using hydrogen can help dematerialize the energy system. For these reasons, hydrogen is considered to be the fuel of the future.[7]

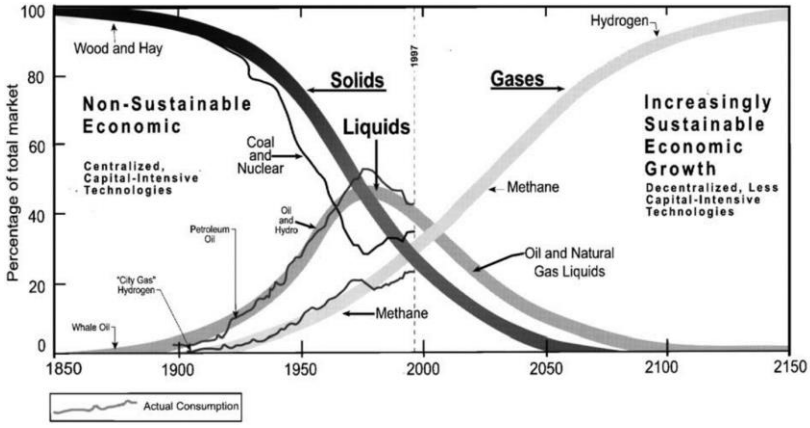


Figure 1.1: The age of energy gases: global energy systems transition.[6]

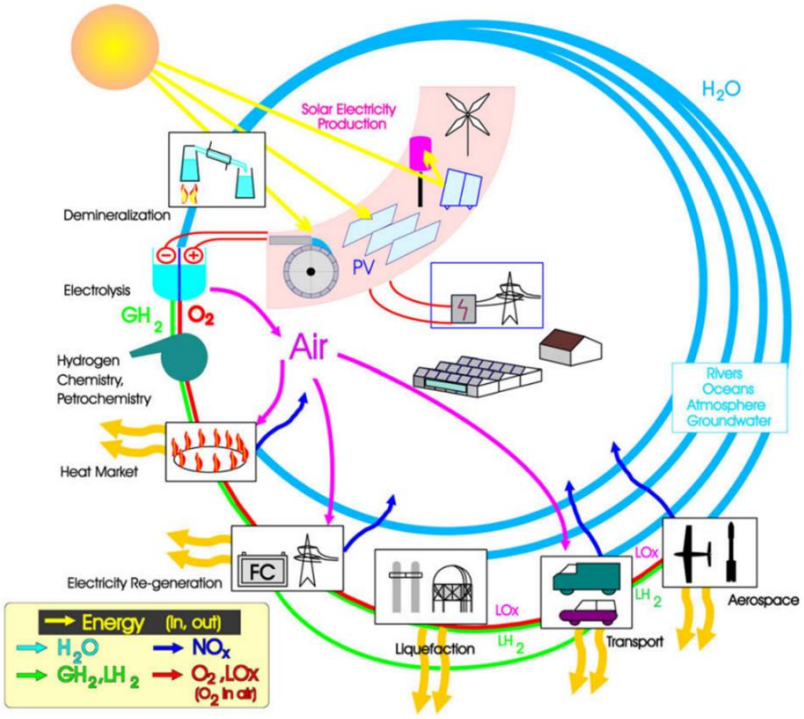


Figure 1.2: Materially closed hydrogen energy systems.[1]

However, the main disadvantage of utilizing hydrogen is its low density. Despite having the highest energy content per weight (120 MJ/kg) among common fuels, the energy density of molecular hydrogen is quite low—only 0.0108 MJ/L.[8] This raises the importance of devising a safe and efficient system to handle and store hydrogen gas.

As one way of storing $H_2$, chemical hydrogen storage methods have been investigated. These methods utilize storage mediums such as metals (as metal hydrides, metal hydride alloys,[9] metal borohydrides[10]) and chemical compounds (cyclohexanes and heterocycles,[11] ammonia,[12] hydrazine and amine boranes,[13,14] formic acid[15–17] and alcohols[18]) through covalently binding hydrogen. Using formic acid as a hydrogen storage medium, for example, conventionally involves complexes of the platinum group metals such as ruthenium, rhodium, iridium.[8] However, more recent studies on non-noble-metal-based catalysts showed that nickel[19], iron[20], cobalt[21], copper[22] catalysts with phosphine and nitrogen donor ligands (including pincer ligands) exhibit comparable catalytic reactivity.[8] For the release of hydrogen, thermal or catalytic decomposition of the carrier is used.[8]

As Blaser described, "Hydrogen is the cleanest reducing agent and hydrogenation is the most important catalytic method in synthetic organic chemistry both on the laboratory and the production scale."[4] Because the two hydrogen atoms are held together by a strong two-electron H–H bond, activating (splitting or the bond cleavage process) the bond in a controlled manner is the key point in utilizing $H_2$.[7] This process could be assisted by transition metal(s), and much research on understanding the mechanism of $H_2$ binding to the metals and further reactivity has been investigated for a several decades in the field of organometallic chemistry.[3,7] For designing effective homogenous hydrogenation catalysts, each of the following components of the catalyst should be considered: a central metal ion assisted by one or more (chiral) ligands plus anions with ability to activate $H_2$, then transfer the two H atoms to an acceptor(s).[4] In general, low valent ruthenium, rhodium and iridium

complexes with tertiary chiral phosphorous ligands have shown to be the most active and versatile catalysts.[23–25]

### 1.1.3 Inspirations from Biological Systems

Recently, the research climate has been shifted to look for the methods to replace precious metals (usually the coinage group metals: ruthenium, rhodium, palladium, osmium, iridium, and platinum) with earth abundant metals in the process of $H_2$ activation/production.[26–28] Due to the limited supply of precious metals and lanthanides, as well as their expensive cost, inexpensive first-row transition metals—such as titanium, manganese, iron and zinc—have been taking the spotlight as the next generation ingredients for catalytic process in industry.[29–32]

It is reasonable to take nature's perspective: metalloproteins utilize earth-abundant metals, rather than precious metals such as palladium or platinum for $H_2$ activation catalysis. Indeed, Morris reported iron complexes used in place of platinum and ruthenium for catalysis such as asymmetric hydrogenation, transfer hydrogenation, hydrosilylation of ketones.[5] More specifically for bioinorganic chemists, the active site of a metalloprotein provides inspirations for designing artificial biomimetic catalysts.[33,34]

Nature has found the way to utilize molecular hydrogen as an energy source by using enzymes, namely, the hydrogenases in microorganisms. The environment of hydrothermal vents in ocean basins near volcanically active areas exhibits extreme conditions—it is anoxic, carbon dioxide- and hydrogen-rich, no light, moderately high temperature (28-90 °C compared to ambient water temperature of 2 °C at similar depths), high pressure environment replete with sulfur-containing minerals (sulfides of metals like iron, copper, zinc) and even hydrogen sulfide, which is very toxic to most known organisms.[35] Although these conditions may seem too extreme for life, it is home for

secluded ecosystems supported by hydrogen-driven subsurface microbial communities. One example is an active deep-sea hyperthermal field called "HyperSLiME (hyperthermophilic subsurface lithoautotropic microbial ecosystem)", located in the Central Indian Ridge.[36] Since this distinctive environment resembles the early Earth[37] to some extent, some researchers postulate that these hydrothermal fields are considered to be the origin of the earth's first metabolic cycles.[38]

### 1.2 HYDROGENASES ($H_2$ASES)

Hydrogenases ($H_2$ases) are a group of metalloenzymes that are found in a wide range of microorganisms (such as prokaryotic microbes to eukaryotic protozoa and fungi) and catalyze the activation of molecular hydrogen into protons and electrons, as well as the reverse reaction of dihydrogen generation.[39–42] These enzymes utilize earth-abundant transition metals such nickel and/or iron to perform the reversible $H_2$ conversion catalysis (heterolytic splitting and heterogenesis of $H_2$, forward and reverse reactions in Eq 1.1, respectively) in efficient ways.[2,43]

$$H_2 \leftrightarrow H^+ + H:^- \leftrightarrow 2H^+ + 2e^- \qquad \text{(Eq 1.1)}$$

#### 1.2.1 [NiFe] and [FeFe] Hydrogenases

Three known types of hydrogenases are known (see Figure 1.3), and all three types contain at least one iron metal center. Among those three, the two enzymes that were first discovered first are the [NiFe] and [FeFe] hydrogenases. These two bimetallic hydrogenases convert $H_2$ into two protons and 2 electrons[43] (all the way to the right in Eq 1.1) and have several common characteristics of the active site.[43] Based on the crystal structures of [NiFe][44–48] and [FeFe][49,50], both enzymes have two subunits of different sizes, bearing the active site deeply buried at the center of the enzyme. In both cases, the iron atoms are ligated by small inorganic ligands such as CO and $CN^-$. The two metal centers

are held in place with two bridging sulfides. Several cubical iron-sulfur clusters (shown as [4Fe-4S] and [3Fe-4S]) are located on or near the bimetallic center, serving as electron transfer chain to shuttle electrons to the metal center. During catalysis, at least one of the metal centers changes its oxidation state (Ni(II)↔Ni(III) in [NiFe] and Fe(I)↔Fe(II) in [FeFe] hydrogenase), rendering it the 'redox-active' center.

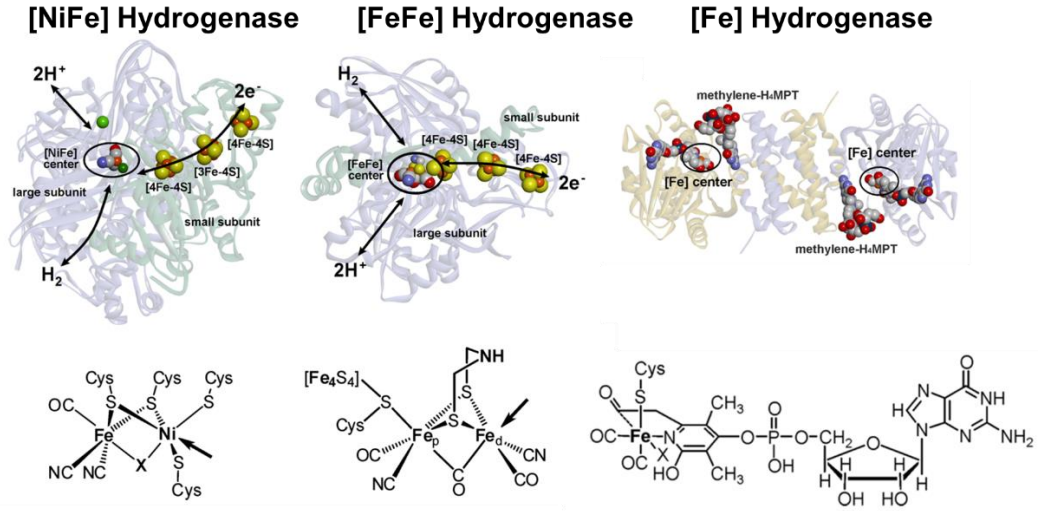


Figure 1.3: X-ray structures of [NiFe], [FeFe] and [Fe] hydrogenase (top row) and the chemical structure of the active site in each enzyme (bottom row). An arrow in [NiFe] and [FeFe] hydrogenases indicates the open metal coordination site.[51]

### 1.2.2 [Fe] Hydrogenase (Hmd)

The third type, [Fe] hydrogenase, is found in methanogenic archaea, but only under nickel-deficient environment.[52] During methanogenesis (methane generation via reduction of carbon dioxide with $H_2$), it catalyzes an intermediate step that reversibly reduces the substrate methenyltetrahydromethanopterin (methenyl-$H_4MPT^+$) by heterolytically cleaving $H_2$ into a proton and a hydride (Scheme 1.1).[52] This hydride is then transferred to the substrate to produce methylene-$H_4MPT$ and a proton as the products. Therefore, the net reaction for $H_2$ is a heterolytic cleavage into a proton and a hydride[2] (middle reaction in Eq

1.1). The presence of methenyl-$H_4MPT^+$ substrate absolutely dictates the catalytic activity of the enzyme.[53] Based on this catalysis, [Fe] hydrogenase is also named as Hmd, which stands for $H_2$-forming methylene-tetrahydromethanopterin dehydrogenase.

In contrast to [NiFe] and [FeFe] hydrogenases, Hmd is a homodimer with two identical subunits, each having only one iron(II)-centered active site. Hmd is free of Fe-S clusters, only having one cysteine-sulfur in the active site. The iron center is redox-inactive, keeping its oxidation state as Fe(II) during catalysis. It is also EPR-silent, which initially led to the mischaracterization of Hmd as a 'metal-free' hydrogenase.[54,55] However, Mössbauer spectroscopy revealed a diamagnetic iron center (either Fe(0) or Fe(II), but the latter being more conceivable as the enzyme can bind $CN^-$ reversibly)[56], and the X-ray structures revealed the details of the active site, in which the iron center with unique donor moieties is present.[2,55,57–59]

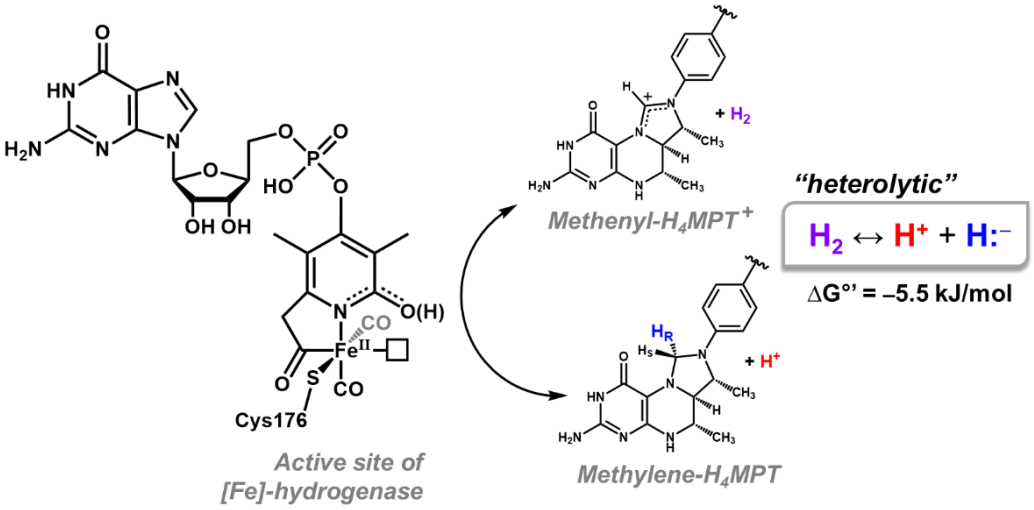


Scheme 1.1: Reversible reduction of the substrate methenyl-$H_4MPT^+$ catalyzes by Hmd with $H_2$, producing methylene-$H_4MPT$ and a proton.

In the active site of [Fe] hydrogenase, the Fe(II) center is ligated with a Cys176-sulfur, cis carbonyl ligands, an $sp^2$-nitrogen and an acyl carbon from the iron-guanylylpyridinol/pyridone(FeGP)-cofactor.[54,55,57,58,60–63] The Cys176-sulfur is the only proteinaceous donor directly linked to the protein. The rest of the sites are the exogenous CO's (2011, 1944 $cm^{-1}$ in IR spectrum[60]), an open coordination site for $H_2$ or solvent ($H_2O$) to bind, and the pyridone-acyl chelate. It is notable that the acyl unit as metal ligand very rare in nature, the only example reported so far being a possible intermediate in the reaction of a nickel-based acetyl-CoA synthase/decarbonylase.[64,65]

It is worth noting on the binding geometry of each donor atom/moiety, as it reflects the nature's thoughtful decision of locating certain moiety at certain position for the best performance of the enzyme in catalysis. Although the pyridone oxygen does not directly participate in the ligation to the metal center, it is positioned directly towards the open coordination site where $H_2$ and methenyl-$H_4MPT^+$ substrate would bind, and the hydride transfer occurs. This emphasizes the critical role of pendant base in the catalytic mechanism. Also, $C^{acyl}N^{pyridone}S^{Cys176}$ unit is bound to Fe(II) in a facial motif, in addition to the substrate binding site located trans to the acyl moiety. These moieties are arranged in such a meticulous way: scientists are responsible for understanding the intentions of the nature, and thus the overall mechanism of the catalysis. Especially, synthetic bioinorganic chemists can examine the nature's unique design of [Fe] hydrogenase by studying synthetic models of the enzyme.

### 1.3 Ligand Design Strategy for Bioinspired Model Systems

One of the several objectives of our research group is to make bioinspired catalysts using earth-abundant transition metals with meticulously designed ligands containing certain features of enzyme active sites. The Hydrogenase subgroup focus on mimicking, and thus, understanding the role of the components that the active site of [Fe] hydrogenase holds. Therefore, at this stage of investigation, we focused on selecting a few key features of Hmd active site to be implemented in ligand design. The features that are focused on separately as independent projects within this thesis include *i)* the pyridone moiety, *ii)* the acyl unit, and *iii)* the facial ligation of a ligand using a scaffold system. (Figure 1.4) All of these topics are discussed in detail in the following chapters. Ideally, the information gathered from both the successful achievements and the failures will help build more profound understanding of the Hmd system, and thus, the design of more sophisticated bioinspired catalysts in the future.

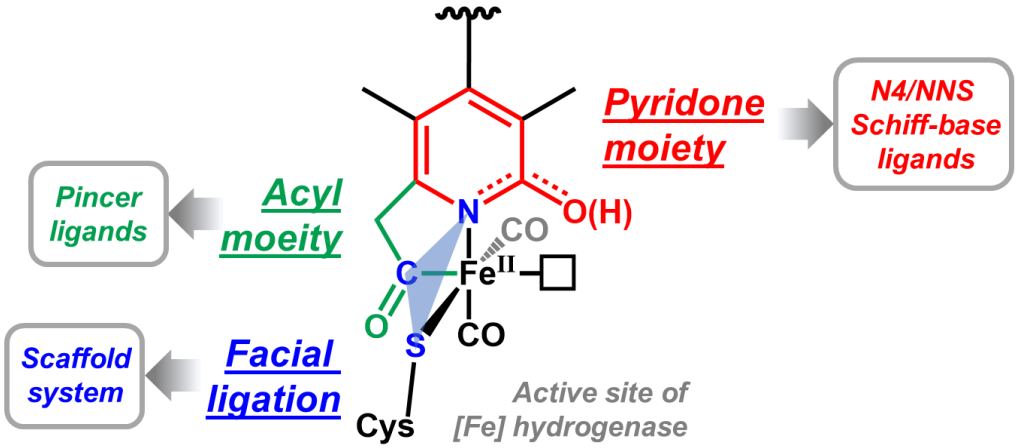


Figure 1.4: The features of Hmd active site that were implemented in ligand designs as independent projects within this dissertation.

### 1.3.1 Schiff-Base N4 Ligands

Our original intention of this project was to synthesize a variety of pyridone-based Schiff-base N4 ligands and their corresponding monomeric cobalt complexes to evaluate the role of the pyridone moiety as a proton shuttle in the known cobalt-N4 catalytic platform such as cobaloximes[66–68] and salcomines[69] (Figure 1.5). These complexes have either N4- or N2O2-donor system within their ligand(s), coordinating to a mononuclear cobalt center. A number of cobaloximes have been studied as model complexes of vitamin B12, whereas salcomine as a possible $O_2$ carrier. From more broader perspective, a good example of iron-N4 system is the active site of hemoglobin, exhibiting an iron center with N4-donating heme.

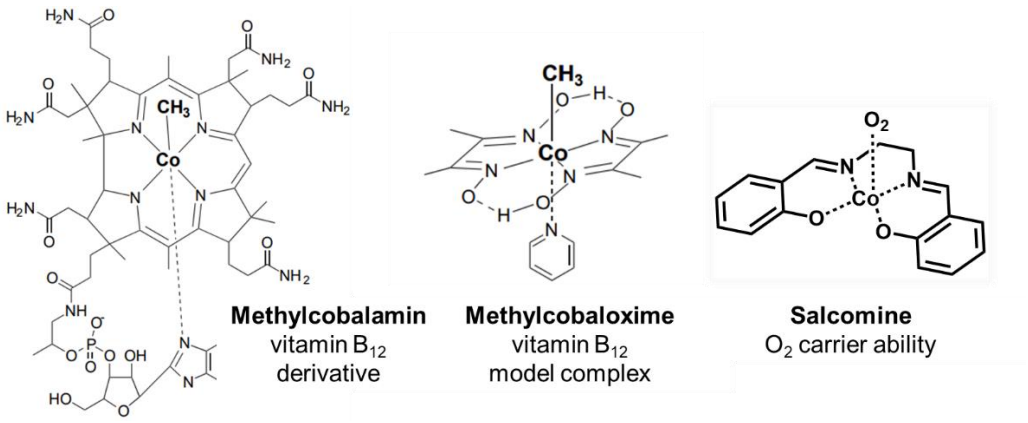


Figure 1.5: Examples of cobalt-N4 or cobalt-N2O2 systems.

Having these examples in mind, a variety of *pyridine*-based Schiff-base N4-type ligands were synthesized (before making the pyridone-based ligands) by condensation reaction of primary diamines (ethylenediamine or *o*-phenylenediamine) with substituted pyridinecarboxaldehyde/ketones (Scheme 1.2). Two nitrogen donors from diamine and two from two pyridines makes a four-N-donor chelate. The substituents $R^1$ and $R^2$ as well as the phenyl group on the diamine were placed with the intention for mononucleation.

These series of pyridine-based ligands were synthesized as rehearsals for making more sophisticated N4-type ligands containing two pyridone moieties to check the viability of the complexation/metalation of cobalt metal. The Schiff-base condensation was chosen for its facile synthetic procedure that was suitable for introductory laboratory learning experience at the beginning of our project.

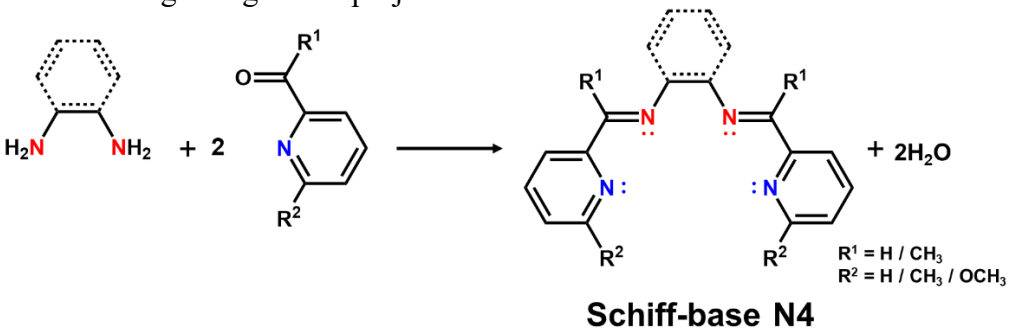


Scheme 1.2: General reaction scheme for synthesizing pyridine-based Schiff-base N4 ligands via condensation reaction.

The reaction of these Schiff-base N4 ligands with cobalt salts gave unexpected results: rather than forming monomeric cobalt complexes, dinuclear cobalt complexes were synthesized via either spontaneous $O_2$ activation (forming $\mu$-peroxo bridge[70], Chapter 2) or spontaneous B–F activation (forming $\mu$-F bridge(s)[71], Chapter 3). Although these dinuclear cobalt complexes were not the desired complexes, their structural, spectroscopic and magnetic properties proved worth of investigation.

### 1.3.2 Pyridone-N4/NNS Ligands

As the pyridine-based Schiff-base N4 ligand project was progressing, attempts to incorporate the pyridone moiety were carried out in parallel. Similar to the pyridine versions described in Section 1.3.1, a Schiff-base condensation reaction was utilized to synthesize the pyridone-N4 ligands (exhibiting two pyridone moieties in symmetric fashion) using pyridone-aldehydes, as well as the asymmetric NNS-type ligands featuring one pyridone group with one methylthioether (-SMe) group from the primary amine (Scheme 1.3).

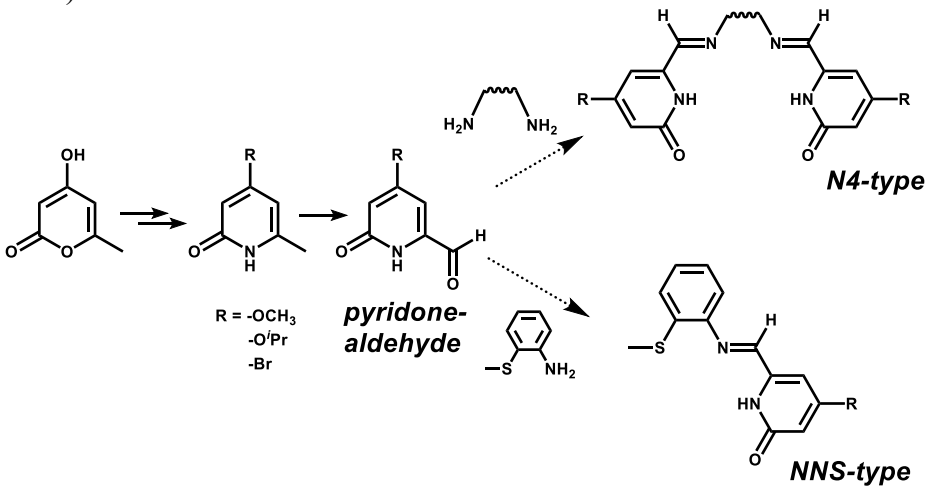


Scheme 1.3: General reaction scheme for synthesizing pyridone-N4/NNS ligands via Schiff-base condensation reaction of pyridone-aldehyde and a choice of primary amine.

This project was partially successful, only detecting the N4 and NNS ligands in $^{1}$H NMR spectra without a clean isolation. It is likely due to the strong intramolecular hydrogen bonding interactions between the pyridone-NH and pyridone-C=O. However, the experimental procedures for the key synthon, pyridone-aldehyde, were discovered. This insight is beneficial for future projects employing the pyridone moiety. The detailed experimental procedures are included in Appendix A.

### 1.3.3 Pincer Ligands

Pincer ligands are one important class of various chelates. In general, a pincer ligand binds to a metal center in tridentate meridional fashion transition metal, forming 2 five- (or sometimes six-) membered metallocyclic rings (Figure 1.6).[72–74] Based on their strong chelating ability that prevents ligand dissociation, a wide variety of pincer ligands has been strategically utilized in the field of inorganic and organometallic chemistry.[73] For studying the catalytic activities/applications for iron systems[72,75–85] or for synthetically modelling the Hmd active site[86,87], various pyridine-based pincer ligands have been investigated.

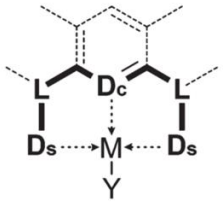


**L** = $NH, CH_2, O$
**Dc** = N, C
**Ds** = $PR_2$, NR, $P(OR)_2$, ...
**M** = Ru, Pd, Pt, Fe, Mo, Ni, ...
**Y** = NCMe, CO, Br, Cl, H,...

Figure 1.6: Generalized structure of pincer complexes.[72]

As mentioned earlier in Section 1.3 (Figure 1.4), the acyl moiety is a unique feature of the Hmd active site, not found in any other metalloenzyme active site, other than as an intermediate in acetyl-CoA synthase.[58] Employing the tunability of pincer ligands, the acyl unit was incorporated into the pyridine-based pincer ligand system using 2-methyl pyridine group, which is later in-situ activated into an acyl group upon metalation, forming an iron-acyl bond through acylmethylpyridinyl unit. The synthetic route for iron-acyl complexes using methylpyridinyl ligand was largely inspired by the works of Xile Hu and coworkers,[88] similar to the Fischer route for metal-acyl generation.[89]

In addition to the acyl unit, the a sulfur donor in the active site of Hmd as cystein-thiolate was imposed on the other side of the pincer ligand as a thioether (-SMe), which is chosen for its effective prevention of the $\mu_2$-thiolato bridging motif and S-S dimerization. The related work on iron-acyl-pincer complexes are discussed in Chapter 4.

### 1.3.4 Scaffold System

For bioinorganic chemists designing molecular catalysts and/or biomimicking enzyme active sites, a rigid scaffold has been used as a platform for orienting multidentate ligands in specific binding geometries to achieve particular a metal-binding motif. In addition, it has an ability to introduce different functional groups by changing substituents for the desired primary coordination environment on the metal center in terms of both geometric and electronic control.[90] For example, cuboidal [$Fe_3S_4$] clusters by Holm utilized a trisubstituted benzene bearing three thiolate donors as an scaffold.[91] And a triptycene-based scaffold by Lippard was used for modeling the diiron active site of monooxygenase.[92] Trans-spanning bidentate diphosphine scaffolds were studied for nickel/palladium/rhodium catalysts by Gelman (triptycene and anthracene),[93,94] Lu (dibenzofuran)[95,96] and van Leeuwen (xanthene).[97–99] (Figure 1.7)

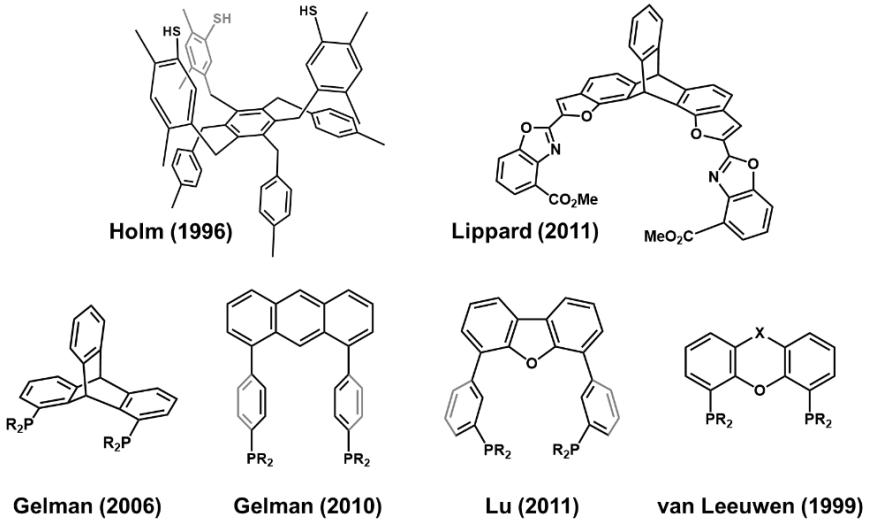


Figure 1.7: Examples of the known scaffolds.[91–99]

In our research group, an anthracene scaffold has been a successful framework for enforcing facial ligation of the donor atoms to iron or manganese centers ($C^{acyl/cabamoyl}$, $N^{pyridine/pyridone}$ and $S^{thiolate/thioether}$ or $P^{phosphine}$).[100–102] The target anthracene-scaffolded ligand

would have two different functionalized phenyl groups on the 1- and 8-positions on the anthracene to arrange201 an asymmetric tridentate (*p*-$C^{acyl}$ and *m*-$N^{pyridone}$ from one group, *m*-$S^{thiolate}$ from the other) with optimal space between the donor atoms (3.03–3.84 Å) for it to bind iron or manganese in facial mode. (Figure 1.8) Other scaffolds provide donor distance that are either too close or too far way for facial ligation.

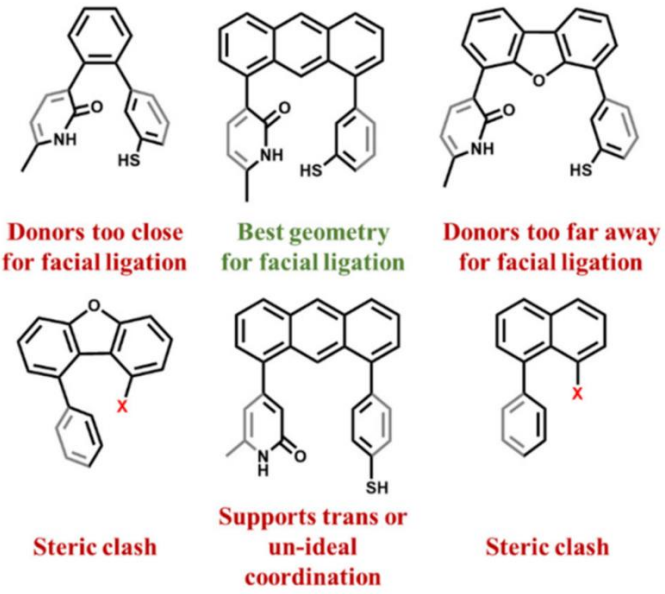


Figure 1.8: Possible scaffold approaches for incorporating the biomimetic donor sets of Hmd active site.[90]

As the iron-anthracene complexes show some degree of reactivity towards $H_2$ activation,[101,102] our focus progressed into the effect of fluxionality of the scaffold on the reactivity of the metal complex. Work by van Leeuwen showed a promising result in that the increased flexibility on the anthranoid scaffold does have positive influence on the catalytic activity of the rhodium complex.[97–99] In our case, we chose the thianthrene scaffold to be used as the more flexible version of anthracene scaffold. Details of thianthrene and the attempts to synthesize the thianthrene-scaffolded ligands are discussed in Chapter 5.

# Chapter 2: "Criss-Crossed" Dinucleating Behavior of an N4 Schiff Base Ligand in $\mu$-OH,$\mu$-$O_2$ Dicobalt(III) Species[a]

## 2.1 Introduction

### 2.1.1 Metal-Dioxygen Complexes

Activating dioxygen is a crucial process in biological systems and is directly related to life-sustaining metabolism. In nature, reversible $O_2$ binding is performed by metalloproteins such as hemoglobin, hemerythrin and hemocyanin, in which transition metal(s) like iron(s) and coppers are present in the active site (Figure 2.1). Biomolecules such as cytochrome P450 are known for their oxygen-activating ability with the aid of iron-containing heme. Indeed, these well-known enzymes achieve catalytic activity by utilizing active site metal ion(s). From the bioinorganic/biomimetic perspective, this inspires many researchers to study metal-dioxygen complexes for their industrial and medical applications.

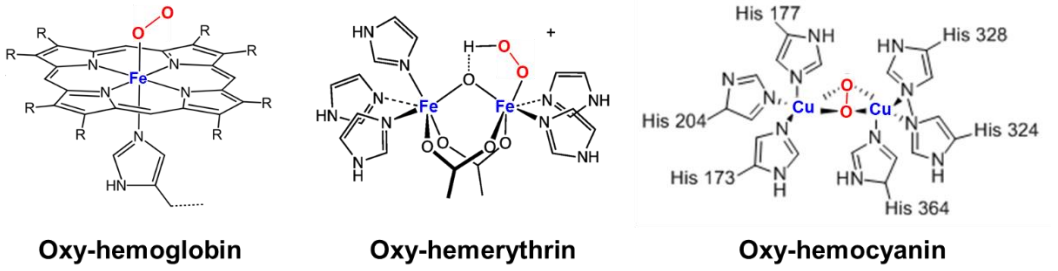


Figure 2.1: Structures of active site of the metalloproteins with $O_2$ binding ability.

However, nature does not utilize cobalt as the active site metal ion. During the oxygenation of the Fe(II) center in iron-porphyrin into Fe(III)-$O_2^{\bullet -}$, the unpaired electron of Fe(III) (low spin, $d^5$) can antiferromagnetically couple with a radical of the superoxide,

[a] Cho, Y. I.; Joseph, D. M.; Rose, M. J. "Criss-Crossed" Dinucleating Behavior of an N4 Schiff Base Ligand: Formation of a $\mu$-OH,$\mu$-$O_2$ Dicobalt(III) Core via $O_2$ Activation. *Inorg. Chem.* **2013**, *52* (23), 13298–13300. The author contributed as the first author in publishing this article.

exhibiting a spectroscopically diamagnetic system. In case of Co(III)-$O_2^{\bullet -}$, the cobalt becomes $S = 0$ having no unpaired electron for antiferromagnetic coupling to stabilize the radical of the superoxide. Nature chose to utilize iron, instead of cobalt, to avoid unstable radical compound formation. Additionally, a Co(III) (low spin, $d^6$) system exhibits a large $\Delta_{OCT}$, which makes the oxygen-adduct too kinetically stable for the release of $O_2$: this is a critical disadvantage for 'carrying' $O_2$ that requires both binding and releasing of $O_2$. In the case of iron, $\Delta_{OCT}$ is not as large, which makes a sufficiently stable oxygen-bound species and reactive-enough species for releasing $O_2$.

Despite the fact that there is no naturally occurring cobalt-based enzyme catalyzing $O_2$ activation yet, utilizing cobalt-dioxygen complexes as synthetic models for $O_2$-related catalysis has potential. In the periodic table, Co is close to Fe and Cu, the transition metals found in metalloenzymes (hemoglobin, hemerythrin and hemocyanin), thereby providing some similarities. In addition, synthetically produced cobalt-version of hemoglobin called 'Coboglobin' showed reversible $O_2$-binding, though its affinity was lower compared to the iron-version.[103]

### 2.1.2 Dicobalt-Dioxygen Complexes

After the very first dicobalt complex was discovered in 1852 by Edmond Frémy[104], research on dinuclear cobalt complexes has been heavily studied by a number of researchers.[105–114] Among them, pioneering work by Alfred von Werner in early 1900's served as a foundation for the field of peroxo-bridged dicobalt systems. Werner described the preparation of coordination complexes containing a dicobalt core with a stabilized dioxygen ligand, and the remaining coordination sphere was proposed to be occupied by an array of ammine ligands.[115,116] However, the exact structure and designation of the core dioxygen ligand was controversial for some time. Nearly 100 years after Werner's initial

report of the crystalline dioxygen-activated dicobalt species, Werner's historical sample was characterized by X-ray crystallography and reported as $\mu$-OH, $\mu$-$O_2$, $\mu$-$NH_2$-[{$Co(NH_3)_3$}$_2$]$(NO_3)_3$.[117] (Figure 2.2)

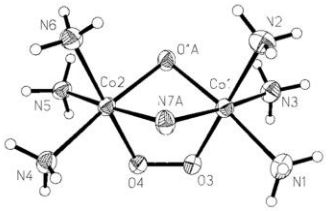


Figure 2.2: X-ray structure of the complex $\mu$-OH, $\mu$-$O_2$, $\mu$-$NH_2$-[{$Co(NH_3)_3$}$_2$]$(NO_3)_3$ by prepared by Werner in 1910[115] and characterized by Spingler *et al*. in 2001.[117].

Oxygen-adducts of cobalt complexes are the most studied metal-dioxygen complexes.[118] In general, $O_2$ is oxidatively added to Co(II) precursors upon the synthesis of Co(III)-$O_2$ complex (Scheme 2.1) via highly rapid and reversible process.[119,120] From each Co(II) center, an electron is transferred into dioxygen, forming an overall diamagnetic dimer of two Co(III) centers and a peroxide ($O_2^{2-}$) bridge. However, it has been reported that the reversibility is limited in most cases, as the main species are decomposed over many cycles into inactive species with higher oxidation state.[120] The origin of the bridging $O_2$ was confirmed by isotopic labeling studies using $^{18}O_2$, proving that it is not from oxygen from a water molecule, but rather from the molecular oxygen from atmosphere.[121] The O–O distance of binuclear cobalt $\mu$-peroxo system roughly ranges 1.42–1.49 Å (Table 2.1), though exceptions are present depending on the number of bridges present or type of ligands.

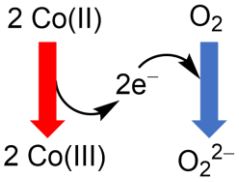

Scheme 2.1: Generic scheme of 2-electron transfer from Co(II) to dioxygen, yielding Co(III) and peroxide ion.

| Species | O–O distance (Å) | Bond order | Ref. |
|---|---|---|---|
| Dioxygen ($O_2$) | 1.20 | 2 | 122 |
| Superoxide ($O_2^{\bullet-}$) | 1.26 ± 0.02 | 1.5 | 122 |
| | 1.32–1.35 | | 123 |
| Peroxide ($O_2^{2-}$) | 1.49 ± 0.02 | 1 | 122 |

Table 2.1: Average distances for O–O in different dioxygen species.

The majority of synthetic dicobalt-dioxygen complexes have two Co(III) centers connected by a $\mu$-peroxo ($O_2^{2-}$) bridge. The $\mu$-peroxo bridge can be further oxidized using an oxidant, such as Ce(IV), to prepare the corresponding $\mu$-superoxo complexes.[119] These dicobalt-dioxygen complexes sometimes feature a second bridge such as a $\mu$-hydroxo ($OH^-$) or a $\mu$-amido ($NH_2^-$) group. Especially, the hydroxo bridge is proposed to "lock in" the peroxo bridge with the caged system, driving the equilibrium further towards the oxygenated complex.[124] This is consistent with spontaneous $O_2$-capturing process / oxidative addition of $O_2$ during the reaction of Co(II) precursors to yield dicobalt-dioxygen complexes. The superoxo versions are considered useful, based on some studies showing superoxo species (for example, a cobaloxime complex [Py-Co($D_2H_2$)-$O_2^{\bullet-}$-Co($D_2H_2$)-Py]$^+$, D = dianion of dimethylglyoxime) as key intermediate in the mechanism.[66] However, due to a highly reactive nature of superoxide ion, irreversible annihilation is not uncommon.[125]

Generally, these dicobalt-peroxo complexes are supported by mono-, bi- or tetra-dentate nitrogenous ligands ($NH_3$, bpy, en, $Me_2$teta), as well as mixed N,O donor sets (salen).[126] It has been reported that the presence of oxygenic groups decrease the readiness of the dicobalt complexes to form stable $O_2$ adducts.[127–129] On the other hand, nitrogen has somewhat stronger σ-donating ability than oxygen, allowing the cobalt center to transfer

an electron to $O_2$, thus forming the adduct.[130] In this sense, a Schiff-base ligand with four N donors and chelating effect greatly enhances the stability of the oxygenated product.

### 2.1.3 Applications of Dicobalt-Dioxygen Complexes

A number of binuclear cobalt complexes with $\mu$-$O_2$ (peroxo or superoxo) bridge have been studied for their applicability in biomedical research as $O_2$ carriers.[131,132] Particularly, photodissociable caged $O_2$ complexes are considered to be promising modes for in situ $O_2$ production. Such complexes release $O_2$ only when irradiated with light, revealing their utility. Their high water-solubility at physiological pH is also a desirable feature. Having intense absorbance in the UV region is another advantage of the $\mu$-$O_2$ dicobalt complexes, causing less interference in visible region in optical measurements in biological systems.

Researchers worked on dicobalt-peroxo systems as synthetic models featuring robust and earth-abundant transition metal (as seen in the active site of enzymes like cytochrome c oxidase) instead of Pt, in order to better understand the proton-coupled electron transfer (PCET) process via reduction of dioxygen into water. Dicobalt(III) dioxygen adducts have also been studied as small molecule models[133–136] relevant to heterogeneous oxygen evolving materials, such as cobalt oxide ($Co_2O_3$).[137,138]

## 2.2 RESULTS AND DISCUSSION

### 2.2.1 Synthesis Overview

Reaction of the Schiff base ligand N,N-bis(pyridin-2-ylmethylene)ethane-1,2-diimine (**enN$_4$**) with either [Co(H$_2$O)$_6$](BF$_4$)$_2$ or [Co(H$_2$O)$_6$](ClO$_4$)$_2$ in aerobic MeCN with excess pyridine (~10 equiv) results in the formation of a dark blackish-orange solution (Scheme 2.2).

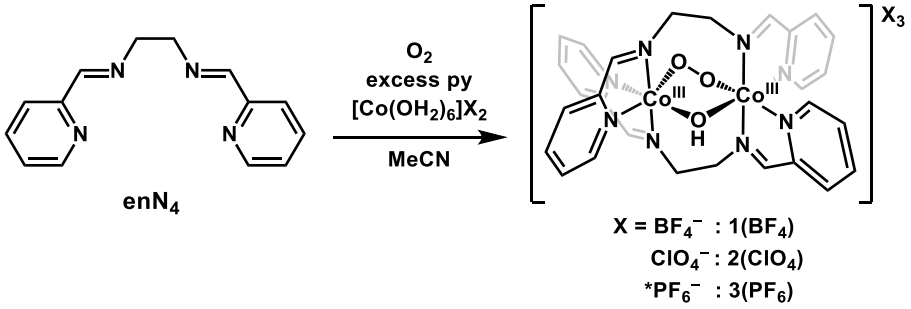


Scheme 2.2: Synthesis of dicobalt complexes **1(BF$_4$)$_3$**, **1(ClO$_4$)$_3$** and **1(PF$_6$)$_3$**. *: For **1(PF$_6$)$_3$**, [Co(MeCN)$_6$](PF$_6$)$_2$ was used instead of the hexahydrate salt.

The solution from the reaction of [Co(H$_2$O)$_6$](BF$_4$)$_2$ was set up for vapor diffusion with Et$_2$O, which yielded black blocks suitable for X-ray diffraction (31% yield) as $\mu$-OH, $\mu$-O$_2$[Co(e**nN$_4$**)]$_2$(BF$_4$)$_3$ (**1(BF$_4$)$_3$**). When [Co(H$_2$O)$_6$](ClO$_4$)$_2$ was used in place of the tetrafluoroborate salt, $\mu$-OH, $\mu$-O$_2$[Co(**enN$_4$**)]$_2$(ClO$_4$)$_3$, or **1(ClO$_4$)$_3$**, was isolated as a precipitate directly from the reaction (37% yield). Slow evaporation of a dilute MeCN/tol solution afforded X-ray quality crystals as $\mu$-OH, $\mu$-O$_2$[Co(**enN$_4$**)]$_2$(ClO$_4$)$_3$•2MeCN•H$_2$O, confirming a nearly identical core structure to that observed in **1(BF$_4$)$_3$**. From the reaction of [Co(MeCN)$_6$](PF$_6$)$_2$ instead of the hexahydrate salts, followed by vapor diffusion with Et$_2$O, X-ray quality crystals were isolated, again with an almost identical core, as $\mu$-OH, $\mu$-O$_2$[Co(**enN$_4$**)]$_2$(PF$_6$)$_3$ (**1(PF$_6$)$_3$**) (28% yield). Further details of the X-ray crystal structures are provided in section 2.2.2 (Figure 2.5-2.7).

These nearly identical structure of the cations highlights the generality of the reaction. Solutions of both **1(BF$_4$)$_3$** and **1(ClO$_4$)$_3$** in CD$_3$CN exhibit $^1$H NMR peaks in the diamagnetic region (Figure 2.3 and 2.4), including a $\mu$-hydroxy proton resonance observed at –0.91 ppm and –0.86 ppm, respectively. In conjunction with the hydroxy proton located in the density map, this supports the overall Co(III)Co(III) assignment. Solutions in CD$_3$CN are stable in the presence of air and moisture over the course of several months.

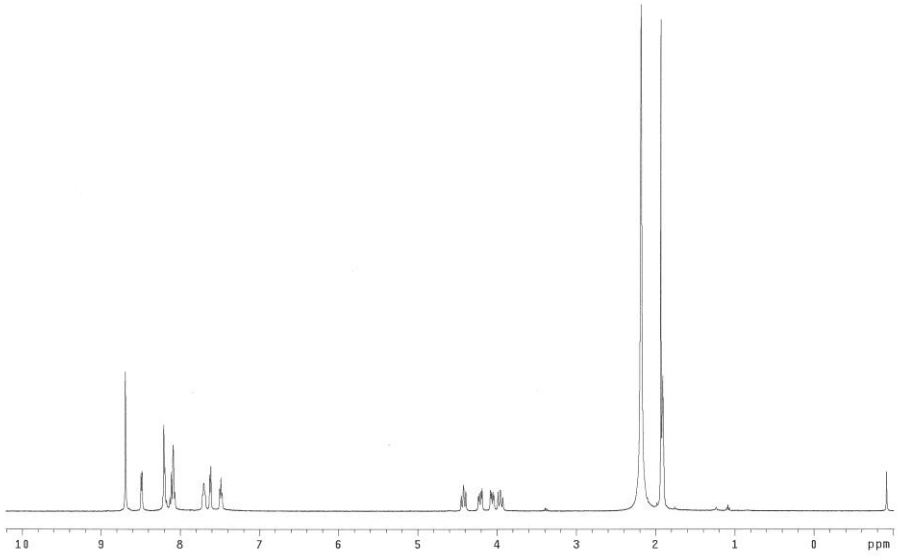


Figure 2.3: $^1$H NMR of **1(BF$_4$)$_3$** in CD$_3$CN (298 K) obtained at 400 MHz.

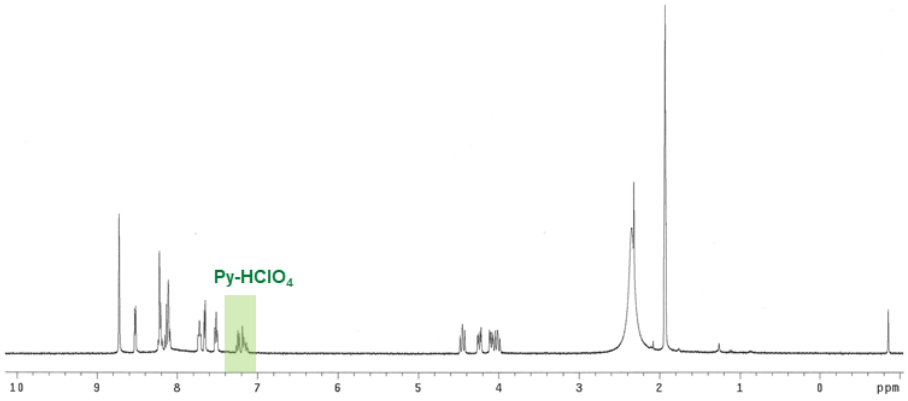


Figure 2.4: $^1$H NMR of **1(ClO$_4$)$_3$** (as isolated directly from the reaction mixture) in CD$_3$CN (298 K) obtained at 400 MHz.

Omission of excess pyridine in the reaction or any subsequent crystallization prevented isolation of the complex. We ascribe this observation to the need for pyridine in the stoichiometry of the reaction, according to Eq. 2.1:

$$2\ enN_4 + 2\ [Co(H_2O)_6](X)_2 + py + O_2 \rightarrow$$
$$\mu\text{-}OH,\ \mu\text{-}O_2[\{Co(enN4)\}_2]X_3 + py\text{-}HX + 11\ H_2O$$

### 2.2.2 X-ray Structure of Metal Complexes

All three structures exhibit a dicobalt system bridged by *i*) a $\mu$-OH and $\mu$-$O_2$ core; and *ii*) a stretched **enN**$_4$ ligand frame [for **1(BF**$_4$**)**$_3$, N2–C7–C8 = 114.2(3)°; N3–C8–C7 = 117.6(3)°] that spans both cobalt ions. The two **enN**$_4$ ligands co-chelate the cobalt centers in a diagonal fashion that criss-crosses the $\mu$-OH, $\mu$-$O_2$ dicobalt core. The peroxo bridge is slightly disordered across diagonal orientations (89/11% for **1(BF**$_4$**)**$_3$; 91/9% for **1(ClO**$_4$**)**$_3$; see Figure 2.5 and 2.6).

#### *2.2.2.1 (μ-OH)-(μ-η$^1$-$O_2$)-[(enN$_4$)$_2$Co$_2$](BF$_4$)$_3$ (1(BF$_4$)$_3$)*

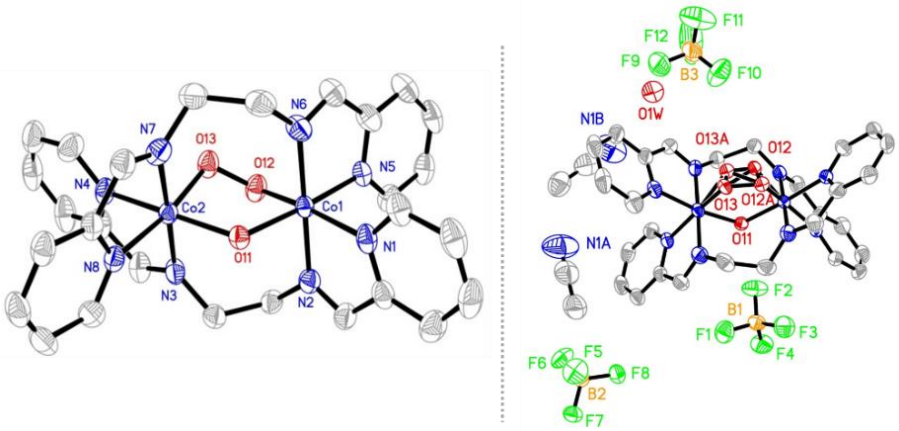


Figure 2.5: ORTEP diagram (50% ellipsoids) of (left) the cation of **1(BF**$_4$**)**$_3$ and (right) the full crystal structure illustrating the disordered peroxo unit (89/11%).

The X-ray structure of **1(BF$_4$)$_3$** (Figure 2.5) exhibits the O–O bond of 1.394 Å and Co–O$^{peroxo}$ bonds of 1.848(2) and 1.866(2) Å (See Table 2.2 for a complete comparison of bond metrics.). The observed Co–O$^{hydroxo}$ bonds are 1.892(19) and 1.900(18) Å. The **enN$_4$** ligands are stretched and criss-crossed, generating the torsion angles of 81.2(4)° for N2-C7-C8-N3 and 80.1(5)° for N6-C21-C22-N7. As a result, two cobalt centers are separated 3.182 Å from each other.

### *2.2.2.2 (μ-OH)-(μ-η$^1$-O$_2$)-[(enN$_4$)$_2$Co$_2$](ClO$_4$)$_3$ (1(ClO$_4$)$_3$)*

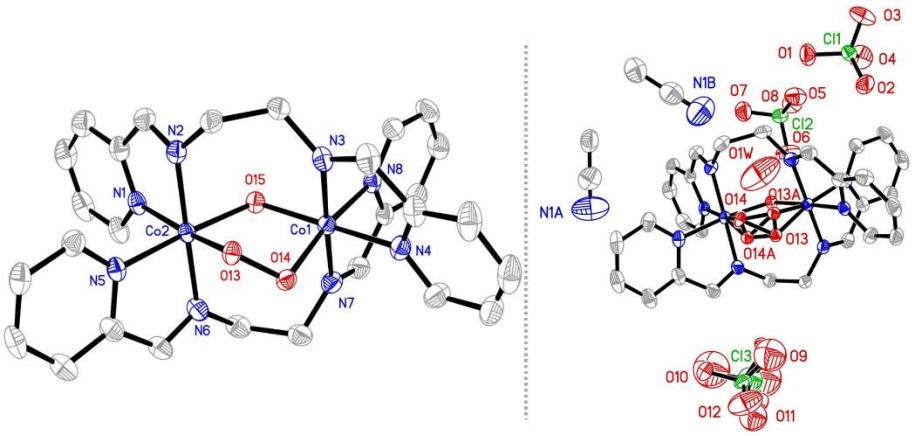


Figure 2.6: ORTEP diagram (50% ellipsoids) of (left) the cation of **1(ClO$_4$)$_3$** and (right) the full crystal structure illustrating the disordered peroxo unit (91/9%) and perchlorate disorder (80/20%).

The X-ray structure of **1(ClO$_4$)$_3$** (Figure 2.6) exhibits the O–O bond of 1.401(3) Å and Co–O$^{peroxo}$ bonds of 1.839(3) and 1.858(3) Å (See Table 2.2 for a complete comparison of bond metrics.). The observed Co–O$^{hydroxo}$ bonds are 1.886(2) and 1.894(2) Å. The **enN$_4$** ligands are stretched and criss-crossed, generating the torsion angles of –81.1(3)° for N2-C7-C8-N3 and –80.5(3)° for N6-C21-C22-N7. As a result, two cobalt centers are separated 3.178 Å from each other.

### *2.2.2.3 (μ-OH)-(μ-η$^1$-O$_2$)-[(enN$_4$)$_2$Co$_2$](PF$_6$)$_3$ (1(PF$_6$)$_3$)*

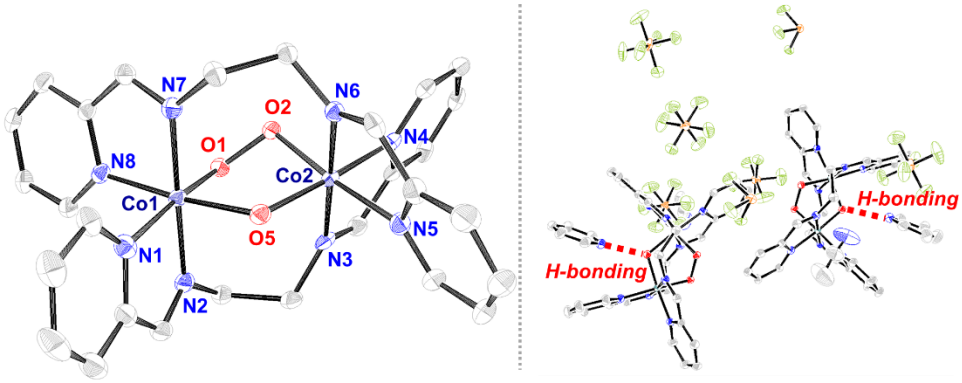


Figure 2.7: ORTEP diagram (50% ellipsoids) of (left) the cation of **1(PF$_6$)$_3$** and (right) the full crystal structure, showing hydrogen bonding between pyridine N and $\mu$-hydroxo H.

The X-ray structure of **1(PF$_6$)$_3$** (Figure 2.7) exhibits the O–O bond of 1.410(4) Å and Co–O$^{peroxo}$ bonds of 1.847(2) and 1.852(3) Å (See Table 2.2 for a complete comparison of bond metrics.). The observed Co–O$^{hydroxo}$ bonds are 1.884(3) and 1.894(3) Å. Two cobalt centers are separated 3.172 Å from each other. Notice the presence of one pyridine per cation. The N$^{py}$ atom is directly pointing at the $\mu$-hydroxo bridge via hydrogen bonding of the H$^{\mu\text{-hydroxo}}$ atom, which provides an evidence that the bridge is indeed OH$^-$ and not O$^{2-}$.

### 2.2.3 Structural Comparison with Known Dicobalt Complexes

There are a number of similar $\mu$-OH, $\mu$-O$_2$ dicobalt cores supported by N-containing ligands that have been structurally characterized (see Table 2.2). For example, the complexes $\mu$-OH,$\mu$-O$_2$-[{Co(en)$_2$}$_2$] (en = ethylenediamine) and $\mu$-OH, $\mu$-O$_2$-[{Co(bpy)$_2$}$_2$] (bpy = 2,2'-bipyridine) exhibit the analogous core structure without the support of the N4 type dinucleating ligand.[131,132,139–142] In the tren [tren = tris(2-aminoethyl)amine)] and Me$_2$teta [Me$_2$teta = N,N-(dimethyl)triethylenetetramine] derivatives $\mu$-OH,$\mu$-O$_2$[(L)$_2$Co]$_2$(ClO$_4$)$_3$, the ligands simply cap each cobalt center, with no interconnection of the ligand across the two cobalt centers.

The two Co–O(O) bond lengths of 1.839(3) (Co1–O12) and 1.858(3) Å (Co2–O13) are quite short when compared to other tetraimine ligated $\mu$-OH,$\mu$-$O_2$ complexes [range = 1.860(2) to 1.877(4) Å] of type $\mu$-OH,$\mu$-$O_2$[$(bpy)_2Co]_2^{3+}$; similar complexes derived from alkyl amines (en, tren, $Me_2$teta) are also longer [range = 1.857 to 1.947 Å].[139–142] The observed peroxo bond [O–O = 1.401(3) Å] (O12–O13) is shorter than that found in the bpy derivatives [1.415(6), 1.412(3) Å] and most of the alkylamine derivatives [range = 1.430 to 1.462 Å]. Two exceptions of note are the en dimer $\mu$-OH,$\mu$-$O_2$-$[(en)_2Co]_2(NO_3)_3$ [O–O = 1.339 Å] and the Werner complex $\mu$-OH, $\mu$-$O_2$, $\mu$-$NH_2$-$[(NH_3)_3Co]_2(NO_3)_3$ [O–O = 1.340(4) Å], which exhibits an anionic amido bridge in addition to the $\mu$-OH, $\mu$-$O_2$ core.[117,139–142] The O–O bond in **1(BF$_4$)$_3$** (1.401(3) Å) is on the low end of the peroxo range (typically 1.4-1.5 Å) compared to the superoxo range (1.25-1.35 Å). Another interesting structural metric is the Co•••Co distance. Considering all of the dicobalt complexes exhibiting the $\mu$-OH, $\mu$-$O_2$ core listed in Table 2.2, **1(BF$_4$)$_3$** exhibits the shortest distance between cobalt centers (3.18 Å). Only the Werner complex $\mu$-OH, $\mu$-$O_2$, $\mu$-$NH_2$-$[(NH_3)_3Co]_2(NO_3)_3$ exhibits a shorter distance between cobalt ions [Co•••Co = 2.766(4) Å].[131,132] This is likely due to the additional amido bridge and the higher overall oxidation state of the species (formally Co(III)-Co(IV)). The close proximity of the cobalt centers in the present case is thus likely the result of the 'criss-crossed', dinucleating **enN$_4$** ligands.

| Complex | Denticity | Di-nucleating? | Co–O(O) | (O)O–Co | (Co)O–O(Co) | Co–O(H) | (H)O–Co | Co•••Co | UV/vis λ in nm (ε in $cm^{-1}$ $M^{-1}$) | Ref. |
|---|---|---|---|---|---|---|---|---|---|---|
| **1(BF$_4$)$_3$** | 2 x N4 | Yes | 1.848(2) | 1.866(2) | 1.394(3) | 1.892(19) | 1.900(18) | 3.182 | 478 (10 060)<br>390 (11 320) | this work |
| **1(ClO$_4$)$_3$** | 2 x N4 | Yes | 1.839(3) | 1.858(3) | 1.401(3) | 1.886(2) | 1.894(2) | 3.178 | 474 (11 340)<br>398 (8 060) | this work |
| **1(PF$_6$)$_3$** | 2 x N4 | Yes | 1.847(2) | 1.852(3) | 1.410(4) | 1.884(3) | 1.894(3) | 3.172 | -- | this work |
| **$1^{3+}$ (DFT) 6-31G*/PW91** | 2 x N4 | Yes | 1.8464 | 1.8429 | 1.3737 | 1.9284 | 1.9347 | 3.2265 | -- | this work |
| **$1^{3+}$ (DFT) TZV/B3PW91** | 2 x N4 | Yes | 1.8378 | 1.8367 | 1.4264 | 1.9170 | 1.9251 | 3.2498 | -- | this work |
| **$\mu$-OH, $\mu$-O$_2$ [(Me$_2$teta)$_2$Co]$_2$(ClO$_4$)$_3$**[b] | 2 x N4 | No | 1.946(14) | 1.843(15) | 1.429(20) | 1.934(19) | 1.987(19) | 3.321 | 296 (~6 000)<br>389 (~6 000) | 142 |
| **$\mu$-OH, $\mu$-O$_2$ [(tren)$_2$Co]$_2$(ClO$_4$)$_3$**[c] | 2 x N4 *tripodal* | No | 1.857(18) | 1.869(20) | 1.462(26) | 1.970(23) | 1.872(23) | 3.292 | -- | 139 |
| **$\mu$-OH, $\mu$-O$_2$ [(bpy)$_2$Co]$_2$(ClO$_4$)$_3$** | 4 x N2 | n/a | 1.868(5) | 1.877(4) | 1.415(6) | 1.917 | 1.911 | 3.304 | -- | 132 |
| **$\mu$-OH, $\mu$-O$_2$ [(bpy)$_2$Co]$_2$(NO$_3$)$_3$** | 4 x N2 | n/a | 1.860(2) | 1.8717(19) | 1.412(3) | 1.892(2) | 1.894(2) | 3.270 | -- | 131 |
| **$\mu$-OH, $\mu$-O$_2$ [(en)$_2$Co]$_2$(ClO$_4$)$_3$** | 4 x N2 | n/a | 1.866(10) | 1.880(8) | 1.460(13) | 1.919(8) | 1.934(10) | 3.289 | 279 (~5 500)<br>358 (~5 500) | 141 |
| **$\mu$-OH, $\mu$-O$_2$ [(en)$_2$Co]$_2$(NO$_3$)$_3$** | 4 x N2 | n/a | 1.875 | 1.873 | 1.339 | 1.916 | 1.900 | 3.261 | -- | 140 |
| **$\mu$-OH, $\mu$-O$_2$, $\mu$-NH$_2$ [(NH$_3$)$_3$Co]$_2$(NO$_3$)$_3$** | 6 x N1 | n/a | 1.872(3) | 1.887(3) | 1.340(4) | 1.922(4)[a] | -- | 2.766 | -- | 117 |
| **$1^{4+}$ (DFT) 6-31G*/PW91** | 2 x N4 | Yes | 1.8379 | 1.8369 | 1.3383 | 1.9219 | 1.9221 | 3.2377 | -- | -- |
| **$1^{4+}$ (DFT) TZV/B3PW91** | 2 x N4 | Yes | 1.8819 | 1.8794 | 1.3524 | 1.9167 | 1.9197 | 3.2791 | -- | -- |

Table 2.2: Selected bond distances (Å) in complexes containing a $\mu$-OH, $\mu$-O$_2$ core and DFT calculated bond distances for **$1^{3+}$** and **$1^{4+}$**. (*a)* note: the $\mu$-OH and $\mu$-NH$_2$ in this structure were crystallographically indistinguishable. (*b*) TETA = triethylenetetramine (*c)* tren = tris(2-aminoethyl)amine.

### 2.2.4 Infrared Spectroscopy via Isotopic Labeling Studies

The IR spectrum of **1(ClO$_4$)$_3$** exhibits a ligand-based ν(CN) feature at 1633 cm$^{-1}$ (1635 cm$^{-1}$ in **1(BF$_4$)$_3$**), which is red-shifted from the unbound ligand value of 1647 cm$^{-1}$. The lower energy region of **1(ClO$_4$)$_3$** exhibits notable stretches at 882, 776 and 650 cm$^{-1}$ (887, 775 and 649 cm$^{-1}$ for **1(BF$_4$)$_3$**) (See Appendix B.1 for the full infrared spectra). The assignment of the ν(O–O) IR feature was verified using isotopic labeling. We chose **1(ClO$_4$)$_3$** instead of **1(BF$_4$)$_3$** for isotopic labeling study, due to its convenient and direct precipitation from the reaction without the need of further crystallization, unlike **1(BF$_4$)$_3$**. Metalation of **enN$_4$** with [Co(H$_2$O)$_6$](ClO$_4$)$_2$ in MeCN in presence of pyridine under $^{18}$O$_2$ atmosphere results in one red-shifted feature at 833 cm$^{-1}$ (the $^{16}$O–$^{16}$O stretch at 882 cm$^{-1}$ is absent; see Figure 2.8, red trace). This confirms the ν(O–O) assignment at 882 cm$^{-1}$ in the IR spectrum of **1(ClO$_4$)$_3$**. Consequently, metalation under $^{17}$O$_2$ atmosphere results in $^{17}$O–$^{17}$O stretch at 860 cm$^{-1}$ (Figure 2.8, green trace)

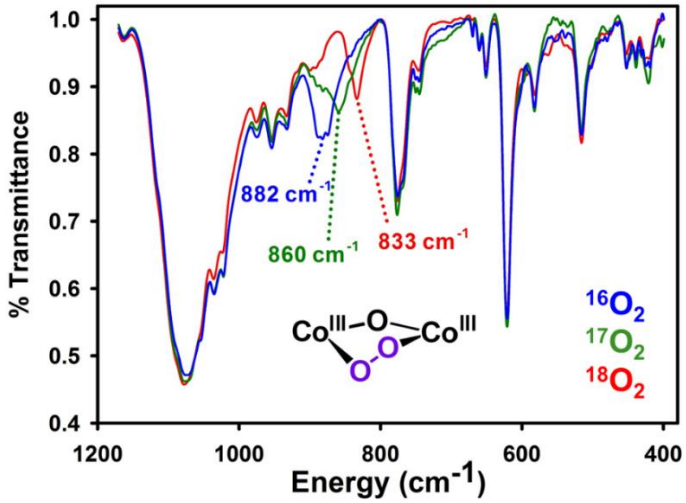


Figure 2.8: Infrared spectra of isotopically distinct **1(ClO$_4$)$_3$** as derived from $^{16}$O$_2$ (blue trace, ν(O–O) = 882 cm$^{-1}$), $^{17}$O$_2$ (green trace, ν(O–O) = 860 cm$^{-1}$; $\Delta\nu_{expt}$ = 22 cm$^{-1}$, $\Delta\nu_{theory}$ = 26 cm$^{-1}$) and $^{18}$O$_2$ (red trace, ν(O–O) = 833 cm$^{-1}$; $\Delta\nu_{expt}$ = 49 cm$^{-1}$, $\Delta\nu_{theory}$ = 48 cm$^{-1}$).

### 2.2.5 Oxidation Reactions

#### *2.2.5.1 Electrochemical Oxidation*

We suspected that the interlinked nature of the cobalt peroxo core might stabilize reduced or oxidized species to an unusual extent. The cyclic voltammogram of **1(BF$_4$)$_3$** in MeCN (0.1 M TBAP, 100 mV/s) is shown in Figure 2.9. The complex exhibits a reversible feature at $E_{½}$ = +0.50 V vs Fc/Fc$^+$, as well as an irreversible feature at –1.07 V vs Fc/Fc$^+$. All three peak currents in the CV follow a scan rate dependence that is linear with $\sqrt{\nu}$ (inset of Figure 2.9; all data shown in Figure 2.10). We hypothesized that the reversible feature was the result of clean Co(III)Co(III) ↔ Co(III)Co(IV) transformations.

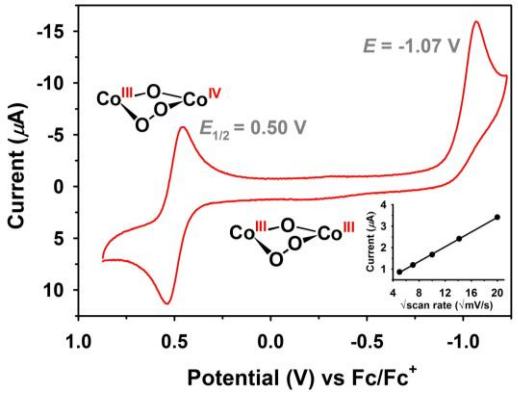


Figure 2.9: Cyclic voltammogram of **1(BF$_4$)$_3$** in MeCN containing 0.1 M NBu$_4$ClO$_4$ (100 mV/s). *Inset:* Scan rate dependence of the reversible oxidation wave at +0.54 V (see Figure 2.10 for scan rate dependence of other peaks).

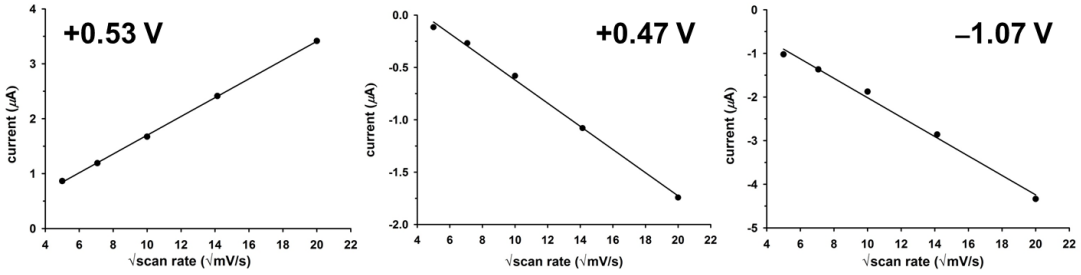


Figure 2.10: Scan rate dependence (25-400 mV/s) of the three features in the CV of **1(BF$_4$)$_3$**: reversible oxidation wave at +0.53 V (left); reversible reduction wave at +0.47 V (middle); irreversible reduction wave at –1.07 V (right).

### *2.2.5.2 Chemical Oxidation and EPR Spectroscopy*

In the absence of structural characterization of the oxidized species, EPR spectroscopy was performed. Treatment of **1(ClO$_4$)$_3$** in MeCN with (NH$_4$)$_2$[Ce(NO$_3$)$_6$] at –40 °C resulted in an immediate color change from brownish red to gray-green; this solution was not stable at higher temperatures. EPR analysis of an aliquot from the –40 °C reaction (frozen MeCN, or MeCN/CH$_2$Cl$_2$ glass, 90 K) afforded a somewhat broad, asymmetric EPR spectrum with *g*-values = 2.06, 2.02 (see Figure 2.11). No prominent hyperfine features were observed at lower temperatures (4-30 K) or upon introduction of $^{17}$O$_2$. The lack of notable axial features in the spectrum (as often observed in Co(IV) porphyrins, cobaloximes, salens)[9] is likely due to the alternate arrangement of the *z* axis at the cobalt center.

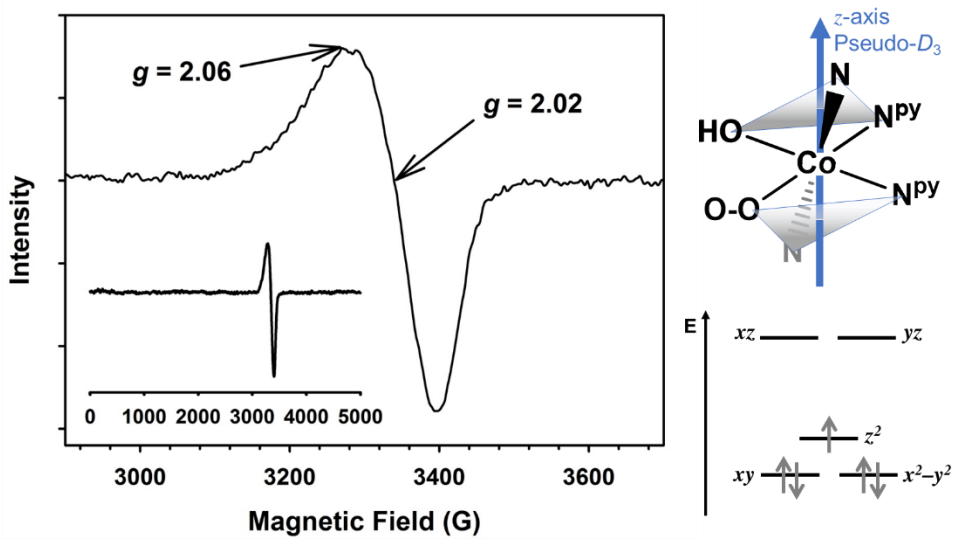


Figure 2.11: (Left) X-band EPR spectra of an MeCN solution of **1(ClO$_4$)$_3$** treated with 1 equivalent of (NH$_4$)$_2$[Ce(NO$_3$)$_6$] at –40 °C. Instrument settings: temperature, 90 K; frequency, 9.44 GHz; modulation, 100 kHz; power, 20 mW; field modulation, 5 G. Nearly identical spectra were recorded from 4-30 K. (Right) Local arrangement of the z axis in a Co(IV) center and the d-orbital diagram.

As the oxidized species proved unisolable in our hand, we investigated its structural and electronic properties by DFT (performed by another researcher, David M. Joseph). Calculations on the species $\mathbf{1}^{3+}$ at the 6-31G*/PW91 (and TZP/B3PW91) level afforded good agreement (within ~0.02 Å) between calculated and experimental bond distances (Table S2 of Ref 70). Overall, DFT supports our assignment of a Co(III)Co(III) dimer bridged by a dianionic peroxide ligand. DFT calculations on the one-electron oxidized species $\mathbf{1}^{4+}$ ($S = ½$) show that the spin density (Figure 2.12, left) is delocalized across *both* cobalt centers *and* the peroxo/superoxo ligand. By most quantitative measures (Table S3 of Ref 70), the balance of spin density tilts in favor of the peroxo (or superoxo) ligand. Some shortening (~0.07 Å) of the O–O bond is observed in the oxidized species (DFT, 1.338, 1.352 Å) versus the resting state (DFT = 1.374, 1.426 Å; Experimental = 1.401(3), 1.394(3) Å). But the oxidized O–O distance in $\mathbf{1}^{4+}$ is longer than the canonical superoxo bond length of ~1.25 Å.

Close inspection of the DFT calculated $d_{z^2}$ orbital indicates that it is not oriented along an axis of bonding (see Figure 2.12). Rather, the $d_{z^2}$ axis trisects one face of the octahedron, eliminating its assignment as an $O_h$ or $D_{4h}$ type system. Some seemingly related $D_3$ systems like $[Fe(III)(bpy)_3]^{3+}$ or $[Ir(IV)(gdt)_3]^{+}$ also exhibit a primary feature at $g_\perp \approx$ 2.6 (with a smaller feature, $g_\parallel = 0.3\text{-}1.6$).[10] The asymmetric $N_4O_2$ coordination environment in $\mathbf{1}^{4+}$ appears to give rise to a minor axial component that results in an electronic environment that resembles an axially elongated $D_3$ system (this usually promotes high or intermediate spin systems in the Fe(III) $d^5$ case). Note that the observed $g$-values of $\mathbf{1}^{4+}$ are similar to reports of cobalt-coordinated superoxo species ($g \approx$ 2.00 to 2.08).[11] Overall, we interpret the EPR signal as emanating from an $S = ½$ Co(IV) ion in a slightly axial coordination environment; this is partially consistent with the DFT calculation(s).

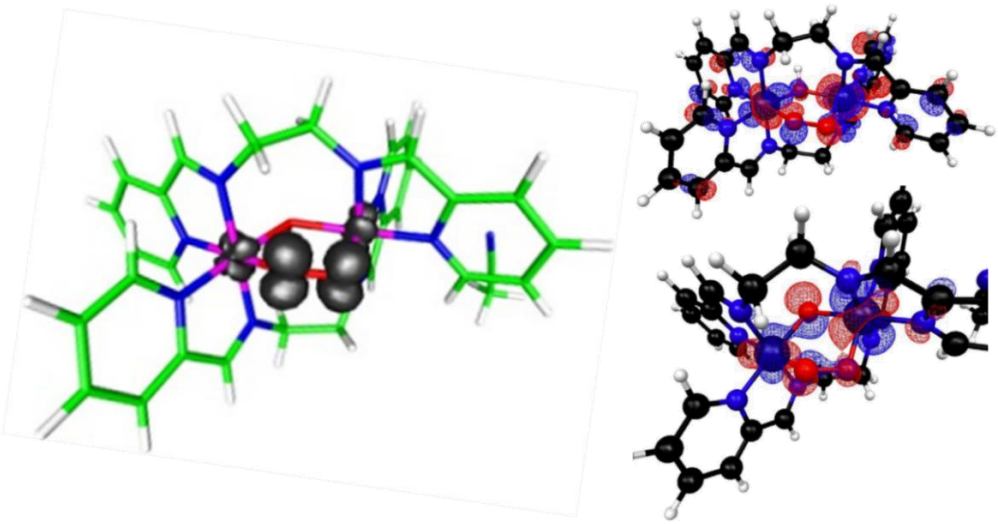

Figure 2.12: (Left) DFT calculated structure and spin density plot of the one-electron oxidized species $\mathbf{1}^{4+}$ (6-31G*/PW91). (Right, top) DFT calculated (6-31G*/PW91) $d_{z2}$ orbital in the optimized geometry of $\mathbf{1}^{3+}$ ($S = 0$). (Right, bottom) The $d_{z2}$ orbital for the one-electron oxidized $\mathbf{1}^{4+}$ calculated at the same level ($S = ½$).

### *2.2.5.3 X-ray Absorption Spectroscopy*

K-edge X-ray absorption spectroscopy (XAS) was performed on of $\mathbf{1(ClO_4)_3}$ and one-electron oxidized species by Jackson group at the University of Kansas. The Co(III)Co(III) and Co(III)Co(IV) samples have nearly identical edge and pre-edge energies (Figure 2.13 and Table 2.3). This suggest that the one-electron oxidation does not occur solely at the Co(III) center (*i.e.*, the hole is significantly delocalized, or localized at a site other than Co). The extended X-ray absorption fine structure (EXAFS) curves for the Co(III)Co(III) and Co(III)Co(IV) samples are nearly identical (Figure 2.14). The Fourier-transforms of the EXAFS spectra are also very similar (Figure 2.15), although there are some subtle differences in the EXAFS data that suggests there are minor structural differences between the Co(III)Co(III) and Co(III)Co(IV) complexes.

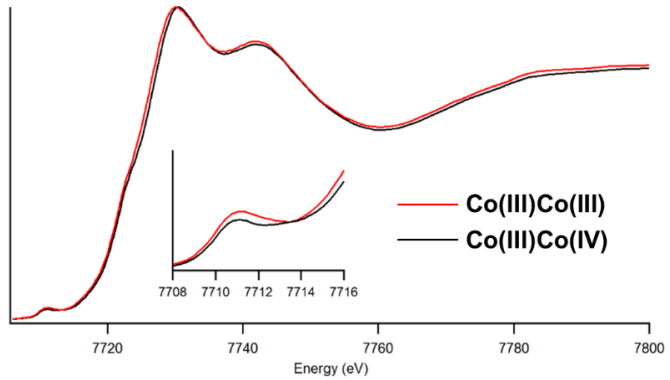


Figure 2.13: X-ray absorption near-edge regions of Co(III)Co(III) and Co(III)Co(IV) samples.

| Complex | Pre-edge energy (eV) | Edge energy |
|---|---|---|
| Co(III)Co(III) | 7711.1 | 7721.3 |
| Co(III)Co(IV) | 7711.1 | 7721.8 |

Table 2.3: Pre-edge and edge energies (eV) for Co(III)Co(III) and Co(III)Co(IV) samples.

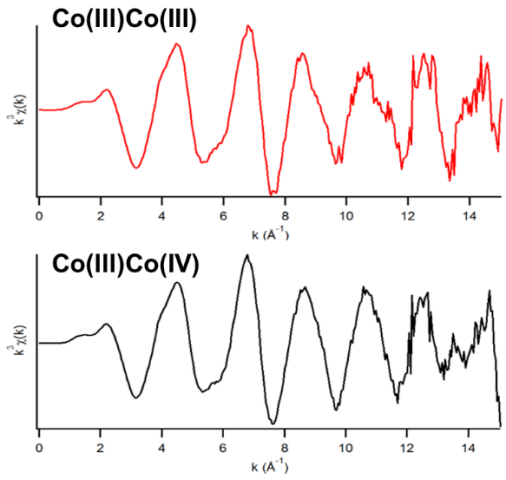


Figure 2.14: Raw EXAFS data for Co(III)Co(III) and Co(III)Co(IV) samples.

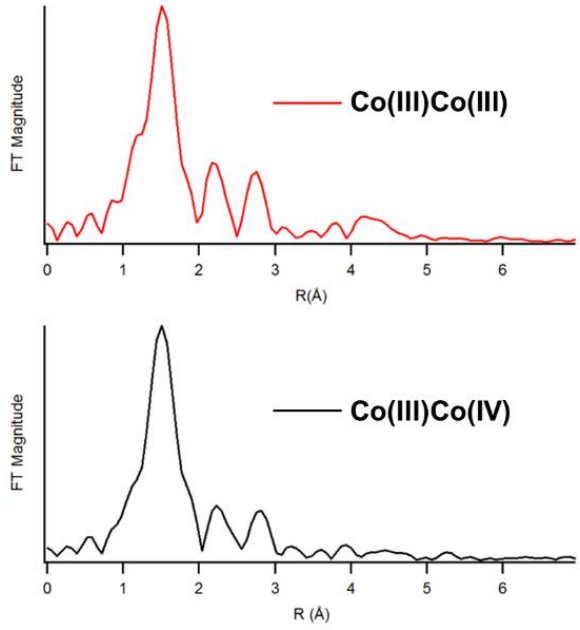


Figure 2.15: Fourier-transform EXAFS data ($k$ = 2 - 14 Å).

## 2.3 CONCLUSIONS

A series of complexes with a dinucleated $\mu$-$O_2$, $\mu$-OH dicobalt core using an N4 Schiff base ligand were synthesized, exhibiting more contracted core compared to previous reports of similar dicobalt-peroxo complexes. The "criss-crossed" ligand arrangement facilitates reversible Co(III)Co(III) ↔ Co(III)Co(IV) processes and the detection of the one electron oxidized Co(III)Co(IV) species was achieved by cyclic voltammetry, EPR spectroscopy and partially DFT calculation; however, XAS and EXAFS data on chemically oxidized species supports the oxidation on sites other than solely on cobalt ion.

## 2.4 EXPERIMENTAL

### 2.4.1 Reagents and Procedures

Cobalt(II) perchlorate hexahydrate, cobalt(II) tetrafluoroborate hexahydrate, ethylenediamine, 2-pyridinecarboxyaldehyde and 99% $^{18}O_2$ were obtained from Sigma-Aldrich. The ligand **enN**$_4$ was synthesized according to the published procedure of Banerjee and coworkers.[143] MeCN, pyridine, toluene and $Et_2O$ were purchased from Fisher Scientific and used without further purification. The deuterated solvent $CD_3CN$ was purchased from Cambridge Isotopes and used as received. Electrochemical grade tetrabutylammonium perchlorate (TBAP) was purchased from Fluka.

### 2.4.2 Synthesis of Compounds

#### *2.4.2.1 N,N-bis(pyridin-2-ylmethylene)ethane-1,2-diimine (enN$_4$)*[143]

The 2-pyridinecarboxaldehyde (4.29 g, 40.0 mmol) was added dropwise to 25 mL of MeOH. Separately, 1.20 g (20.0 mmol) of ethylenediamine was diluted in 10 mL of MeOH and added dropwise to the aldehyde solution. The solution was refluxed for 7 h, after which the solution turned yellow-orange. Upon cooling, the solution was dried with N2 in warm water bath. The final product was pale-yellow solid. Yield: 3.71 g (77.8%). Selected IR bands (ν in $cm^{-1}$): 1645 s 1584 m, 1564 m, 1470 m, 1434 m, 1425 m, 1356 m, 1333 m, 1295 m, 1217 w, 1150 w, 1105 w, 1043 m, 991 m, 979 m, 967 m, 920 m, 903 m, 869 m, 769 vs, 741 s, 649 w, 617 s, 572 w, 514 m, 482 s, 408 s. $^1$H NMR in $CDCl_3$ (δ in ppm): 8.56 d (2H, imine-H), 8.37 s (2H), 7.93 d (2H), 7.66 t (2H), 7.24 dd (2H), 4.01 s (4H).

#### *2.4.2.2 (μ-OH)-(μ-η$^1$-O$_2$)-[(enN$_4$)$_2$Co$_2$](BF$_4$)$_3$ (1(BF$_4$)$_3$)*

The ligand **enN**$_4$ (100 mg, 0.420 mmol) was dissolved in 7 mL of MeCN to make a pale-yellow solution, and 5 drops of pyridine were added. Separately, 143 mg (0.420 mmol) of $[Co(H_2O)_6](BF_4)_2$ was dissolved in 3 mL of MeCN to generate a pale red solution, and then

it was added dropwise to the stirred solution of the ligand. The solution became a red/burgundy within minutes, and over the course of 1 h became dark brown-orange; the reaction was stirred overnight (no color change). Black microcrystalline material was obtained from vapor diffusion of $Et_2O$ into the MeCN solution of the complex over the course of several days (75 mg, 31% yield). X-ray quality crystals were grown via slow vapor diffusion of $Et_2O$ into a dilute MeCN solution of the complex supplemented with several additional drops of pyridine (omission of pyridine at any stage prevented isolation of the complex). Analysis for $C_{32}H_{37}B_3Co_2F_{12}N_{10}O_4$: calcd, C 38.28, H 3.71, N 13.95; found, C 37.76, H 3.70, N 12.94.Selected IR bands, in $cm^{-1}$: 1635 w ($\nu_{C=N}$), 1601 m, 1305 m, 1229 w, 1018 br vs ($\nu_{BF}$), 887 m **($\nu_{\mu(O\text{-}O)}$)**, 775 s, 583 w, 516 s. $^1H$ NMR in $CD_3CN$ ($\delta$ in ppm): 8.69 s (4H), 8.49 d (2H, *J* = 5.2), 8.20 s, 8.19 t (2H), 8.09 m (4H), 7.70 m (2H), 7.62 d (2H), 7.49 t (2H), 4.42 t (2H, *J* = 11), 4.21 dd (2H, *J* = 13.2, 5.4), 4.06 dd (2H, *J* = 12.4, 5.6), 3.96 t (2H, *J* =11.8); –0.91 s (1H); the $^1H$ spectrum remains unchanged in $CD_3CN$ for months. UV/vis in MeCN, $\lambda$ in nm ($\varepsilon$ in $cm^{-1}$ $M^{-1}$): 474 (11 340), 398 (8 060).

#### *2.4.2.3 (μ-OH)-(μ-η$^1$-$O_2$)-[($enN_4$)$_2Co_2$]($ClO_4$)$_3$ (1($ClO_4$)$_3$)*

The ligand **enN**$_4$ (200 mg, 0.840 mmol) was dissolved in 15 mL of MeCN to make a pale-yellow solution, and 5 drops of pyridine were added. Separately, 308 mg (0.840 mmol) of $[Co(H_2O)_6](ClO_4)_2$ was dissolved in 5 mL of MeCN to generate a pale red solution, which was added dropwise to the stirred solution of the ligand. The solution became a red-brown within minutes, and over the course of 1 h became dark brown. After stirring 16 h, a black microcrystalline solid was collected by filtration, and washed with $Et_2O$. Yield: 163 mg (37%). X-ray quality crystals (black parallelipipes) were obtained from slow evaporation (at 35 °C) of a saturated solution of the complex in MeCN/toluene (3:1) containing 10 extra drops of pyridine. (Note: omission of pyridine in any step prevented isolation of the

complex.) Analysis for $C_{37}H_{43}Cl_4Co_2N_{11}O_{20}$: calcd, C 36.38, H 3.55, N 12.61; found, C 34.27, H 3.49, N 12.61. Selected IR bands, in $cm^{-1}$: 1633 w ($\nu_{C=N}$), 1600 m, 1304 m, 1229 w, 1073 vs br ($\nu_{ClO}$), 882 m br **($\nu_{\mu(o\text{-}o)}$)**, 776 s, 621 vs, 583 m, 516 m. $^1$H NMR in $CD_3CN$ ($\delta$ in ppm, J in Hz): 8.73 s (4H), 8.52 d (2H, *J* = 5.2), 8.24-8.09 m (8H), 7.72 t br (2H, *J* = 4.8), 7.65 d (2H, *J* = 6.0), 7.51 t (2H, *J* = 6.4), 4.45 t (2H, *J* = 11.2), 4.24 dd (2H, *J* = 13.2, 5.6), 4.09 dd (2H, *J* = 12.4, 5.6), 4.02 t (2H, *J* = 11.6), –0.86 s (1H); roughly 0.5 pyH-$ClO_4$ was observed in the material collected directly from the reaction: 7.26-7.14 m. Note: the $^1$H spectrum remains unchanged in $CD_3CN$ for months after storage at room temperature. UV/vis in MeCN, $\lambda$ in nm ($\varepsilon$ in $cm^{-1}$ $M^{-1}$): 478 (10 060), 390 (11 320).

#### *2.4.2.4 (μ-OH)-(μ-η$^1$-$O_2$)-[($enN_4$)$_2Co_2$]($PF_6$)$_3$ (1($PF_6$)$_3$)*

The ligand **enN**$_4$ (100 mg, 0.420 mmol) was dissolved in 50 mL of MeCN to make a pale-yellow solution, and 5 drops of pyridine were added. Separately, 250 mg (0.420 mmol) of $[Co(MeCN)_6](PF_6)_2$ (prepared by reacting $CoCl_2$ with $TlPF_6$) was dissolved in 5 mL of MeCN to generate a pale pink solution, which was added dropwise to the stirred solution of the ligand. The solution became a red within minutes, and over the course of 0.5 h became black; the reaction was stirred overnight (no color change). Yield: 127 mg (28%). X-ray quality crystals were grown as brownish black needles via slow vapor diffusion of $Et_2O$ into a reaction mixture supplemented with several additional drops of pyridine (omission of pyridine at any stage prevented isolation of the complex). Selected IR bands, in $cm^{-1}$: 1627 w ($\nu_{C=N}$), 1601 m, 1306 m, 1229 w, 884 m **($\nu_{\mu(o\text{-}o)}$)**, 821 vs br ($\nu_{P\text{-}F}$), 778 s, 555 s, 518 m.

### 2.4.3 X-ray Crystallography

Definitions used for calculating $R_w(F^2)$, R(F) and the goodness of fit, S, are given below. Tables of crystal data and refinement parameters and tables for bond lengths, angles and torsion angles are summarized in Appendix C.1.

$$R_w(F^2) = \sqrt{\frac{\sum w(|F_0|^2 - |F_C|^2)^2}{\sum w(|F_0|)^4}}$$

$$R(F) = \frac{\sum |F_0| - |F_C|}{\sum |F_0|} \quad \text{for reflections with } F_0 > 4(\sigma(F_0))$$

$$S = \frac{\sum w(|F_0|^2 - |F_C|^2)^2}{(n-p)}$$

#### *2.4.3.1 (μ-OH)-(μ-η$^1$-O$_2$)-[(enN$_4$)$_2$Co$_2$](BF$_4$)$_3$(MeCN)$_2$(H$_2$O) (1(BF$_4$)$_3$)*

Crystals grew as clusters of prisms by vapor diffusion of $Et_2O$ into the MeCN solution of **1(BF$_4$)$_3$**. The analyzed crystal was cut from a larger crystal and had approximate dimensions of 0.48 × 0.26 × 0.21 mm. The data were collected on a Rigaku SCX-Mini diffractometer with a Mercury 2 CCD using a graphite monochromator with Mo Kα radiation (λ = 0.71075 Å). A total of 2160 frames of data were collected using θ-scans with a scan range of 0.5° and a counting time of 8 seconds per frame. The data were collected at 153 K using a Rigaku XStream low temperature device. Data reduction were performed using the Rigaku Americas Corporation's Crystal Clear version 1.40.[144] The structure was solved by direct methods using SIR97[145] and refined by full-matrix least-squares on $F^2$ with anisotropic displacement parameters for the non-H atoms using SHELXL-97.[146] Structure analysis was aided by use of the programs PLATON98[147] and WinGX.[148] The hydrogen atoms on carbon were calculated in ideal positions with isotropic displacement parameters set to 1.2 × $U_{eq}$ of the attached atom (1.5 × $U_{eq}$ for methyl hydrogen atoms). The hydrogen

atom on the hydroxyl group was observed in a ΔF map and refined with an isotropic displacement parameter.

The oxygen molecule bridging the two Co ions appeared to be slightly disordered. The disorder was modeled by assigning the variable x to the site occupancy factors to one set of oxygen atoms and (1-x) to the site occupancy factors for the alternate set. A common isotropic displacement parameter was refined for the four oxygen atoms while restraining the geometry of the molecule to be equivalent. In this way, the site occupancy for the major component of the disordered oxygen molecule consisting of atoms O12 and O13 refined to 89(2)%.

In addition, a partially occupied molecule of water was also located. This atom, O1w, was close enough to be H-bound to N1b and F12, but did not have enough $e^-$ density to constitute a fully occupied water molecule. Its occupancy was estimated to be close to 1/3 by fixing its isotropic displacement parameter to 0.05 while refining the site occupancy. No H atoms for this molecule were included in the final refinement model.

The function, $\Sigma w(|F_0|^2 - |F_C|^2)^2$, was minimized, where $w = 1/[(\sigma(F_0))^2 + (0.079*P)^2 + (3.118*P)]$ and $P = (|F_0|^2 + 2|F_C|^2)/3$. $R_w(F^2)$ refined to 0.176, with R(F) equal to 0.0634 and a goodness of fit, S, = 1.16. The data were checked for secondary extinction but no correction was necessary. Neutral atom scattering factors and values used to calculate the linear absorption coefficient are from the International Tables for X-ray Crystallography (1992).[149]

#### *2.4.3.2 (μ-OH)-(μ-η$^1$-$O_2$)-[$(enN_4)_2Co_2$]$(ClO_4)_3(MeCN)_2(H_2O)$ (1$(ClO_4)_3$)*

Crystals grew as large black prisms by slow evaporation from MeCN/toluene (3:1) solution of **1$(ClO_4)_3$** at 35 °C. The analyzed crystal was cut from a larger crystal and had approximate dimensions of 0.26 × 0.16 × 0.12 mm. The data were collected on a Rigaku

AFC12 diffractometer with a Saturn 724+ CCD using a graphite monochromator with Mo Kα radiation (λ = 0.71075Å). A total of 1632 frames of data were collected using θ-scans with a scan range of 0.5° and a counting time of 25 seconds per frame. The data were collected at 153 K using an Oxford Cryostream low temperature device. Data reduction were performed using the Rigaku Americas Corporation's Crystal Clear version 1.40.[144] The structure was solved by direct methods using SIR97[145] and refined by full-matrix least-squares on $F^2$ with anisotropic displacement parameters for the non-H atoms using SHELXL-97.[146] Structure analysis was aided by use of the programs PLATON98[147] and WinGX.[148] The hydrogen atoms on carbon were calculated in ideal positions with isotropic displacement parameters set to 1.2 × $U_{eq}$ of the attached atom (1.5 × $U_{eq}$ for methyl hydrogen atoms). The hydrogen atom on the hydroxide oxygen atom, O15, was observed in a ΔF and refined with an isotropic displacement parameter.

One of the hydrogen, H1wa, atoms on the oxygen atom of the water molecule, O1w, was found in the ΔF map. The hydrogen atom's bond length refined to >1 Å. In subsequent refinement models, the bond length was fixed at 0.80 Å. The displacement parameter for H1wa was set to 1.5 × $U_{eq}$ for that of O1w.

One of the perchlorate ions and the peroxide dianion were disordered. The disorder was modeled in the same manner for each anion. For example, in the perchlorate ion case, the site occupancy factor for one component was assigned the variable x, while the alternate component's site occupancy was set to (1-x). A common isotropic displacement parameter was assigned to the two Cl atoms, Cl3 and Cl3a. A separate isotropic displacement parameter was assigned to the oxygen atoms, O9, O10, O11 and O12 of one component and O9a, O10a, O11a and O12a to the second component. The geometry of the ions was restrained to be equivalent throughout the refinement. In this way, the site occupancy for the major component consisting of Cl3, O9, O10, O11 and O12 refined to 80(2)%. For the

peroxide ions, the site occupancy of the major component consisting of atoms, O13 and O14, refined to 91(2)%. The higher occupancy atoms of these anions were refined anisotropically with their displacement parameters restrained to be approximately isotropic in the final refinement model.

The function, $\Sigma w(|F_0|^2 - |F_C|^2)^2$, was minimized, where $w = 1/[(\sigma(F_0))^2 + (0.0385*P)^2 + (4.0847*P)]$ and $P = (|F_0|^2 + 2|F_C|^2)/3$. $R_w(F^2)$ refined to 0.111, with R(F) equal to 0.0455 and a goodness of fit, S = 1.09. The data were checked for secondary extinction effects but no correction was necessary. Neutral atom scattering factors and values used to calculate the linear absorption coefficient are from the International Tables for X-ray Crystallography (1992).[149]

#### *2.4.3.3 (μ-OH)-(μ-η $^1$-$O_2$)-[($enN_4$)$_2$$Co_2$]($PF_6$)$_3$ (1($PF_6$)$_3$)*

Crystals grew as needles by vapor diffusion of $Et_2O$ into the MeCN solution of **1($PF_6$)$_3$**. The analyzed crystal was cut from a cluster of crystals and had approximate dimensions of 0.32 × 0.15 × 0.08 mm. The data were collected on an Agilent Technologies SuperNova Dual Source diffractometer using a μ-focus Cu Kα radiation source (λ = 1.5418 Å) with collimating mirror monochromators. The data were collected at 100 K using an Oxford Cryostream low temperature device. Data collection, unit cell refinement and data reduction were performed using Agilent Technologies CrysAlisPro V 1.171.37.31.[150] The structure was solved by direct methods using SHELXT[151] and refined by full-matrix least-squares on $F^2$ with anisotropic displacement parameters for the non-H atoms using SHELXL-2014/7.[152] Structure analysis was aided by use of the programs PLATON98[147] and WinGX.[148] The hydrogen atoms were calculated in ideal positions with isotropic displacement parameters set to 1.2 × $U_{eq}$ of the attached atom (1.5 × $U_{eq}$ for methyl

hydrogen atoms). The data crystal was twinned with twin law determined using CrysAlisPro.

The function, $\Sigma w(|F_0|^2 - |F_C|^2)^2$, was minimized, where $w = 1/[(\sigma(F_0))^2 + (0.1132*P)^2 + (9.3992*P)]$ and $P = (|F_0|^2 + 2|F_C|^2)/3$. $R_w(F^2)$ refined to 0.189, with R(F) equal to 0.066 and a goodness of fit, S, = 1.03. The data were checked for secondary extinction effects but no correction was necessary. Neutral atom scattering factors and values used to calculate the linear absorption coefficient are from the International Tables for X-ray Crystallography (1992).[149]

### 2.4.4 Electrochemistry

Cyclic voltammograms were obtained on a Pine Wavenow potentiostat. The cell was constructed using a polished glassy carbon working electrode, platinum counter-electrode, and Ag wire reference electrode in 0.1 M TBAP solution in MeCN. The reported potentials are referenced versus ferrocene as internal standard. Standard CVs were obtained at 100 mV/s, except in scan rate dependence experiments (25-400 mV/s) (Figure 2.10).

### 2.4.5 Physical Measurements

$^1$H NMR spectra were collected on Varian DirecDrive 400 MHz spectrometer and chemical shifts were referenced to $CD_3CN$. UV/vis absorption spectra were obtained using Varian Cary 6000i spectrometer using ~0.1 mM solutions in 1 cm quartz cuvettes. Infrared spectra were recorded by using a Bruker Alpha spectrometer equipped with a diamond ATR crystal. EPR spectra were obtained by Bruker Biospin EMXplus 114 X-band spectrometer equipped with a liquid nitrogen cryostat. Elemental analysis was done by Midwest Micro Lab.

# Chapter 3: Fluoride-Bridged Dicobalt(II) Complexes via Spontaneous B–F Abstraction: Structures and Magnetism[b]

## 3.1 INTRODUCTION

### 3.1.1 Spontaneous Fluoride-Bridge Formation of Dicobalt Complexes

In addition to $\mu$-perxo dicobalt complexes discussed in Chapter 2, there are also a number of preceding examples of dinucleating cobalt(II) complexes that spontaneously form fluoride bridged structures as a result of fluoride abstraction from tetrafluoroborate ($BF_4^-$) anion (Figure 3.1). For example, Reaction of 3,5-diethyl-1,2,4-triazole with a series of cobalt(II) reagents yields the singly fluoride-bridged species $[Co_3(\mu\text{-}F)_2(detrH)_6(NCS)_4]$, wherein the bridging angle of Co–F–Co is 114.44°.[153,154] In related work, another series of mono-fluoride bridged dimers of general formula $[\mathbf{M}_2(\mu\text{-}F)(\mu\text{-}\mathbf{L_m}^*)_2](BF_4)_3$ was reported, where **M** = Fe(II), Co(II), Ni(II), Cu(II), Zn(II), and Cd(II) and $\mathbf{L_m}$ is *m*-bis[bis(3,5-dimethyl-1-pyrazolyl)-methyl]benzene (or, poly-(pyrazolyl)methane ligand).[155] These complexes have a linear M–F–M bridge and each M(II) center exhibits trigonal bipyramidal geometry. Separately, Meyer et al. characterized structures of dinuclear Co(II) complexes with bridging pyrazolate ligands and multidentate side arms, wherein the {N-Co-F-Co-N} unit forms a five-membered ring that is nearly coplanar with the bridging pyrazolate.[156] These researchers observed fluoride abstraction upon crystallization of the ion-exchanged reaction mixture, affording the final complex $[Co_2\mathbf{L^1}(\mu\text{-}F)](BPh_4)_2$, where $\mathbf{L^1}$ is $[3,5\text{-}(R_2NCH_2)_2C_3N_2H_2$, $R = Me_2N(CH_2)_3$.

The spontaneous formation of *bis*-fluoride bridged cobalt dimers has also been reported. In a remarkable reactivity study, Holland and coworkers found that reaction of

[b] Cho, Y. I.; Ward, M. L.; Rose, M. J. Substituent effects of N4 Schiff base ligands on the formation of fluoride-bridged dicobalt(II) complexes via B–F abstraction: structures and magnetism. *Dalt. Trans.* **2016**, *45* (34), 13466–13476. The author contributed as the first author in publishing this article.

fluorobenzene with a coordinatively unsaturated Co(I) complex ligated with bulky β-diketiminate undergoes binuclear oxidative addition to generate the 4-coordinate complex

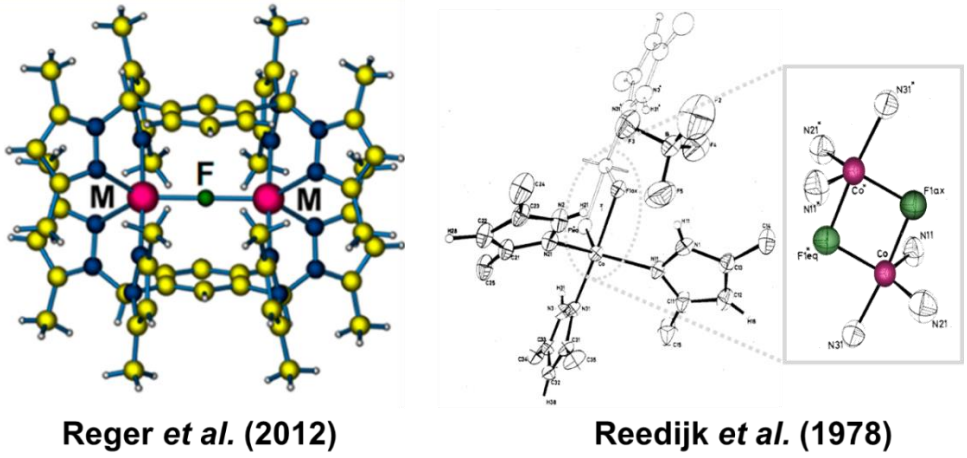


Figure 3.1: Examples of M($\mu$-F)M (left, M = Mn(II), Fe(II), Co(II), Ni(II), Cu(II), Zn(II), Cd(II)) and M($\mu$-F)$_2$M (right, M = Co(II)) from the literature.[155,157]

[$\mathbf{L}^{\mathbf{tBu}}$Co($\mu$-F)]$_2$, where $\mathbf{L}^{\mathbf{tBu}}$ = 2,2,6,6-tetramethyl-3,5-bis(2,4,6-triisopropylphenylimido)hept-4-yl.[158] Reedijk et al. reported the studies on [Co$_2$($\mu$-F)$_2$(DMPZ)$_3$](BF$_4$)$_2$ (DMPZ = 3,5-dimethylpyrazoles). Flourides from hydrated Co(BF$_4$)$_2$ abstracted during the reaction with DMPZ and small amount of triethyl orthoformate (dehydrating agent) in ethanol, forming Co($\mu$-F)$_2$Co in near trigonal bipyramidal symmetry around each metal center.[157] Additionally, several bis-tetradentate acyclic amine ligands provided a series of bipyridyl-type binding sites that afforded multinuclear (M = 4-6) metal complexes, which contain six-coordinate metal centers such as [Co$_4$($\mathbf{L}^{\mathbf{Et}}$)$_2$($\mu$-F)$_4$](BF$_4$)$_4$ and [Co$_4$-($\mathbf{L}^{\mathbf{Mix}}$)$_2$($\mu$-F)$_4$](BF$_4$)$_4$ where each set of two Co(II) centers are connected by two $\mu$-F bridges.[159,160] Inomata et al. reported a crystal structure of two octahedral Co(II) centers ligated with tris[(6-methylpyridin-2-yl)methyl]amine to afford [Co$_2$($\mu$-F)$_2$(C$_{21}$H$_{24}$N$_4$)$_2$](BF$_4$)$_2$, which exhibits doubly bridging $\mu$-F motifs.[161] Additionally, several Zn(II) and Cd(II) based dimers [M$_2$($\mu$-F)$_2$(L)](BF$_4$)$_2$ of a Schiff base expanded porphyrin

were studied by Sessler and coworkers.[162] Most importantly, except for [$\mathbf{L}^{\mathbf{tBu}}$Co($\mu$-F)]$_2$[158], the fluoride source for the $\mu$-F unit in all of the above cases was the tetrafluoroborate anion from the cobalt source [Co(OH$_2$)$_6$](BF$_4$)$_2$ (Zn(II) or Cd(II) in the case of Ref 162).

Although no precise mechanistic explanation has been elucidated so far for the spontaneous fluoride abstraction from tetrafluoroborate to generate M–F bridge(s), several plausible explanations are reported based on experimental observations. Goebeze et al. noted that the fluoride abstraction can occur in a protic solvent, such as methanol.[160] This is possibly due to the strong hydrogen-bonding interaction of $^{protic}$O-H•••F-BF$_3$. Others showed that in the presence of a strong base with bulky substituents (such as quinuclidine and 3,5-dimethylpyrazole), decomposition of tetrafluoroborate occurs and, as a result, metal-fluorides[163] or polymeric MF$_2$(ligand)$_2$ complexes[164] are generated.

### 3.1.2 Magnetic Properties of Known Metal-Fluoride Dimers

It is well known that halides – fluoride especially – can serve as effective conduits for magnetic coupling between metal centers. The magnetic properties of a number of fluoride- and difluoride-bridged cobalt dimers have been reported to exhibit varying extents of anti-ferromagnetic magnetic (AFM) coupling (Figure 3.2).

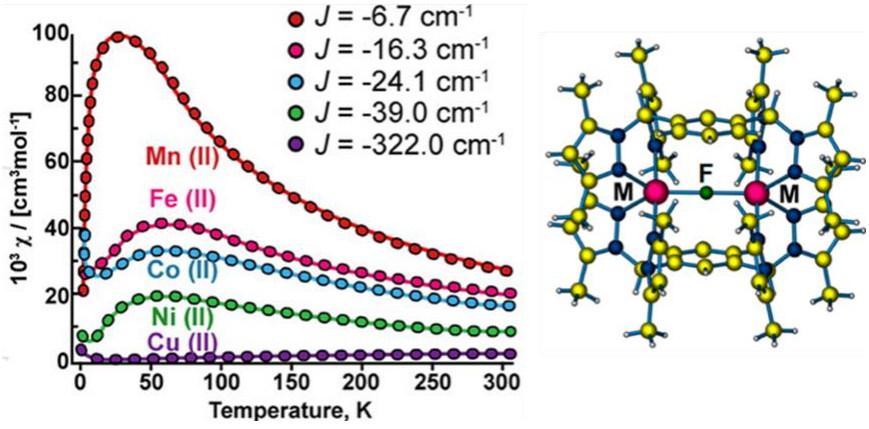

Figure 3.2: Magnetic susceptibility plots of M($\mu$-F)M complexes by Reger et al.[155]

Long and Reger described the *mono*-fluoride bridged cobalt dimer [$Co_2$($\mu$-F)($\mu$-**L**)]($BF_4$)$_3$, (where **L** = *m*-bis(dipz)$C_6H_4$) supported by a dinucleating tetrapyrazolylmethane ligand.[165] In solid state measurements, the dimer followed linear ($\chi^{-1}$ vs T) Curie-Weiss behavior between 300→40 K ($\mu_{eff}$ = 6.87 $\mu_B$ per $Co_2$; $\mu_{eff}$ = 4.86 $\mu_B$ per Co; $g$ = 2.45), and the plot exhibited an $x$-intercept at $\theta$ = –16 K, indicative of small extent of AF coupling ($J$ = –0.67 $cm^{-1}$). However, a methylated version of this dimer exhibited a much greater extent of AFM coupling ($J$ = –24.1 $cm^{-1}$). Indeed, these authors stated that "it has been noted that in intramolecular AFM exchange, interactions should be at a maximum in a bimetallic complex with a single bridging monoanionic ligand, X, when the M–X–M angle is 180°." Along these same lines, Miller and coworkers reported a Cr(III) dimer (also $S = {}^3/_2$ ions) with one nearly linear (179.85(12)°) bridging fluoride – namely [$Cr_2$($\mu$-F)(F)$_2$(TPA)$_2$]($BF_4$)$_3$ – which also exhibited a high extent of AFM coupling ($J$ = –13 $cm^{-1}$).

The *di*-fluoride bridged Cr(III) dimer [$Cr_2$($\mu$-F)$_2$(TPA)$_2$]($BF_4$)$_2$ exhibited greatly diminished coupling ($J$ = –1.53 $cm^{-1}$). Indeed, a number of *di*-fluoride bridged Co(II) dimers exhibit diminished AFM coupling across the $Co_2F_2$ diamond core, versus the linear $Co_2F$ motif. For example, Zsolnai and co-workers described a ($\mu$-F)($\mu$-pyrazolyl) Co(II) dimer that exhibited a $\theta$-value closer to zero ($\theta$ = –4.30 K), indicating an intermediate extent of AFM coupling. Brooker and co-workers investigated a series of phenylpyrimidine-bridged Co(II) dimers (all $S = {}^3/_2$ Co centers) – both with and without an additional $\mu$-F bridge. While the pyrimidine-bridged dimers exhibited weak AFM coupling ($J$ = –2.74, –2.87 $cm^{-1}$), the addition of a fluoride bridge greatly increased the AFM coupling ($J$ = –13.36 $cm^{-1}$).

However, there is at least one example of a transition metal dimer with a $M_2F_2$ diamond core that does not exhibit anti-ferromagnetic coupling. The copper(II) dimer $[Cu_2F_2(tmpz)_6](BF_4)_2$ (where tmpz = trimethylpyrazole) exhibits a magnetic susceptibility of $\mu_{eff} = 1.80\ \mu_B$ and a linear $\chi$•T plot with $\theta = 0$ K. The lack of AFM coupling in this case, however, was attributed to the exclusively axial orientation of the Cu(II) spin density in the $d_z^2$ orbital, which is perpendicular to the plane of $Cu_2F_2$ bonding. Thus, we hypothesized there would be significant AFM coupling of the two $S = {}^3/_2$ Co(II) centers with spin density along both the *z*-axis and *xy*-plane.

## 3.2 Results and Discussion

### 3.2.1 Synthesis Overview

A series of ligands was synthesized by modifying the **enN$_4$** ligand's (Chapter 2) (*i*) linker length from 2-carbon to 3-carbon (**pnN$_4$**) and/or (*ii*) the ortho-substituent (-H, -OMe and -PhCl) of pyridine rings (Figure 3.3). The initial purpose was to investigate the effect of ligand framework and substituents on the formation of related dicobalt peroxo structures. Modifications were thus introduced in the linker length — from 2-carbon to 3-carbon (**pnN$_4$**) to give more space and flexibility in between the metal centers — as well as the functionality at the ortho position (**pnN$_4$-OMe** and **pnN$_4$-PhCl**) to alter the steric and the electronic environment.

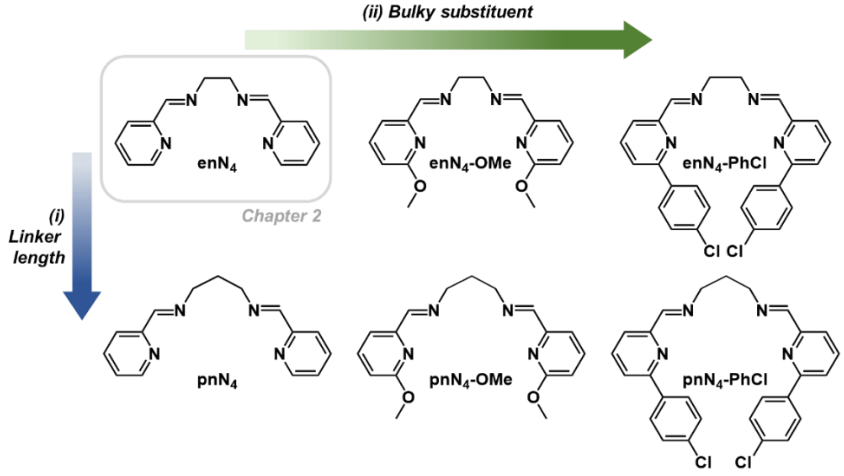


Figure 3.3: Structures of the ligands used in Chapter 3.

Complexation of the ligands with cobalt(II) hexahydrate salts gave unexpected results. The ligands **enN$_4$-OMe** and **enN$_4$-PhCl** yielded no isolable metal complex, whereas all of the 3-carbon-linker ligands, **pnN$_4$**, **pnN$_4$-OMe** and **pnN$_4$-PhCl,** afforded unexpected cobalt products (Scheme 3.1). Dimeric cobalt(II) complexes were produced with the ligands **pnN$_4$** and **pnN$_4$-PhCl**, whereas monomeric cobalt(II) complexes were synthesized from ligand **pnN$_4$-OMe** or a control reaction (only pyridine with no ligand).

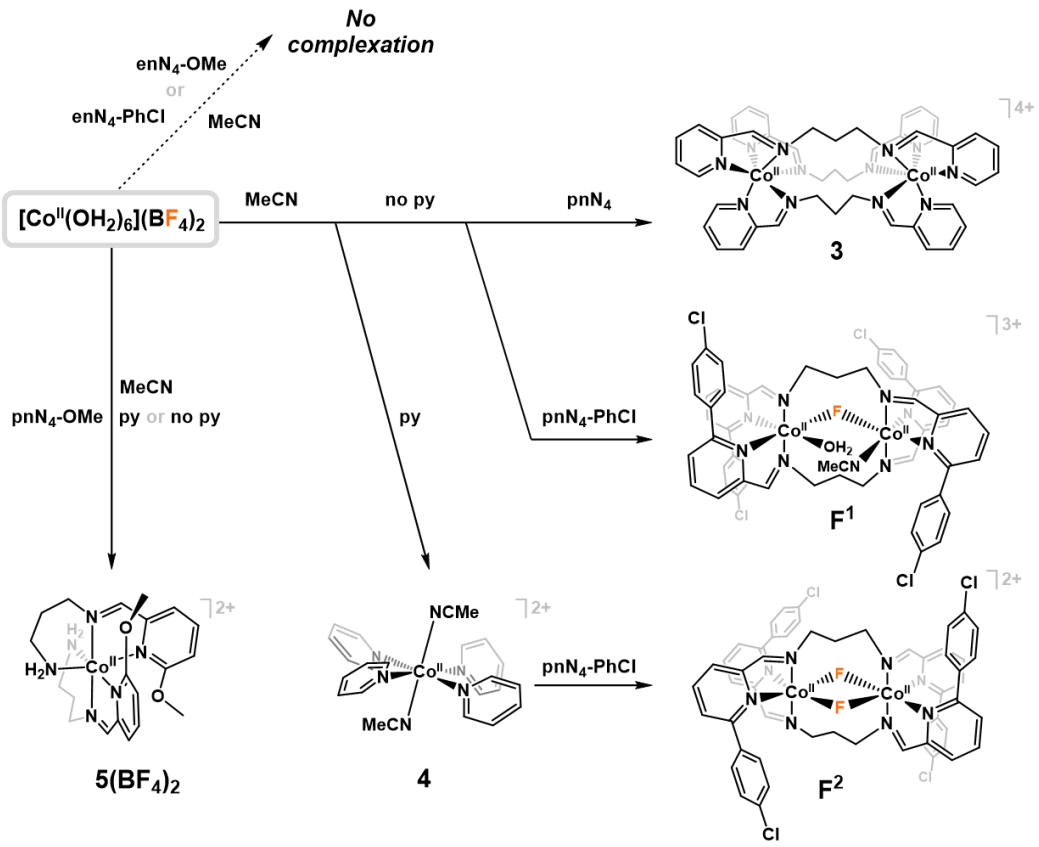


Scheme 3.1: Synthetic scheme depicting the isolation of the cobalt(II) monomers and dimers.

In the case of complexing **pnN$_4$-OMe** with [Co(OH$_2$)$_6$](X)$_2$ (X = BF$_4$ or ClO$_4$) the final crystal structure revealed hydrolysis of one arm of the **pnN$_4$-OMe** framework, thus forming a tridentate **pnN$_3$-OMe** ligand. As a result, two **pnN$_3$-OMe** units chelated a single 6-coordinate Co(II) center in [Co(pnN$_3$-OMe)$_2$](ClO$_4$)$_2$ (**5(ClO$_4$)$_2$**) to afford the bis-ligated species. (Crystallizations of the BF$_4^-$ version did not afford X-ray quality crystals.) The specific hydrolysis of only the **pnN$_4$-OMe** complex is likely due to its methoxy substituent, which is capable of H-bonding to adventitious water molecule(s), which could recruit H$_2$O solvates to the second coordination sphere of the complex, or stabilize a charged transition state or intermediate (e.g. tetrahedral oxyanion). In contrast, the aromatic or hydrocarbon-

only substituents of the other ligands (R = –H, –PhCl) do not H-bond, and therefore do not promote hydrolysis.

In contrast, complexation of the unsubstituted **pnN$_4$** ligand with the same cobalt source led to the formation of the 'non-bridged' cryptand-type dimer [Co$_2$(pnN$_4$)$_3$](BF$_4$)$_4$ (**3**). It thus appears that $O_2$ activation, which was observed in the case of **enN$_4$**, may be prevented by (*i*) the longer distance between cobalt ions, and (*ii*) the coordinatively saturated environment of each Co center in **3**. More specifically, the two cobalt(II) centers are coordinated by *three* total **pnN$_4$** ligands – in contrast to the Co$_2$ unit coordinated by *two* **enN$_4$** ligands in the cobalt-peroxo dimer (**1(BF$_4$)$_3$**).

Regarding the bulkiest of this series of ligands, **pnN$_4$-PhCl**, the identity of the metalation product was determined by the presence or absence of pyridine. First, reaction of **pnN$_4$-PhCl** *in the absence of pyridine* with a pink MeCN solution of [Co(OH$_2$)$_6$](BF$_4$)$_2$ generated a pale orange solution, from which we obtained pink crystals of the mono-fluoride bridged dimer [Co$_2$($\mu$-F)(pnN$_4$-PhCl)$_2$(OH$_2$)(MeCN)](BF$_4$)$_3$ (**F$^1$**), wherein one fluoride has been abstracted from the BF$_4$ anion (presumably generating 1 equiv of BF$_3$). The same reaction *in the presence of pyridine*, however, afforded a different product, namely the di-fluoride bridged dimer [Co$_2$($\mu$-F)$_2$(pnN$_4$-PhCl)$_2$](BF$_4$)$_2$ (**F$^2$**). From these two reactions, it was clear that pyridine was not *required* as a co-reagent to promote B–F bond cleavage.

To confirm that pyridine did not independently promote B–F bond cleavage, the simple complexation of [Co(OH$_2$)$_6$](BF$_4$)$_2$ with excess pyridine was performed. The straightforward isolation of the resulting coordination complex [Co(py)$_4$(MeCN)$_2$](BF$_4$)$_2$ (**4**) confirms that the simple combination of pyridine and Co(II)–BF$_4$ starting salt are not sufficient to promote the fluoride abstraction.[166] Direct reaction of **4** with **pnN$_4$-PhCl** (assisted by extra pyridine) in MeCN confirmed the formation of **F$^2$** via X-ray diffraction,

consistent with **4** as the intermediate species to form di-fluoride bridged dimer $\mathbf{F^2}$ from $[Co(OH_2)_6](BF_4)_2$.

In the absence of a rigorous mechanistic explanation for fluoride abstraction from tetrafluoroborate generating $\mu$-fluoride bridge(s), we postulated that the bulky chlorophenyl group stabilizes a transient and coordinatively unsaturated cobalt species, which reacts with the $BF_4$ anion to promote $F^-$ abstraction. Alternatively, the $\pi$ system of the –PhCl unit (not present in any of the other ligands used here) could bind or stabilize the $BF_4$ anion *or* the byproduct $BF_3$, thereby promoting the B–F bond cleavage. In contrast to previous reports where the metalation conditions (vide supra: protic solvent, base, etc.) were invoked as a factor in B–F cleavage, all of the metalation conditions in the present case were quite similar. Thus, the precise reason(s) for the B–F cleavage in the present case remain(s) unclear but is directly related to the identity of the N4 chelate.

In our case, the choice of **pnN$_4$**-type ligand controlled the $F^-$ abstraction. In particular, metalation of the unsubstituted **pnN$_4$** resulted in a symmetric Co(II) dimer, wherein the connectivity between the two cobalt centers is provided only by the three **pnN$_4$** ligands, rather than fluoride ion(s).

### 3.2.2 X-ray Structure of Metal Complexes

#### *3.2.2.1 [$Co_2$(μ-F)($pnN_4$-PhCl)$_2$($OH_2$)(MeCN)]($BF_4$)$_3$•(MeCN)$_2$ ($F^1$)*

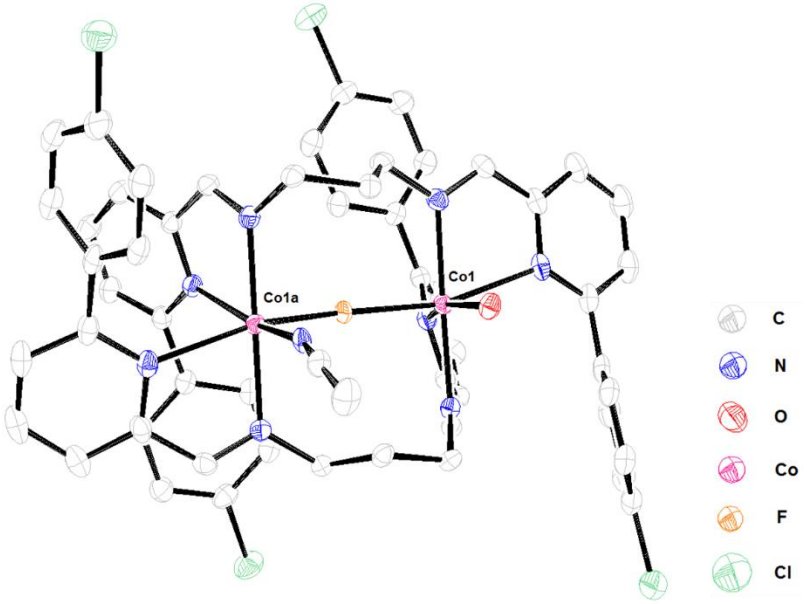


Figure 3.4: ORTEP diagram (50% ellipsoids) of the cation in [$Co_2$(μ-F)($pnN_4$-PhCl)$_2$($OH_2$)(MeCN)]($BF_4$)$_3$ (**$F^1$**). H's are not shown for sake of clarity.

In the structure of the (mono)fluoride-bridged dimer **$F^1$** (Figure 3.4), two **$pnN_4$-PhCl** ligands dinucleate the two pseudo-octahedral cobalt(II) centers in a 'criss-crossed' fashion, much like the 'criss-crossed' **$enN_4$**-based $Co_2$-peroxo dimer (**1($BF_4$)$_3$**) that served as inspiration for this work. The two cobalt centers are connected by a μ-flouride bridge, which was abstracted from the tetrafluoroborate anion. The three-carbon linkers on each ligand are folded toward the face/side where the solvents are occupied. On the ligand frame, the *ortho*-PhCl moiety is twisted out of planarity from the pyridine moiety, wherein the dihedral angle between the of the pyridine ring and *ortho*-PhCl is 133.5(2)°. The $N_{SB}$~$N_{py}$ link on the ligand generates a chelating pocket where it makes a stable five-membered ring when ligated with cobalt. Each center also has a solvent coordinating site, ligated to either MeCN (Co–$N_{MeCN}$ = 2.21(2) Å) or $H_2O$ (Co–O = 2.08(2) Å). The side where μ-flouride

bridge resides is hindered by the ligating $N_{py}$ donor groups and the bulky –PhCl groups, which facilitate a greater extent of open space that serves to allow solvent molecules to ligate. The $N_{SB}$ donors (from distinct ligands) are all arranged in trans orientation from one another, and the average Co–$N_{SB}$ bond distance is 2.105 Å. The angle of $N_{SB}$–Co–$N_{SB'}$ is 178.14(8)°, very close to linear geometry, and these two sets of $N_{SB}$–Co–$N_{SB'}$ are positioned nearly parallel to each other. The $N_{py}$ donors are trans from various ligands ($F^-$, MeCN, $OH_2$), but nonetheless reside within a narrow range of distances (2.25-2.28 Å) from the cobalt center; the average Co–$N_{py}$ distance is 2.269 Å, approximately 0.16 Å shorter than the Co–$N_{SB}$ distances. For all the previously known $Co_2(\mu$-F) complexes, aromatic N donors of the ligand(s) to the Co centers were from either pyrazole or triazole, not pyridine, and the average Co–$N_{pyr/tripyr}$ distances ranges from 1.945 to 2.172 Å (See Table 3.2).[153–156,165] The observed Co–F bond of **1** is 2.034(5) Å, which is within the normal range (1.96-2.077(3) Å)[153–156,165] but slightly above the average. The angle of Co–F–Co is 159.47(11)°, which provides steric relief for the binding of solvent molecules; it also separates the cobalt centers quite far way (Co•••Co ≈ 4.00 Å).

### *3.2.2.2 [$Co_2(\mu\text{-}F)_2(pnN_4\text{-}PhCl)_2](BF_4)_2$ ($F^2$)*

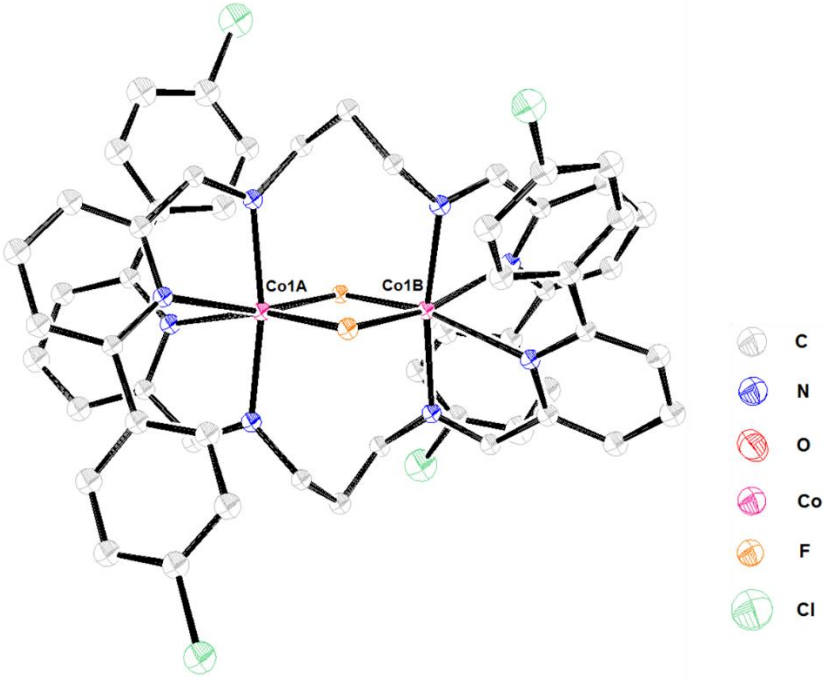


Figure 3.5: ORTEP diagram (50% ellipsoids) of the cation in $[Co_2(\mu\text{-}F)_2(pnN_4\text{-}PhCl)_2](BF_4)_2$ (**$F^2$**). H's are not shown for sake of clarity.

The overall structure of **$F^2$** (Figure 3.5) is analogous to that of **$F^1$**, except for the presence of the second $\mu$-flouride bridge in place of the two solvent molecules. As a result, complex **$F^2$** does not have distinguishable 'faces' since both sides are equally occupied by the two nearly 99°-angled $\mu$-fluoride bridges. The Co–F bond distances of 2.045(4) and 2.049(4) Å are slightly longer than that found in the linear Co–F unit found in **$F^1$** (2.034(5) Å). The acutely angled bridges bring the two cobalt centers closer together (3.109 Å) compared with that of **$F^1$** (4.003 Å). The average Co–F bond distances for the known $Co_2(\mu\text{-}F)_2$ complexes range from 2.036 to 2.196 Å, placing **$F^2$** in the lower range. This short bond distance is likely attributable to the tightly criss-crossing motif. Relatedly, the three-carbon linkers are perfectly criss-crossed when viewed down the plane formed by the two cobalt centers with two $\mu$-flouride bridges. The Co–$N_{SB}$ and Co–$N_{py}$ distances are each slightly

longer than the corresponding bond distances in **F**[1], but unremarkable: Co–$N_{SB}$(avg) = 2.121 Å; Co–$N_{py}$(avg) = 2.307 Å. The average Co–$N_{py}$ distances of the known $Co_2(\mu\text{-}F)_2$ complexes range from 2.129 to 2.214 Å (See Table 3.2).[159–161,167] Overall, the short Co–F bond distances and correspondingly long Co–$N_{py(ClPh)}$ bond distances suggest a push-pull effect wherein the steric repulsion of the bulky -PhCl unit drives the compression of all four Co–F bonds in $Co_2(\mu\text{-}F)_2$ core. Lastly, the -PhCl group from one ligand exhibits close π-π stacking (3.616 Å) with a pyridine moiety from the other ligand on the same Co center. Although they are not stacked directly on top of each other, they are aligned in parallel fashion (see spacefill representation, Figure 3.6).

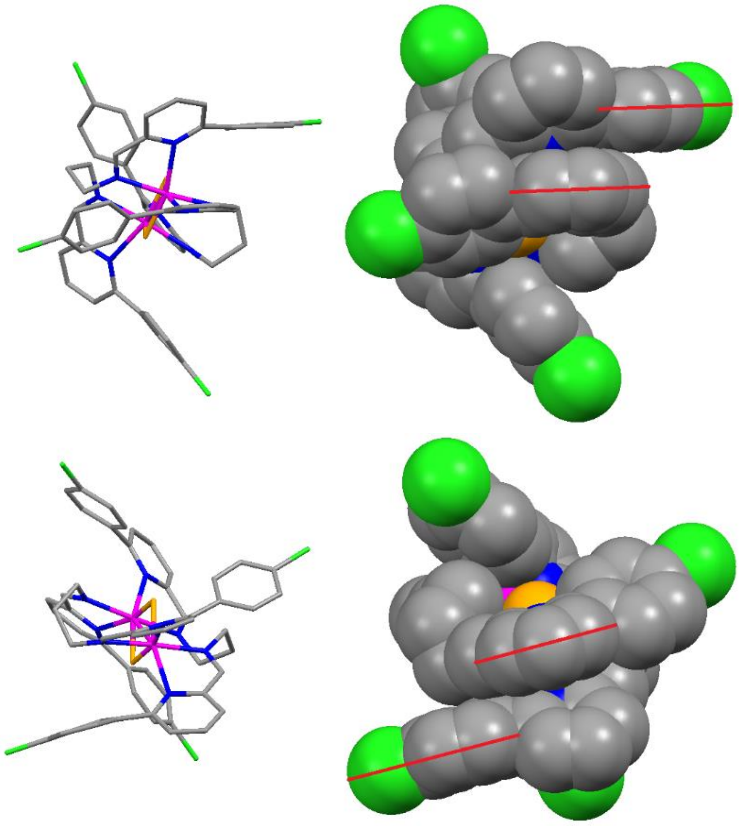

Figure 3.6: Capped stick and space-filling representations of complex **F**[2], illustrating the π-π interactions between ligands. Red lines represent the plane of the aromatic ring. The closest C•••C distance is 3.616 Å.

### *3.2.2.3 [$Co_2(pnN_4)_3$](BF$_4$)$_4$•(MeCN)$_3$•($H_2O$) (3)*

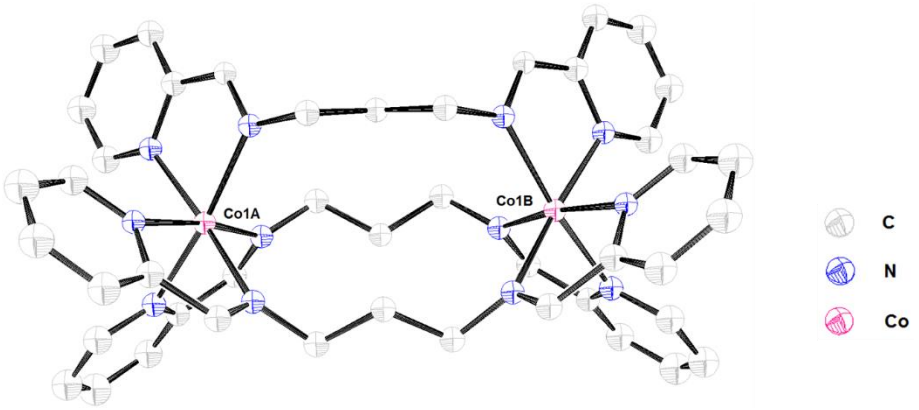


Figure 3.7: ORTEP diagram (50% ellipsoids) of the cation in [$Co_2(pnN_4)_3$](BF$_4$)$_4$ (**3**). H's are not shown for sake of clarity.

The tris-ligated dimer **3** (Figure 3.7) is characterized primarily by a much longer distance between cobalt centers – almost 7.0 Å. The propyl linker in each of the three **pnN$_4$** ligands is widely stretched out in a W-shape, and the two cobalt(II) centers are dinucleated at the opposite ends of the cryptand. Both cobalt centers exhibit pseudo-octahedral geometry, ligated with three sets of $N_{SB}$ and $N_{py}$ from the three ligands. Since the ligands are widely open, two cobalt centers are extremely far away from each other (6.801 Å) which is more than twice as long as the Co•••Co distance for **F$^2$**, and about 1.7 times than that of **F$^1$**. There is a (horizontal) paddlewheel-like 3-fold axis of *chemical* symmetry that along the axis between the two metal centers, and a 2-fold *crystallographic* symmetry as a (vertical) mirror plane between the two cobalt centers. While the average Co–$N_{SB}$ distance (2.151 Å) is comparable to those found in **F$^1$** and **F$^2$** (2.105, 2.121 Å), the absence of the fluoride or solvent molecules results in a much shorter average Co–$N_{py}$ distance of 2.160 Å.

### *3.2.2.4 [Co(py)$_4$(MeCN)$_2$](BF$_4$)$_2$ (4)*

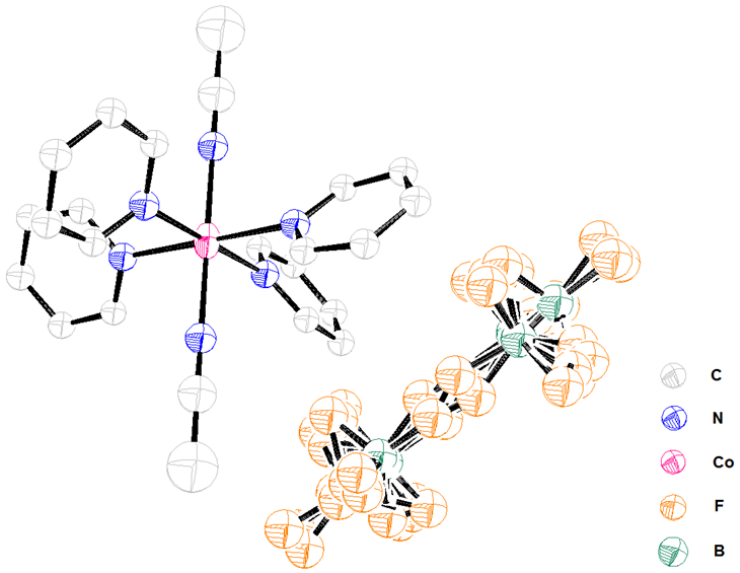


Figure 3.8: Full ORTEP diagram (50% ellipsoids) of [Co(py)$_4$(MeCN)$_2$](BF$_4$)$_2$ (**4**) including disorder model of the BF$_4$ counterions. H's are not shown for sake of clarity.

A simple reaction of [Co(OH$_2$)$_6$]BF$_4$ dissolved in MeCN and treated with excess pyridine afforded the tetrapyridine cobalt(II) complex **4** (Figure 3.8). The four equatorial pyridine molecules and two axial acetonitrile molecules are occupying the coordination sites on cobalt(II), along with two disordered tetrafluoroborate counter anions. The four pyridine moieties [Co–N$_{py}$ = 2.156(8) Å] are arranged in a propeller arrangement around the equatorial plane, wherein the torsion angle of each pyridine ring versus the *xy*-plane is 126.03°. The coordination geometry of the cobalt(II) center exhibits a nearly perfect square-bipyramidal geometry in terms of the bound N atoms: the N$_{py}$–Co–N$_{py}$ angle is 90.003(1)°, while the N$_{py}$–Co–N$_{MeCN.}$ angle is 90.000(1)°, and the angles of all the trans-positioned N donors with Co are 180.0°.

### *3.2.2.5 [Co(pnN$_3$-OMe)$_2$](ClO$_4$)$_2$ (5(ClO$_4$)$_2$)*

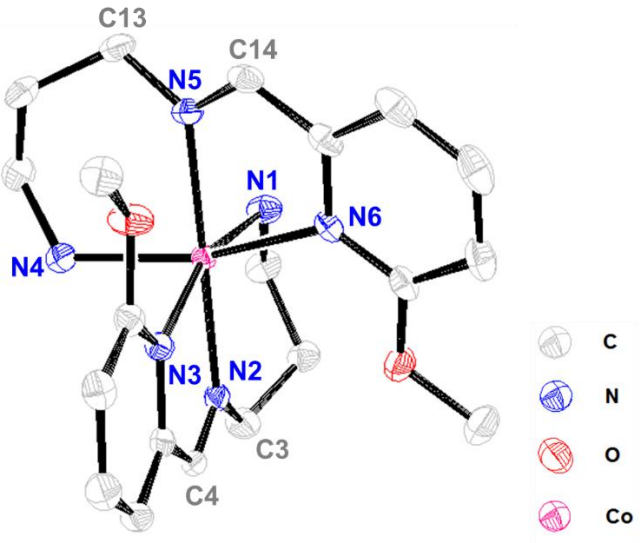


Figure 3.9: ORTEP diagram (50% ellipsoids) of the cation in [Co(pnN$_3$-OMe)$_2$](ClO$_4$)$_2$ (**5(ClO$_4$)$_2$**). H's are not shown for sake of clarity.

The cobalt(II) center of another monomer **5(ClO$_4$)$_2$** is ligated by six N donor atoms from two spontaneously half-hydrolyzed-pnN$_3$-OMe ligands (originally **pnN$_4$-OMe**). Each ligand is bound in meridional fashion. The methoxy-oxygens do not participate in coordination, making the two O$^{methoxy}$•••Co distances 3.27 and 3.28 Å. The methyl groups on those oxygens are pointing away from the cobalt center. Although the half of the ligand is hydrolyzed, the other half is intact as a Schiff-base, keeping the C4–N2 and and C14–N5 as double bonds with 1.267(3) Å and 1.270(3) Å, respectively.

### *3.2.2.6 Overall*

Selected bond distances and angles for complexes **F[1]**, **F[2]**, **3** and **4** are listed in Table 3.1. Considering the Co–$N_{py}$ distance 2.156(8) Å of **4** as the standard (i.e. the 'ideal' pyridine distance in absence of a chelate), the non-fluoride bridged dimer **3** exhibits the closest Co–$N_{py}$ distance (avg = 2.160 Å), whereas the fluoride-bridged dimers **F[1]** and **F[2]** have significantly longer average distances (2.269 Å and 2.307 Å, respectively). Having no other substituents except for the Schiff-base linker on the pyridine rings, **pnN$_4$** most closely resembles the coordination environment in **4**. Although an equivocal conclusion cannot be made in the absence of a **pnN$_4$-PhCl**-based structure without fluoride bridge(s), it is likely that the bulky -PhCl substituents cause some steric repulsion close to the metal center and surrounding ligands. In support of this claim, it is notable that while the reported manganese carbonyl complex [($N_{Me}$NS)Mn(CO)$_2$(Br)] exhibits a standard Mn–$N_{py}$ bond length (1.987(2) Å), substitution of the bulky -PhF unit at the ortho position elongates the Mn–$N_{py}$ bond significantly (2.100(4) Å).[168]

| Complex | Co•••Co | Co–$N_{SB}$ | Co–$N_{py}$ | Co–F | ∠Co-F-Co |
|---|---|---|---|---|---|
| [$Co_2$($\mu$-F)(pn$N_4$-PhCl)$_2$($OH_2$)(MeCN)]($BF_4$)$_3$ (**F[1]**) | 4.003 | 2.103(2)<br>2.107(2) | 2.2559(19)<br>2.282(2) | 2.034(5) | 159.47(11) |
| [$Co_2$($\mu$-F)$_2$(pn$N_4$-PhCl)$_2$]($BF_4$)$_2$ (**F[2]**) | 3.109 | 2.115(4)<br>2.127(4) | 2.288(4)<br>2.326(4) | 2.045(4)<br>2.049(4) | 98.8(2)<br>99.1(2) |
| [$Co_2$(pn$N_4$)$_3$]($BF_4$)$_4$ (**3**) | 6.801 | 2.141(7)<br>2.144(7)<br>2.168(7) | 2.154(7)<br>2.160(7)<br>2.166(7) | –<br>–<br>– | –<br>–<br>– |
| [Co(py)$_4$(MeCN)$_2$]($BF_4$)$_2$ (**4**) | – | – | 2.156(8) | – | – |

Table 3.1: Selected bond distances (Å) and angles (°) for [$Co_2$($\mu$-F)(pn$N_4$-PhCl)$_2$($OH_2$)(MeCN)]($BF_4$)$_3$ (**F[1]**), [$Co_2$($\mu$-F)$_2$(pn$N_4$-PhCl)$_2$]($BF_4$)$_2$ (**F[2]**), [$Co_2$(pn$N_4$)$_3$]($BF_4$)$_4$ (**3**) and [Co(py)$_4$(MeCN)$_2$]($BF_4$)$_2$ (**4**).

| Reference No. | Chemical Formula | M•••M | M-N* | M-$N_{py}$ | M-$N_{pyr}$ | M-F | ∠M-F-M |
|---|---|---|---|---|---|---|---|
| This work | $[Co_2(\mu\text{-}F)(pnN_4\text{-}PhCl)_2(OH_2)(MeCN)](BF_4)_3$ (**F$^1$**) | 4.003 | *Schiff-base: 2.103(2), 2.107(2) | 2.2559(19), 2.282(2) | – | 2.034(5) | 159.47(11) |
| 155 | $[Co_2(\mu\text{-}F)(\mu\text{-}L_m*)_2](BF_4)_3$ | 4.13 | – | – | *pyrazole: avg: 2.099 | 2.0626(4) | 180.00 |
| 165 | $[Co_2(\mu\text{-}F)(\mu\text{-}L_m)_2](BF_4)_3$ | 3.90 | – | – | *pyrazole: avg: 2.09 | 1.9521(4), 1.9774(4) avg: 1.96 | 180 |
| 156 | $[Co_2(\mu\text{-}Br)L^1](BPh_4)_2$ | 3.577 | – | – | 1.944(1), 1.945(4) | 2.077(3) | 118.9(2) |
| 153 | $[Co_3(\mu\text{-}F)_2(detrH)_6(NCS)_4](H_2O)_2$ | 3.3726(3) | – | – | *triazole: 2.137(2)-2.206(2) | 1.992(1)-2.019(1) avg: 2.006 | 114.44(7) |
| 154 | $[Co_3(\mu\text{-}F)_2(tmtr)_4(NCS)_4(H_2O)_2](H_2O)_4$ | 3.4015(3) | – | – | *triazole: 2.131(2), 2.152(2), 2.168(2), 2.172(2) | 2.023(1), 2.058(2) avg: 2.041 | 112.92(7) |
| 169 | $[Cr_2(\mu\text{-}F)(F)_2(TPyA)_2](BF_4)_3$ | 3.862 | *amine 2.059, 2.065 | 2.016, 2.042 | – | 1.977(16), 1.9347(16) | 179.85(12) |
| This work | $[Co_2(\mu\text{-}F)_2(pnN_4\text{-}PhCl)_2](BF_4)_2$ (**F$^2$**) | 3.109 | *Schiff-base: 2.2.115(4), 2.127(4) | 2.288(4), 2.326(4) | – | 2.045(4), 2.049(4) | 98.8(2), 99.1(2) |
| 160 | $[Co_4(L^{Mix})_2(F)_4](BF_4)_4$ | 3.114(9) | *amine: 2.127(5), 2.139(4) mean: 2.129 | 2.100(4)-2.162(4) mean: 2.129 | *pyrimidine: 2.233(4), 2.227(4) mean: 2.230 | 1.987(3)-2.086(3) mean: 2.036 | 100.0(1), 99.4(1) |
| 159 | $[Co_4(L^{Et})_2(F)_4](BF_4)_4$ | 3.194(5) | 2.161(2), 2.177(2) mean: 2.169 | 2.134(2)-2.198(2) avg: 2.155 | *pyrimidine: 2.390(2), 2.316(2) mean: 2.353 | 1.992(1)-2.095(1) mean: 2.049 | 100.64(5), 104.29(5) |
| 170 | $[Co_2F_2(dmpz)_6](BF_4)_2$ | 3.092(2) | – | – | 2.033(5), 2.040(5), 2.042(6) | 1.924(4), 2.146(4) | 98.8(2) |
| 158 | $[L^{tBu}Co(\mu\text{-}F)]_2$ | 3.062 | *amine: 1.952, 1.974 | – | – | 1.860, 1.988 | 105.43 |
| 167 | $[Co_6L_4(\mu\text{-}F)_2](BF_4)_{10}$ | 3.143 | – | 2.127(6)-2.208(13) avg: 2.172 | 2.093(12)-2.190(9) | 2.035(6)-2.058(5) avg: 2.047 | 100.18, 100.36 |
| 161 | $[Co_2(\mu\text{-}F)_2L_2](BF_4)_2$ | 3.157 | *amine: 2.124(3) | 2.143(3), 2.249(3), 2.251(3) | – | 1.985(2), 2.098(2) avg: 2.196 | 101.24 |
| 171 | $[L^{Me}Fe(\mu\text{-}F)]_2$ | 3.0831(6) | *diketiminate 2.0081(18), 2.0161(17) | – | – | 1.9757(12), 1.9774(14) | 102.44(10), 102.56(9) |
| 172 | $[Cu_2(\mu\text{-}F)_2(tmpz)_6](BF_4)_2$ | 3.0141(8) | – | – | 2.103(3), 2.009(3), 1.965(3) | 2.183(2), 1.911(2) | 94.59(7) |
| 173 | $[Cu_2F_2(bnpy_2)_2](PF_6)_2$ | 3.137(1) | *amine: 2.064 | 2.014, 2.019 | – | 1.918(2), 2.232(2) | 97.97 |
| This work | $[Co_2(pnN_4)_3](BF_4)_4$ (**3**) | 6.801 | *Schiff-base: 2.141(7), 2.144(7), 2.168(7) | 2.154(7), 2.160(7), 2.166(7) | – | – | – |
| This work | $[Co(py)_4(MeCN)_2](BF_4)_2$ (**4**) | – | – | 2.156(8) | – | – | – |

Table 3.2: Selected bond distances (Å) and angles (°) for dimers with $\mu$-F bridge(s) reported here and in literature.

### 3.2.3 Magnetism

#### *3.2.3.1 Experimental and Simulated Magnetic Susceptibilities of $F^1$ and $F^2$*

The temperature-dependent magnetic susceptibilities of dimers $\mathbf{F^1}$ and $\mathbf{F^2}$ were obtained. The χ vs T plots for both dimers are shown in Figure 3.10 (A for $\mathbf{F^1}$; B for $\mathbf{F^2}$), which were obtained from 300 to 2 K at 1000 G. From 300 to 50 K for $\mathbf{F^1}$, the magnetic susceptibility steadily increases from 0.015 to 0.028 emu $mol^{-1}$. (Figure 3.10A) This is nearly identical to the range exhibited by the mono-fluoride dimer $[Co_2(\mu\text{-}F)(\mu\text{-}\mathbf{L})](BF_4)_3$ reported by Reger and Ozarowski (0.015 to 0.035 emu $mol^{-1}$).[155] Following a small decrease in χ near 30 K, the χ value rises rapidly approaching 0 K (0.05 emu $mol^{-1}$); the aforementioned cobalt dimer followed a similar pattern, approaching 0.04 emu $mol^{-1}$ near 0 K. The corresponding data in the χT vs T plot (inset, Figure 3.10A) can be readily simulated by the modified van Vleck equation for a symmetric system of two $S = {}^3/_2$ ions (where $c$ = TIP = 0.00155 emu $mol^{-1}$).[174]

$$\chi = \frac{N_A \mu_B^2 g^2}{3k_B T} \frac{\left\{82 \exp\left({}^{12J}/_{k_B T}\right) + 30 \exp\left({}^{6J}/_{k_B T}\right) + 6 \exp\left({}^{2J}/_{k_B T}\right)\right\}}{\left\{7 \exp\left({}^{12J}/_{k_B T}\right) + 5 \exp\left({}^{6J}/_{k_B T}\right) + 3 \exp\left({}^{2J}/_{k_B T}\right) + 1\right\}} + c \qquad \text{(Eq. 3.1)}$$

The best-fit AFM coupling constant of $J = -14.9$ $cm^{-1}$ for $\mathbf{F^1}$ is comparable to other strongly AFM coupled systems with nearly linear Co–F–Co angles ($J \approx -10$ to $-25$ $cm^{-1}$). Additionally, the simulated $g$ value of 2.34 is within the range of other singly-fluoride bridged cobalt(II) dimers, which span a narrow range of $g$ = 2.26 to 2.45.[155,165] The effective magnetic moment at 300 K was determined to be $\mu_{eff} = 6.07\ \mu_B$ (SQUID, 1000 G; Figure B.4, right); benchtop, $\mu_{eff} = 6.24\ \mu_B$.

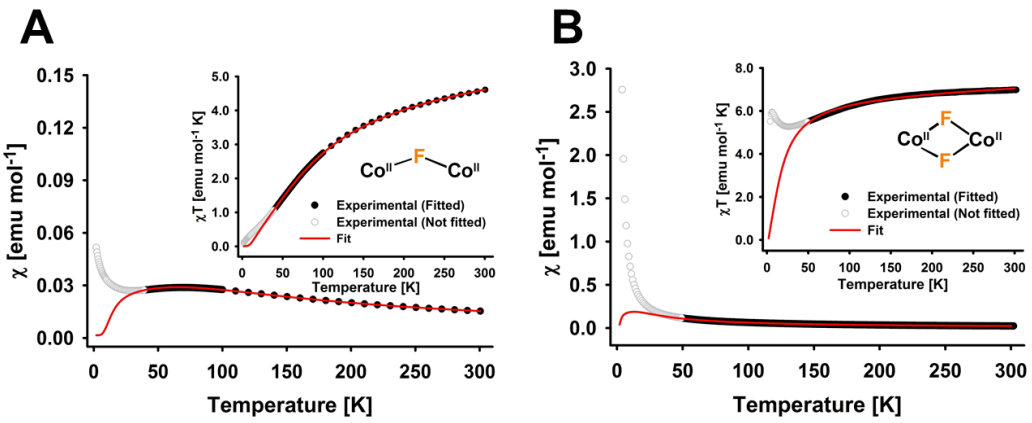


Figure 3.10: Plots of χ vs T for $\mathbf{F^1}$ (A) and $\mathbf{F^2}$ (B). *Insets:* The corresponding χT vs T plots. *Experiment conditions:* 2 → 300 K at 1000 G. Solid red line represents the best fit for the modified van Vleck formula using *J* and *g* values as variables. Black circles represent the experimental data was fit by the simulation; gray open circles represent experimental data that was not fit by the simulation.

One notable discrepancy between the simulation and the experimental data for $\mathbf{F^1}$ is clearly observed at low temperatures in the χ vs T plot. Indeed, such a deviation from simple AFM coupling was also observed in the dinucleating dmpz system.[155] The authors attributed such anomalous behavior at low temperatures to the large zero field splitting in the excited paramagnetic states. Such a phenomenon is not accounted for by the modified van Vleck dimer equation used here, and instead requires full diagonalization of the Hamiltonian in higher order matrices; at present, no analytical formula is available for cobalt(II) dimers with significant zero-field splitting contributions. However, from the clear agreement of the simulation with experimental data above 50 K, our derived *J* and *g* values in the present analysis appear valid.

### *3.2.3.2 Comparison of J and g Values for $F^1$ and $F^2$*

In contrast to **F¹**, the χ vs T plot for **F²** exhibits values in the range of 0.02 to 0.11 emu $mol^{-1}$ from 300 to 50 K; the latter value is greater than that for **F¹** at the same temperature (0.028 emu $mol^{-1}$). Like **F¹**, dimer **F²** also exhibits an exponential increase in χ below 30 K that is not accounted for by the van Vleck dimer formula. Nonetheless, both the χ vs T and χT vs T plots are well-simulated by the equation above 50 K. For di-fluoride bridged **F²**, the simulated AFM coupling constant of $J = -2.97$ $cm^{-1}$ is significantly weaker than that for **F¹** ($J = -14.9$ $cm^{-1}$). This is expected based on the significant deviation from 180° of the $Co_2F_2$ diamond core (X-ray for **2**: ∠Co–F–Co = 98.8(2), 99.1(2)°), as compared with the corresponding Co–F–Co angle found in **F¹** (159.47(11)°). In this structural respect, it is not surprising that the AFM coupling constant for **F¹** is notably weaker than that of one of the strongest AFM couplings ($J = -24.1$ $cm^{-1}$; ∠Co–F–Co = 180°, crystallographically defined). Interestingly, the simulated *g* value for **F²** ($g = 2.72$) is significantly higher than that for **F¹** ($g = 2.34$), and quite similar to a number of known di-fluoride bridged cobalt(II) dimers ($g = 2.62$ to 2.74). Such a consistently higher *g* value in the case of di-fluoride bridged dimers may be due to the inherently greater symmetry in the coordination environment, thus leading to greater orbital angular momentum effects (vide infra).

### *3.2.3.3 Origins of Magnetic Parameters*

The present data and the accumulated data in Table 3.3 warrant a discussion of the origin of the experimentally determined *g* values. The *g* value for a greater than half-filled $^4T_{1g}$ single ion is classically given by Equations 3.2-4:[175]

$$g = 2.00(1 - \frac{4\lambda}{10Dq}) \qquad \text{(Eq. 3.2)}$$

$$\lambda\,(^4T_{1g}) = -\xi/3 \qquad \text{(Eq. 3.3)}$$

$$g = 2.00(1 + \frac{4\xi}{3\times 10Dq}) \qquad \text{(Eq. 3.4)}$$

First, Eq 3.4 is in that notable that *g* is proportional to $\xi$ (the spin-orbit coupling parameter). In a purely $O_h$ $^4T_{1g}$ system, the spin-orbit coupling constant is quite high due to the high orbital angular momentum of the unpaired $t_{2g}$ electron across the degenerate $t_{2g}$ set. This effect is amplified by the high spin of the complex ($\boldsymbol{L \bullet S = J}$). As a complex moves away from pure $O_h$ symmetry, the orbital angular momentum decreases due to the loss of degeneracy in the $t_{2g}$ set. Therefore, higher symmetry in the coordination environment generally results in a higher $\xi$ parameter, and a correspondingly higher *g* value. Another factor governing the *g* value is 10Dq. In our systems, the main difference between the two complexes (in terms of ligand donor strength) is the number of bridging $F^-$ ligands per Co(II) center. Fluoride is one of the weakest ligands in the spectrochemical series, especially compared to nitrogen-donating ligands with π acid character (pyridine and Schiff base). Thus, more coordinated $F^-$ ions will lower the 10Dq value of the complex, thus contributing to a higher *g* value.

| Reference No. | Chemical Formula | Core | Donor Set on each Metal | Geometry | ∠Co–F–Co (°) | $J$ ($cm^{-1}$) | $g$ |
|---|---|---|---|---|---|---|---|
| This work | $[Co_2(\mu\text{-}F)(pnN_4\text{-}PhCl)_2(OH_2)(MeCN)](BF_4)_3$ (**F[1]**) | Co($\mu$-F)Co | N5F1 N4O1F1 | $O_h$ | 159.47(11) | –14.9 | 2.34 |
| 155 | $[Co_2(\mu\text{-}F)(\mu\text{-}L_m*)_2](BF_4)_3$ | Co($\mu$-F)Co | N4F1 | TBP | 180.00 | –24.1(5) | 2.26 |
| 165 | $[Co_2(\mu\text{-}F)(\mu\text{-}L_m)_2](BF_4)_3$ | Co($\mu$-F)Co | N4F1 | TBP | 180 | –0.67(5) | 2.45(1) |
| 156 | $[Co_2(\mu\text{-}Br)L^1](BPh_4)_2$ | Co($\mu$-Br)Co | N4Br1 | Distorted TBP | 118.9(2) | $-1<J<0$ | - |
| 169 | $[Cr_2(\mu\text{-}F)(F)_2(TPyA)_2](BF_4)_3$ | Cr($\mu$-F)Cr | N4F2 | $O_h$ | 179.85(12) | –13 | 2.00 |
| This work | $[Co_2(\mu\text{-}F)_2(pnN_4\text{-}PhCl)_2](BF_4)_2$ (**F[2]**) | Co($\mu$-F)$_2$Co | N4F2 | $O_h$ | 98.8(2) 99.1(2) | –2.97 | 2.72 |
| 160 | $[Co_4(L^{Mix})_2(F)_4](BF_4)_4$ | [Co($\mu$-F)$_2$Co]$_2$ | N4F2 | $O_h$ | 100.0(1) 99.4(1) | –13.36 | 2.62 |
| 159 | $[Co_4(L^{Et})_2(F)_4](BF_4)_4$ | [Co($\mu$-F)$_2$Co]$_2$ | N4F2 | $O_h$ | 100.64(5) 104.29(5) | –3.85 | 2.74 |
| 161 | $[Co_2(\mu\text{-}F)_2L_2](BF_4)_2$ | Co($\mu$-F)$_2$Co | N4F2 | $O_h$ | 101.24 | - | - |

Table 3.3: Magnetic properties and geometry information of the dicobalt-fluoride complexes.

### *3.2.3.4 J and g Values: Comparison to literature*

Dimer **F²**. Brooker and coworkers studied tetranuclear cobalt complexes that have two sets of non-interacting Co($\mu$-F)$_2$Co cores in each complex (See Table 3.3).[159,160] Each cobalt center has an N4F2 donor set with octahedral geometry analogous to dimer **F²**. The observed *g* values for two examples of this type of 'dimer of dimers' were 2.62 and 2.74, which are comparable to that of dimer **F²** ($g$ = 2.72). The collection of rather high *g* values reflects a narrow range (very similar coordination environments), and is likely attributable to both the weak ligand fields (two $F^-$ bridges) and the relatively symmetric ligand fields ($C_2$ axes). Turning to the coupling constants, the *J* values for the tetranuclear examples reported by Brooker were –13.36 and –3.85 cm$^{-1}$. The latter example, namely [Co$_4$(L$^{Et}$)$_2$(F)$_4$](BF$_4$)$_4$, showed a coupling constant very close to dimer **F²** ($J$ = –2.97 cm$^{-1}$). These rather small coupling constant values are attributable to the acute Co$_2$F$_2$ diamond core: the Co–F–Co angles deviate greatly from 180°: 100.64(5)° and 104.29(5)° for [Co$_4$(L$^{Et}$)$_2$(F)$_4$](BF$_4$)$_4$; 98.9(2)° and 99.1(2)° for dimer **F²** (See Table 3.3).

Dimer **F¹**. For the mono-fluoride-bridged dimer **F¹**, two similar Co($\mu$-F)Co complexes studied by Reger and coworkers exhibit comparable *J* and *g* values, although their ligation environment is not strictly the same.[155,165] Both complexes share the same chemical formula of [Co$_2$($\mu$-F)($\mu$-**L**)$_2$](BF$_4$)$_3$, where **L** is either **L$_m$**, *m*-bis[bis(pyrazolyl)methyl], or benezene **L$_m$***, *m*-bis[bis(3,5-dimethyl-1-pyrazolyl)methyl]benzene. However, each cobalt center exhibits a trigonal bipyramidal (TBP) geometry rather than $O_h$. This results in the ideal, linear Co–F–Co bridge (180.0°), thus producing very strong AFM coupling ($J$ = –24.1(5) cm$^{-1}$). In comparison, dimer **F¹** exhibits a slightly lower AFM coupling constant ($J$ = –14.9 cm$^{-1}$), likely due the slightly acute ∠Co–F–Co of 159.47(11)° (~20° less than Reger's complex, Table 3). Notably, the

$g$ value determined for $\mathbf{F^1}$ ($g$ = 2.34) is quite close to those determined for the two TBP Co(II) dimers ($g$ = 2.26 and 2.45(1)). We also considered a structurally and electronically related mono-fluoride bridged chromium complex, namely $[Cr_2(\mu\text{-}F)(F)_2(TPyA)_2](BF_4)_3$, reported by Miller and coworkers.[169] The approximately $O_h$ Cr(III) centers exhibit the analogous AFM-coupled $S = {}^3/_2$ metal ions ($J$ = –13 cm$^{-1}$, ∠Cr–F–Cr = 179.85(12)), but instead emanating from a $^4A_{2g}$ ground term ($\boldsymbol{L} \approx 0 \rightarrow \boldsymbol{J} \approx 0$) rather than $^4T_{1g}$ as in the case of cobalt. The chromium dimer exhibited a notably smaller $g$ value (2.00), again providing evidence that $g > 2.0$ for $\mathbf{F^1}$ and $g >> 2.0$ for $\mathbf{F^2}$ plausibly result from greater contributions from the $\xi$ parameter.

Regarding the structural properties of $\mathbf{F^1}$, closer inspection of the individual Co centers reveals a donor set comprised of one F$^-$, four N donors (two $N_{py}$ and two $N_{SB}$) that and the last site is either a nitrogen donor (MeCN) or an oxygen donor ($H_2O$). This mixed N4FO or $N5FN_{MeCN}$ coordination sphere lowers the symmetry around the Co(II) center – both at the individual metal centers, as well as in the dimer as a whole (i.e. the dimer is not centrosymmetric, $C_{2v}$ or even $C_2$), thereby lowering contributions to $g$ from the $\xi$ parameter. Additionally, dimer $\mathbf{F^1}$ has only one weak-field F$^-$ ligand, resulting in a larger 10Dq (compared to $\mathbf{F^2}$), which is again correlated to a lower $g$-value (for $\mathbf{F^1}$: $g$ = 2.34; for $\mathbf{F^2}$: $g$ = 2.72). In contrast, dimer **2** has two coordinated F$^-$ ions resulting in a smaller 10Dq value at each metal center. Additionally, the N4F2 donor set provides approximate local $C_{2V}$ symmetry at each metal center; this imposes higher symmetry, greater $t_2$ set orbital degeneracy, and a correspondingly higher $\xi$ value. Thus, the best-fit $g$ value for $\mathbf{F^2}$ is predictably greater than that for $\mathbf{F^1}$.

## 3.3 CONCLUSIONS

In summary, this work shows that the combination of $[Co(H_2O)_6](BF_4)_2$ plus pyridine is not sufficient to promote B–F bond cleavage, instead leading to the formation of the structurally characterized species $[Co(py)_4(MeCN)_2](BF_4)_2$. In addition, the unsubstituted ligand **pnN$_4$** is not sufficient for B–F bond cleavage, resulting in a dicobalt(II) complex with non-coupled metal centers (Co•••Co = 6.801 Å). On the other hand, the sterically hindered ligand **pnN$_4$-PhCl** in the absence of pyridine promotes a single B–F cleavage event, leading to the formation of the mono-fluoride bridged cobalt(II) dimer **F$^1$**. Reaction of this bulky ligand **pnN$_4$-PhCl** with the pyridine-bound Co(II) precursor promotes two B–F cleavage events, leading to isolation of the di-fluoride bridged species **F$^2$**.

The linearly mono-fluoride bridged dimer **F$^1$** exhibits strong AFM coupling ($J$ = –14.9 cm$^{-1}$), while the diamond-core $Co_2F_2$ di-fluoride bridged dimer **F$^2$** exhibits weaker AFM coupling ($J$ = –2.97 cm$^{-1}$). The observed $g$ values for **F$^2$** are higher than that for **F$^1$**, due to the smaller ligand field splitting and suggesting significant contributions from the larger spin-orbit coupling parameter Z in **F$^1$**, which emanates from the more symmetric $^4T_{1g}$ ground state of the individual cobalt ions in **F$^1$**.

## 3.4 EXPERIMENTAL

### 3.4.1 Reagents and Procedures

Cobalt(II) tetrafluoroborate hexahydrate, cobalt(II) perchlorate hexahydrate, 1,3-diaminopropane, 2-pyridinecarboxaldehyde, 6-(4-chlorophenyl)-2-pyridinecarboxaldehyde and 6-methoxy-2-pyridinecarboxaldehyde were obtained from Sigma-Aldrich. The solvents MeOH, EtOH, MeCN, pyridine and $Et_2O$ were purchased from Fisher Scientific and used without further purification. The deuterated solvent $CDCl_3$ was purchased from Cambridge Isotopes and used as received. All ligand synthesis and metalations were performed under ambient atmosphere.

### 3.4.2 Synthesis of Ligands

#### *3.4.2.1 (1E,1'E)-N,N'-(ethane-1,2-diyl)bis(1-(6-methoxypyridin-2-yl)methanimine) ($enN_4$-OMe)*

A batch of 6-methoxy-2-pyridinecarboxaldehyde (2.91 g, 21.2 mmol) was dissolved in 25 mL of MeOH. Separately, ethylenediamine (603 mg, 10.0 mmol) was dissolved in 5 mL of MeOH and added dropwise to the aldehyde solution with extra 5 mL as a final wash. The solution was refluxed overnight. Upon cooling, the solution spontaneously recrystallized and filtered on Büchner funnel to afford yellow crystals. Yield: 2.92 g (98%). $^1$H NMR in $CDCl_3$ (δ in ppm): 8.30 (s 2H), 7.60 (t 2H), 7.58 (d 2H), 6.75 (d 2H), 4.02 (s 4H), 3.94 (s 6H).

#### *3.4.2.2 (1E,1'E)-N,N'-(ethane-1,2-diyl)bis(1-(6-(4-chlorophenyl)pyridin-2-yl)methanimine) ($enN_4$-PhCl)*

A batch of 6-(4-chlorophenyl)-2-pyridinecarboxaldehyde (1.81 g, 8.32 mmol) was dissolved in 25 mL of MeOH. Separately, ethylenediamine (250 mg, 4.16 mmol) was dissolved in 5 mL of MeOH and added dropwise to the aldehyde solution, which made the whole reaction mixture into a pasty pale-yellow substance. Addition of extra 10-20 mL of

MeOH dissolved most of the substance. The solution was then refluxed overnight at 70 °C yielding a bright yellow solution with visible powder. The progress of the reaction was monitored by taking $^{1}$H NMR spectroscopy. Since the aldehyde resonances were still present, MeOH replaced by EtOH and additional 130 mg of ethylenediamine was added. Refluxing the reaction for additional 7.5 h resulted in a peachy orange solution with solids. Vacuum filtration of the reaction mixture afforded white solid as a product. Yield: 1.36 g (71%). Selected IR bands (ν in $cm^{-1}$): 1020 vs, 804 m. $^{1}$H NMR in $CDCl_3$ (δ in ppm): 8.41 (s 2H), 7.85-7.82 (m 6H), 7.75 (s 2H), 7.63 (d 2H), 7.35 (m 4H), 4.01 (s 4H).

#### *3.4.2.3 (1E,1'E)-N,N'-(propane-1,3-diyl)bis(1-(pyridin-2-yl)methanimine) ($pnN_4$)*

A batch of 2-pyridinecarboxaldehyde (1.645 g, 15.36 mmol) was dissolved in 25 mL of EtOH. Separately, 1,3-diaminopropane (0.513 g, 6.92 mmol) was dissolved in 10 mL of EtOH and added dropwise to the aldehyde solution. The solution was refluxed at 80 °C for 6.5 hours, during which the solution turned red-orange. Upon cooling, the solution was evaporated in vacuo under heating until the liquid turned oily and more viscous. The solution was then evaporated under a stream of $N_2$ gas to remove any remaining solvent. The final product was a dark orange-brown oil. Yield: 1.40 g (80%). Selected IR bands (ν in $cm^{-1}$): 1333 w, 1303 w, 771 s. $^{1}$H NMR in $CDCl_3$ (δ in ppm): 8.52 (d 2H), 8.31 (s 2H), 7.88 (d 2H), 7.61 (t 2H), 7.17 (t 2H), 3.69 (t 4H), 2.06 (q 2H). HRMS (+ESI): *m/z* calcd. for $C_{15}H_{16}N_4$ (M), 252.1375; found, $(M+H)^+$ 253.1437.

#### *3.4.2.4 (1E,1'E)-N,N'-(propane-1,3-diyl)bis(1-(6-(4-chlorophenyl)pyridin-2-yl)methanimine) ($pnN_4$-PhCl)*

A batch of 6-(4-chlorophenyl)-2-pyridinecarboxaldehyde (1.0 g, 4.6 mmol) was dissolved in 30 mL of MeOH. Separately, 1,3-diaminopropane (0.17 g, 2.3 mmol) was dissolved in 10 mL of MeOH and added dropwise to the aldehyde solution. The resulting solution was

refluxed overnight at 65 °C, forming an off-white precipitate. Upon cooling, the precipitate was filtered and collected, affording an ivory powder. Yield: 1.03 g (95%). Selected IR bands (ν in $cm^{-1}$): 1328 w, 1300 w, 802 s. $^1H$ NMR in $CDCl_3$ (δ in ppm): 8.48 (s 2H), 7.95 (m 6H), 7.80 (t 2H), 7.70 (dd 2H), 7.42 (d 4H), 3.81 (t 4H), 2.18 (q 2H). HRMS (+ESI): *m/z* calcd. for $C_{27}H_{22}Cl_2N_4$ (M), 472.1222; found, $(M+H)^+$ 473.1305.

#### *3.4.2.5 (1E,1'E)-N,N'-(propane-1,3-diyl)bis(1-(6-methoxypyridin-2-yl)methanimine) ($pnN_4$-OMe)*

A batch of 6-methoxy-2-pyridinecarboxaldehyde (1.905 g, 13.89 mmol) was dissolved in 25 mL of MeOH. Separately, 1,3-diaminopropane (0.500 g, 6.75 mmol) was dissolved in 10 mL of MeOH and added dropwise to the aldehyde solution. The solution was refluxed at 70 °C overnight. The resulting an orange solution evaporated in vacuo under heating until the liquid turned oily and more viscous. The final product was an orange oil. Yield: 1.75 g (81%). Selected IR bands (ν in $cm^{-1}$): 1465 s, 1264 s, 802 s. $^1H$ NMR in $CDCl_3$ (δ in ppm): 8.25 (s 2H), 7.56 (d 2H), 7.53 (t 2H), 6.70 (d 2H), 3.90 (s 6H), 3.71 (t 4H), 2.09 (q 2H). HRMS (+ESI): *m/z* calcd. for $C_{17}H_{20}N_4O_2$ (M), 312.1586; found, $(M+H)^+$ 313.1671.

### 3.4.3 Synthesis of Metal Complexes

#### *3.4.3.1 $[Co_2(\mu\text{-}F)(pnN_4\text{-}PhCl)_2(OH_2)(MeCN)](BF_4)_3 \bullet (MeCN)_2$ ($F^1$)*

The ligand **$pnN_4$-PhCl** (250 mg, 0.528 mmol) was dissolved in 20 mL of MeCN to generate a slurry. Separately, 180 mg (0.528 mmol) of $[Co(OH_2)_6](BF_4)_2$ was dissolved in 20 mL of MeCN to generate a dark pink solution and added dropwise to the stirred ligand solution. Upon completing the addition of the metal salt, the solution became transparent and bright orange. The color did not change any further as the solution was stirred in air for 1 h and allowed to stand overnight; no precipitate was formed from the initial reaction. Vapor diffusion of $Et_2O$ into the MeCN solution of the complex over one week afforded small

reddish-pink crystals suitable for X-ray diffraction. Yield: 60 mg (28%). Selected IR bands (ν in $cm^{-1}$): 1599 m, 1450 m, 1000 vs, 838 m, 807 s, 751 m. Elemental analysis for $C_{60}H_{55}B_3Cl_4Co_2F_{13}N_{11}O$, calcd.: C 48.52, H 3.73, N 10.37; found: C 48.20, H 3.63, N 10.21. Magnetic susceptibility (benchtop, 298 K): $\mu_{eff}$ = 6.24 $\mu_B$.

#### *3.4.3.2 $[Co_2(\mu\text{-}F)_2(pnN_4\text{-}PhCl)_2](BF_4)_2$ ($F^2$)*

*Method A.* The ligand **pnN$_4$-PhCl** (250 mg, 0.528 mmol) was dissolved in 20 mL of MeCN to generate a slurry, and 5 drops of pyridine were added. Separately, 180 mg (0.528 mmol) of $[Co(OH_2)_6](BF_4)_2$ was dissolved in 20 mL of MeCN to generate a dark pink solution and added dropwise to the stirred ligand solution. Upon completing the addition of the metal salt, the solution became transparent and bright orange. The color did not change any further as the solution was stirred in air for 30 minutes and stored overnight; no precipitate was formed from the initial reaction. Vapor diffusion of $Et_2O$ into an MeCN solution of the complex over two weeks afforded small red crystals formed suitable for X-ray diffraction studies. Yield: 47 mg (26%). Selected IR bands (ν in $cm^{-1}$): 1652 w, 1595 m, 1455 m, 1432 w, 1394 w, 1172 w, 1091 s, 1045 vs, 1034 vs, 1012 s, 1001 s, 974 s, 922 m, 837 s, 802 vs, 756 s, 742 m, 717 w, 650 m, 520 m, 504 m, 472 m. Elemental analysis for $C_{54}H_{44}B_2Cl_4Co_2F_{10}N_8$, calcd.: C 50.82, H 3.48, N 8.78; found: C 50.66, H 3.50, N 8.77. Magnetic susceptibility (benchtop, 298 K): $\mu_{eff}$ = 7.70 $\mu_B$.

*Method B.* Complex **F$^2$** can be produced via different route. The ligand **pnN$_4$-PhCl** (37.6 mg, 0.0794 mmol) was dissolved in 7 mL of MeCN with one drop of pyridine. Separately, **4** (50.0 mg, 0.0794 mmol) was dissolved in 7 mL of MeCN and added dropwise to the stirring ligand solution. Upon completing the addition of the solution of **4**, the solution became orange. The solution was stirred in air for one hour and then overnight covered; no precipitate was formed from the initial reaction. Vapor diffusion of $Et_2O$ into the MeCN

solution of the complex over one month afforded small red-orange crystals suitable for X-ray diffraction, giving the same unit cell values as those from previous synthetic route.

#### *3.4.3.3 [$Co_2(pnN_4)_3$]($BF_4$)$_4$•($MeCN$)$_3$•($H_2O$) (3)*

The ligand **pnN$_4$** (600 mg, 2.378 mmol) was dissolved in 20 mL of MeCN to generate an orange solution. Separately, 540 mg (1.585 mmol) of [$Co(OH_2)_6$]($BF_4$)$_2$ was dissolved in 15 mL of MeCN and added dropwise to the stirring ligand solution. Upon completing the addition of the metal salt, the solution became dark black, with a red tint. The solution was stirred in air for one hour and then overnight covered. A beige precipitate was formed and filtered with a Büchner funnel (307 mg). Vapor diffusion of $Et_2O$ into a MeCN solution of the precipitate over one month afforded small red crystalline needles. Yield: 307 mg (28%). Selected IR bands ($\nu$ in $cm^{-1}$): 1643 w, 1599 m, 1446 w, 1307 w, 1049 vs, 1020 vs, 885 w, 775 m, 520 w, 494 w, 416 w. Elemental analysis for $C_{45}H_{50}B_4Co_2F_{16}N_{12}O$ (**[$Co_2(pnN_4)_3$]($BF_4$)$_4$•($H_2O$)**), calcd.: C 43.59, H 4.06, N 13.55; found: C 42.98, H 4.06, N 14.03. Magnetic susceptibility (benchtop, 298 K): $\mu_{eff}$ = 7.09 $\mu_B$.

#### *3.4.3.4 [$Co(py)_4(MeCN)_2$]($BF_4$)$_2$ (4)*

In 10 mL of MeCN, 100 mg of [$Co(OH_2)_6$]($BF_4$)$_2$ was dissolved and 20 drops of pyridine were added dropwise into the solution. The solution was stirred in air overnight, which remained an orangish-pink color. Vapor diffusion of $Et_2O$ into the MeCN solution of the complex was over 3 d afforded small pink crystals suitable for X-ray diffraction studies. Yield: 96 mg (52%). Selected IR bands ($\nu$ in $cm^{-1}$): 1604 m, 1445 s, 1220 m, 1112 s, 1039 vs, 1009 vs, 980 vs, 951 s, 756 s, 702 vs, 655 w, 629 m, 425 m. Elemental analysis for $C_{20}H_{20}B_2CoF_8N_4$ ([$Co(py)_4$]($BF_4$)$_2$), calcd.: C 43.76, H 3.67, N 10.21; found: C 41.30, H 4.22, N 10.73.

#### *3.4.3.5 [Co(pnN$_3$-OMe)$_2$](ClO$_4$)$_2$ (5(ClO$_4$)$_2$)*

The ligand **pnN$_4$-OMe** (100 mg, 0.320 mmol) was dissolved in 10 mL of MeCN (the presence or absence of 5 drops of pyridine had no effect) to make a yellow solution. Separately, 117 mg (0.320 mmol) of [Co(OH$_2$)$_6$](ClO$_4$)$_2$ was dissolved in 10 mL of MeCN and added dropwise to the stirring ligand solution. Upon completing the addition of the metal salt, the solution became dark red. The color did not change any further as the solution was stirred in air for one hour and stored overnight; no precipitate was formed from the initial reaction. Vapor diffusion of Et$_2$O into an MeCN solution of the complex over one week afforded feathery reddish pink crystals formed suitable for X-ray diffraction studies. Yield: 53 mg (26%). Selected IR bands (ν in cm$^{-1}$): 1597 s, 1574 s, 1480 s, 1433 s, 1310 s, 1288 s, 1069 vs, 1003 s, 970 s, 959 s, 945 s, 916 s, 807 s, 799 s, 760 s, 736 m, 621 vs, 575 m. Elemental analysis for C$_{20}$H$_{30}$Cl$_2$CoN$_6$O$_{10}$, calcd.: C 37.28, H 4.69, N 13.04; found: C 37.27, H 4.52, N 11.84.

#### *3.4.3.6 [Co(pnN$_3$-OMe)$_2$](BF$_4$)$_2$ (5(BF$_4$)$_2$)*

This salt was prepared according to the same procedure as above. Selected IR bands (ν in cm$^{-1}$): 1597 s, 1575 s, 1481, 1434, 1393 m, 1311 s, 1287 s, 1032 vs, 1001 s, 957 s, 944 s, 916 s, 801 s, 760 s, 738 w, 520 m. Elemental analysis for C$_{20}$H$_{30}$B$_2$CoF$_8$N$_6$O$_2$, calcd.: C 38.81, H 4.88, N 13.58; found: C 38.74, H 4.84, N: 13.46.

### 3.4.4 X-ray Crystallography

Definitions used for calculating $R_w(F^2)$, R(F) and the goodness of fit, S, are given below. Tables of crystal data and refinement parameters and tables for bond lengths, angles and torsion angles are summarized in Appendix C.2.

$$R_w(F^2) = \sqrt{\frac{\sum w(|F_0|^2 - |F_C|^2)^2}{\sum w(|F_0|)^4}}$$

$$R(F) = \frac{\sum|F_0| - |F_C|}{\sum|F_0|}$$ for reflections with $F_0 > 4(\sigma(F_0))$

$$S = \frac{\sum w(|F_0|^2 - |F_C|^2)^2}{(n-p)}$$

#### *3.4.4.1 [Co$_2$(μ-F)(pnN$_4$-PhCl)$_2$(OH$_2$)(MeCN)](BF$_4$)$_3$•(MeCN)$_2$ (F$^1$)*

Crystals grew as clusters of parallelipipes by vapor diffusion of $Et_2O$ into the MeCN solution of **F$^1$**. The analyzed crystal was cut from a larger crystal and had approximate dimensions of 0.56 × 0.46 × 0.32 mm. The data were collected on a Rigaku AFC12 diffractometer with a Saturn 724+ CCD using a graphite monochromator with Mo Kα radiation (λ = 0.71073 Å). A total of 1220 frames of data were collected using θ-scans with a scan range of 0.5° and a counting time of 45 seconds per frame. The data were collected at 100 K using a Rigaku XStream low temperature device. Data reduction were performed using the Rigaku Americas Corporation's Crystal Clear version 1.40.[144] The structure was solved by direct methods using SIR2004[176] and refined by full-matrix least-squares on $(F)^2$ with anisotropic displacement parameters for the non-H atoms using SHELXL-2014/7.[152] Structure analysis was aided by use of the programs PLATON98[147] and WinGX.[148] The hydrogen atoms on carbon were calculated in ideal positions with isotropic displacement parameters set to 1.2 × $U_{eq}$ of the attached atom (1.5 × $U_{eq}$ for methyl hydrogen atoms).

For complex **F$^1$**, the cobalt complex resides around a crystallographic two-fold rotation axis at ½, y, ¼. The two-fold rotation axis passes through the bridging fluoride ion, F1. To maintain charge balance in the crystal, there are three $BF_4$ ions per dimeric complex. In the asymmetric unit, one of the tetrafluoroborate ions is given half-weight. This ion is disordered with a half-weighted molecule of acetonitrile. The two-fold symmetry of the complex results in the disorder of a molecule of water and a molecule of acetonitrile that are bound to the Co ion. By symmetry, the water and acetonitrile molecules

are half-weighted in the refinement model. Because this disorder could be the result of imposing two-fold symmetry on the complex, a model in the lower symmetry space group, *C*c, was considered. In *C*c, there is no requirement that the water molecule and the acetonitrile molecule need be disordered. The refinement in *C*c was reasonable. Predictably, the refinement model in *C*c suffered from high correlation between parameters that would be related by the two-fold rotation axis. The agreement factors were also reasonable but significantly higher than those for the *C*2/c model. For the *C*c model, R1 = 0.0543, while wR2 = 0.149 and GOOF = 1.08. When compared to the *C*2/c model, where R1 = 0.0452 and wR2 = 0.112, with a GOOF = 1.07, the *C*2/c model is superior.

The function, $\Sigma w(|F_0|^2 - |F_C|^2)^2$, was minimized, where $w = 1/[(\sigma(F_0))^2 + (0.0403*P)^2 + (19.6854*P)]$ and $P = (|F_0|^2 + 2|F_C|^2)/3$. $R_w(F^2)$ refined to 0.112, with R(F) equal to 0.0452 and a goodness of fit, S, = 1.07. The data were checked for secondary extinction effects but no correction was necessary. Neutral atom scattering factors and values used to calculate the linear absorption coefficient are from the International Tables for X-ray Crystallography (1992).[149]

#### *3.4.4.2 $[Co_2(\mu\text{-}F)_2(pnN_4\text{-}PhCl)_2](BF_4)_2$ ($F^2$)*

Crystals grew as clusters of parallelipipes by vapor diffusion of $Et_2O$ into the MeCN solution of **F²**. The analyzed crystal was cut from a larger crystal and had approximate dimensions of 0.15 × 0.08 × 0.07 mm. The data were collected on a Rigaku AFC12 diffractometer with a Saturn 724+ CCD using a graphite monochromator with Mo Kα radiation (λ = 0.71073 Å). The data were collected at 100 K using a Rigaku XStream low temperature device. Data reduction were performed using the Rigaku Americas Corporation's Crystal Clear version 1.40.[144] The structure was solved by direct methods using SIR2004[176] and refined by full-matrix least-squares on $F^2$ with anisotropic

displacement parameters for the non-H atoms using SHELXL-2014/7.[152] Structure analysis was aided by use of the programs PLATON98[147] and WinGX.[148] The hydrogen atoms on carbon were calculated in ideal positions with isotropic displacement parameters set to 1.2 × $U_{eq}$ of the attached atom (1.5 × $U_{eq}$ for methyl hydrogen atoms).

The function, $\Sigma w(|F_0|^2 - |F_C|^2)^2$, was minimized, where $w = 1/[(\sigma(F_0))^2 + (0.0336*P)^2 + (5.5519*P)]$ and $P = (|F_0|^2 + 2|F_C|^2)/3$. $R_w(F^2)$ refined to 0.121, with R(F) equal to 0.064 and a goodness of fit, S, = 1.10. The data were checked for secondary extinction effects but no correction was necessary. Neutral atom scattering factors and values used to calculate the linear absorption coefficient are from the International Tables for X-ray Crystallography (1992).[149]

#### *3.4.4.3 $[Co_2(pnN_4)_3](BF_4)_4 \bullet (MeCN)_3 \bullet (H_2O)$ (3)*

Crystals grew as red needles by vapor diffusion of $Et_2O$ into the MeCN solution of **3**. The analyzed crystal was cut from a larger crystal and had approximate dimensions of 0.19 × 0.16 × 0.14 mm. The data were collected on a Rigaku AFC12 diffractometer with a Saturn 724+ CCD using a graphite monochromator with Mo Kα radiation (λ = 0.71073 Å). The data were collected at 100 K using a Rigaku XStream low temperature device. Data reduction were performed using the Rigaku Americas Corporation's Crystal Clear version 1.40.[144] The structure was solved by direct methods using SIR2004[176] and refined by full-matrix least-squares on $F^2$ with anisotropic displacement parameters for the non-H atoms using SHELXL-2014/7.[152] Structure analysis was aided by use of the programs PLATON98[147] and WinGX.[148] The hydrogen atoms on carbon were calculated in ideal positions with isotropic displacement parameters set to 1.2 × $U_{eq}$ of the attached atom (1.5 × $U_{eq}$ for methyl hydrogen atoms).

The function, $\Sigma w(|F_0|^2 - |F_C|^2)^2$, was minimized, where $w = 1/[(\sigma(F_0))^2 + (0.0340*P)^2 + (7.4434*P)]$ and $P = (|F_0|^2 + 2|F_C|^2)/3$. $R_w(F^2)$ refined to 0.120, with R(F) equal to 0.055 and a goodness of fit, S, = 1.05. The data were checked for secondary extinction effects but no correction was necessary. Neutral atom scattering factors and values used to calculate the linear absorption coefficient are from the International Tables for X-ray Crystallography (1992).[149]

#### *3.4.4.4 $[Co(py)_4(MeCN)_2](BF_4)_2$ (4)*

Crystals grew as hexagons by vapor diffusion of $Et_2O$ into the MeCN solution of **4**. The analyzed crystal was cut from a larger crystal and had approximate dimensions of 0.43 × 0.39 × 0.35 mm. The data were collected on a Rigaku AFC12 diffractometer with a Saturn 724+ CCD using a graphite monochromator with Mo Kα radiation (λ = 0.71073 Å). The data were collected at 100 K using a Rigaku XStream low temperature device. Data reduction were performed using the Rigaku Americas Corporation's Crystal Clear version 1.40.[144] The structure was solved by direct methods using SIR2004[176] and refined by full-matrix least-squares on $F^2$ with anisotropic displacement parameters for the non-H atoms using SHELXL-2014/7.[152] Structure analysis was aided by use of the programs PLATON98[147] and WinGX.[148] The hydrogen atoms on carbon were calculated in ideal positions with isotropic displacement parameters set to 1.2 × $U_{eq}$ of the attached atom (1.5 × $U_{eq}$ for methyl hydrogen atoms).

The function, $\Sigma w(|F_0|^2 - |F_C|^2)^2$, was minimized, where $w = 1/[(\sigma(F_0))^2 + (0.1971*P)^2 + (31.3920*P)]$ and $P = (|F_0|^2 + 2|F_C|^2)/3$. $R_w(F^2)$ refined to 0.396, with R(F) equal to 0.125 and a goodness of fit, S, = 1.19. The data were checked for secondary extinction effects but no correction was necessary. Neutral atom scattering factors and values used to

calculate the linear absorption coefficient are from the International Tables for X-ray Crystallography (1992).[149]

#### *3.4.4.5 [Co(pnN$_3$-OMe)$_2$](ClO$_4$)$_2$ (5(ClO$_4$)$_2$)*

Crystals grew as needles by vapor diffusion of $Et_2O$ into the MeCN solution of **5**. The analyzed crystal was cut from a larger crystal and had approximate dimensions; 0.54 × 0.19 × 0.16 mm. The data were collected on a Rigaku AFC12 diffractometer with a Saturn 724+ CCD using a graphite monochromator with Mo Kα radiation (λ = 0.71073 Å). The data were collected at 100 K using a Rigaku XStream low temperature device. Data reduction were performed using the Rigaku Americas Corporation's Crystal Clear version 1.40.[144] The structure was solved by direct methods using SIR2004[176] and refined by full-matrix least-squares on $F^2$ with anisotropic displacement parameters for the non-H atoms using SHELXL-2014/7.[152] Structure analysis was aided by use of the programs PLATON98[147] and WinGX.[148] The hydrogen atoms on carbon were calculated in ideal positions with isotropic displacement parameters set to 1.2 × $U_{eq}$ of the attached atom (1.5 × $U_{eq}$ for methyl hydrogen atoms).

The function, $\Sigma w(|F_0|^2 - |F_C|^2)^2$, was minimized, where $w = 1/[(\sigma(F_0))^2 + (0.1475*P)^2 + (30.3352*P)]$ and $P = (|F_0|^2 + 2|F_C|^2)/3$. $R_w(F^2)$ refined to 0.086, with R(F) equal to 0.036 and a goodness of fit, S, = 1.01. The data were checked for secondary extinction effects but no correction was necessary. Neutral atom scattering factors and values used to calculate the linear absorption coefficient are from the International Tables for X-ray Crystallography (1992).[149]

### 3.4.5 SQUID

Magnetic susceptibility measurements were carried out in a Quantum Design superconducting quantum interference device (SQUID) magnetometer after cooling in zero

field (ZFC) and after cooling in a measuring field (FC) of 100 Oe or 1 kOe. Room temperature magnetic susceptibility measurements were performed by Alfa Aesar magnetic susceptibility balance.

### 3.4.6 Physical Measurements

$^{1}$H NMR spectra were collected on Varian DirecDrive 400 MHz spectrometer and chemical shifts were referenced to $CDCl_3$. Infrared spectra were recorded using a Bruker Alpha spectrometer equipped with a diamond ATR crystal. Elemental analysis was performed by Midwest Micro Lab. High-resolution mass spectrometry data was measured on an Agilent Technologies 6530 Accurate Mass QTofLC/MS instrument.

# Chapter 4: Different Binding Modes of Pincer Ligands in $H_2$ Activating Iron-Acyl Model Complexes for Mono-Iron Hydrogenase (Hmd)

## 4.1 Introduction

### 4.1.1 [Fe] Hydrogenase

In nature, dihydrogen activation has been accomplished by a class of enzymes called hydrogenases.[51] Among the three types, mono [Fe] hydrogenase catalyzes the reversible cleavage of $H_2$ in a *non-redox*, heterolytic fashion as a key step during the methanogenic conversion of carbon dioxide ($CO_2$) to methane ($CH_4$).[57] In this process, the substrate methenyltetrahydromethanopterin (methenyl-$H_4MPT^+$) is used as a $C_1$ 'carrier' throughout the metabolic pathway. As a result of $H_2$ activation by Hmd, a hydride is transferred to the $H_4MPT^+$ substrate, thus producing methylenetetrahydromethanopterin (methylene-$H_4$MPT) and a proton.[2]

Based primarily on the 2008 and 2009 crystal structures of the enzyme, the active site is composed of the following moieties (Scheme 4.1): a redox-inactive Fe(II) center, a bidentate acyl-pyridine moiety presenting a N (pyridone/pyridinol) and C (acyl) donor from derived from the so-called FeGP cofactor; a S donor from Cys176; *cis* carbonyl ligands; and lastly a labile/open coordination site (*trans* to acyl-C) for solvent or substrate binding.[57,58,177,178] As a structure dictates its function, close examination of particular coordination motifs through a biomimetic approach can aid in clarifying the role of each ligand and its orientation, thus providing deeper insight for understanding the catalytic mechanism.

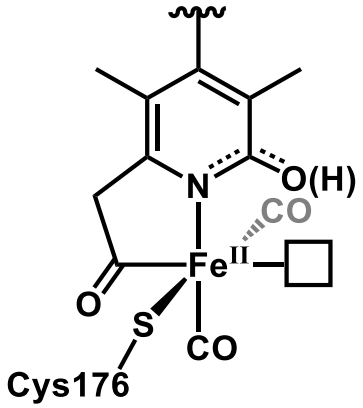


Scheme 4.1: Active site of the [Fe] hydrogenase.

One of the most intriguing features of [Fe] hydrogenase is the presence of the iron-acyl moiety. Indeed, this donor motif is thus far unique in biological systems. Electronically, the acyl-C donor cannot be replicated by any of the standard amino acid residues, nor by any of the ligands found in other hydrogenase enzymes (CO, $CN^-$, thiolate, azadithiolate, etc.). While it is an extremely strong σ-donor ($pK_a \approx 35$) – stronger than almost any other known biological ligand other than methyl ($pK_a \approx 45$; e.g. methylcobalimin) – it is also a good π-acceptor due to the available resonance form of the oxyanion/Fisher carbene ($Fe{=}C{-}O^-$). It is thus presumed to play a very specific role in the non-redox activation of $H_2$ and hydride transfer mechanism.

### 4.1.2 Metal-Ligand Cooperation of Pincer Systems

Regarding the geometry of the donors about the metal center, it can be reasonably postulated that in the absence of steric (or otherwise geometrically directing) effects, the strong σ-donating ability of the acyl-C directs the open/solvent binding site to its *trans* position. Indeed, this postulate is epitomized in the model chemistry developed by Hu, Pickett and others – wherein non-macrocyclic CNS donor sets (i.e. the thiolate is not tethered to the acylpyridine or carbamoyl-pyridine moiety) inherently adopt a *fac*-CNS

donor geometry with the halide, solvent[179] or open[180–182] site oriented *trans* from the acyl-C donor. However, reactivity studies with such 'non-tethered' model complexes have not been forthcoming, likely due to the instability of hydride intermediates or possibly lack of $H_2$ activation due to fluxional geometries. This strong *trans* influence of the acyl group (much stronger than carbonyl)[88] is thought to play a major role in the catalysis in terms of electronic effects. In this respect, it is remarkable that nature chose to make use of a rare type of ligand to promote catalysis.

Metal-ligand cooperativity in small molecule systems, and even more broadly in active site chemistry,[183] has been recently noted. A number of related iron(II) carbonyl complexes have been investigated by organometallic and catalysis researchers in the last decade to better understand the role of each donor moiety (Scheme 4.2). Milstein and coworkers adopted the use of pincer-type $P^CN^CN$ and $P^CN^CP$-type ligands, in which the central pyridine presents two phosphine moieties at the *ortho* positions via methylene linkers.[12] A variety of Fe(II)-(PNN/PNP)-hydride complexes were shown to serve as hydrogenation catalysts for ketones, aldehydes and esters to alcohols; $CO_2$ to formate; alkynes to alkenes; and amines to amide and alcohols.[76,77,79,81] Mechanistically, these species universally proceed through a dearomatized pyridinate species, wherein one of the picolinic protons in the methylene linker is deprotonated. Subsequently, the metal-ligand cooperativity of the Lewis acidic (metal) and basic (ligand) sites drive the heterolytic activation of $H_2$. In related work, Kirchner and co-workers focused on iron(II) complexes with $P^NN^NP$-type ligands where the pyridine ring and the phosphine moieties are connected by amide (NH) linkers instead.[83–85] Upon activation with strong base (NH deprotonation), the complexes catalyze the hydrogenation of ketones and aldehydes, and proceed through the same heterolytic cleavage of $H_2$ as supported by DFT calculations.[83,84] A number of ruthenium complexes with either symmetric PNP- or asymmetric PNN-based pincer

ligands were also studied for their various catalytic activities by Huang and coworkers.[184–187] In this case, asymmetric PNN type ligands were employed, in which the resulting Ru-pincer complexes were similarly 'dearomatized' via base treatment. Such Ru-pincer complexes performed: dehydrogenative homocoupling of primary alcohols to esters and dehydrogenative couplings of amines to imines;[184] transfer hydrogenation of ketones;[185] and electrocatalytic reduction of $CO_2$ to CO and HCOOH in $H_2O$/MeCN mixture.[187]

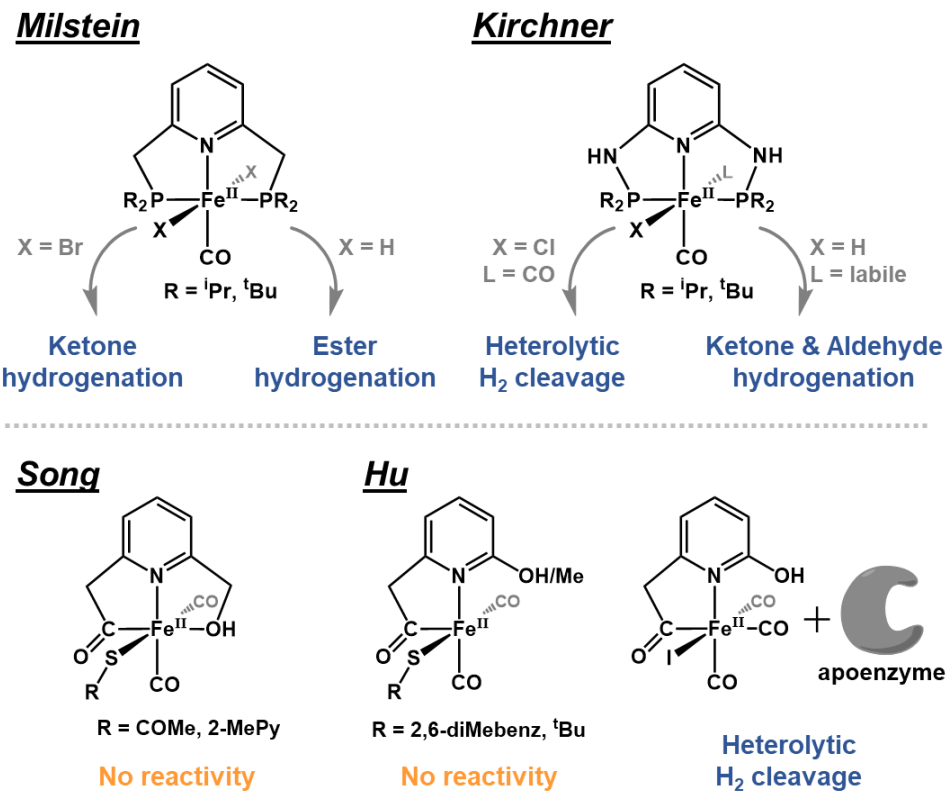


Scheme 4.2: Examples of known PNP pincer systems (top row) and synthetic models of [Fe] hydrogenase (bottom row).

### 4.1.3 Synthetic Models of Hmd

Among bio-inorganic researchers, the Song group utilized 2-acylmethyl-6-pyridinol (or hydroxymethyl) ligands to chelate iron(II) and provide more structural resemblance to the [Fe] hydrogenase enzyme active site.[86,87,188] Although lacking reactivity studies, they successfully implemented all the donor atoms in correct geometry and donor orientation as found in the active site. The Hu group has also investigated small-molecule mimics featuring acylmethylpyridine ligands exhibiting a 2-hydroxy[182], 2-methoxy[180,189] or 2-tertbutyl group[182]; a thiolate ligand (2,6-dimethylbenzenethiolate[180,182] and others;[182] and the *cis*-carbonyl motif. And although there was neither crystallographic evidence or reactivity towards $H_2$ of the isolated complex, the first acylmethyl-pyridinol ligand bound iron(II) complex was synthesized.[182] Through pioneering studies using a hybrid protein|molecule approach, it was hypothesized that the following components are crucial in the $H_2$ activation: *i)* the presence of protein environment and substrate (methenyl-$H_4MPT^+$), *ii)* thiolate ligand as an internal base (in other words, a proton acceptor) and *iii)* the pyridine-2-OH moiety (or conjugate pyridone), which positions the active site/cofactor suitable for the heterolytic cleavage of $H_2$. Support for these claims was provided by the preparation and characterization of a 'semi-synthetic [Fe] hydrogenase', which was reconstituted by binding the synthetic models into the apoenzyme. The resulting hybrid enzyme exhibited measurable reactivity (TOF = 2 and 1 $s^{-1}$ for the heterolytic cleavage of $H_2$ in the presence of the substrate and the production of $H_2$, respectively),[183] which corresponded to about 1% of the wildtype enzyme activity. This exceeded the rates of the previously reported synthetic hydrogenation catalysts (TOF ≈ $10^{-3}$ to $10^{-1}$ $s^{-1}$).[190,191]

Figure 4.1 shows the works by our group demonstrating that preservation of the facial coordination motif of the C, N, S donors via an 'anthracene scaffold' approach, a synthetic model can, in fact, promote $H_2$ activation in the absence of the protein

environment.[101] The active solvato-Fe(II) species not only activates $H_2$, but also abstracts hydride from a model imidazolidine substrate (hydride source via C–H activation), then produces $H_2$ with the aid of a bulky phenol (proton source). Furthermore, we recently demonstrated that functional $H_2$ activation and hydride transfer can be performed by thioether- and thiolate-containing model complexes derived from this anthracene scaffold.[102,192]

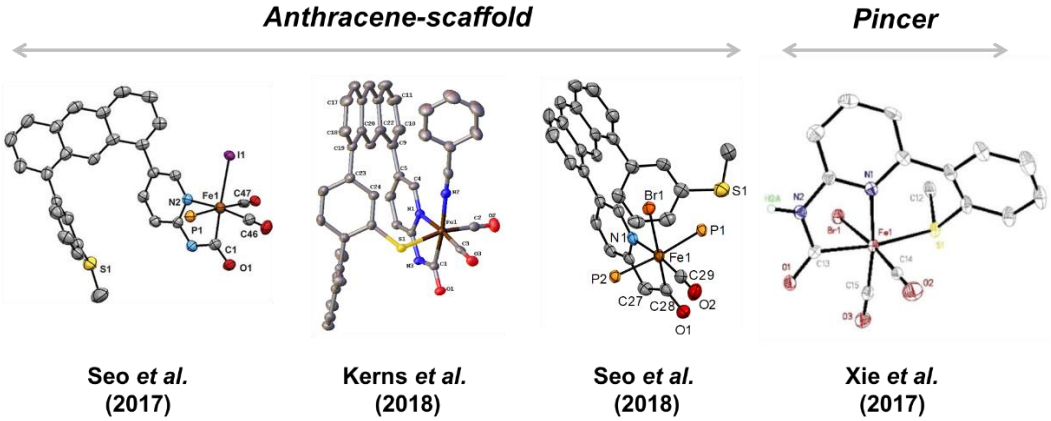


Figure 4.1: Previously studied anthracene-based and pincer iron complexes from our research group.[101,102,192,193]

More closely related to the present work, we reported the carbamoyl-pincer model complex $[(C^{NH}NS)Fe(CO)_2(Br)]$[193,194] (Figure 4.1 and Scheme 4.3) – the carbamoyl version of the methylene-acyl **Fe-CNS** complex in this paper. The CNS donor set was ligated in standard pincer (meridional) fashion, and treatment with a hydride source ($NaHBEt_3$) provided spectroscopic evidence for the Fe–H species (low temp $^1$H NMR spectroscopy: –5.08 ppm in $d^8$-THF). *However, the complex was not competent for $H_2$ activation*, and ligand decomposition was observed upon treatment with strong base (NH deprotonation). We were thus interested to determine the importance of the donor identity (acyl versus carbamoyl) in an analogous complex for $H_2$ activation.

The focus for this project was on the structural and reactivity effects of the methylene-acyl donor in concert with thioether versus phosphine donors in a single-chelate approach. The apparent flexibility of this ligand frame allows the metal center to 'choose' the ideal binding mode based on structural and electronic effects. The structures and enzyme-like reactivities of the resulting **Fe-CNS** and **Fe-CNP** congeners were thus compared herein in the following way: 'forward' direction, using $D_2$ activation (presence or absence of base).

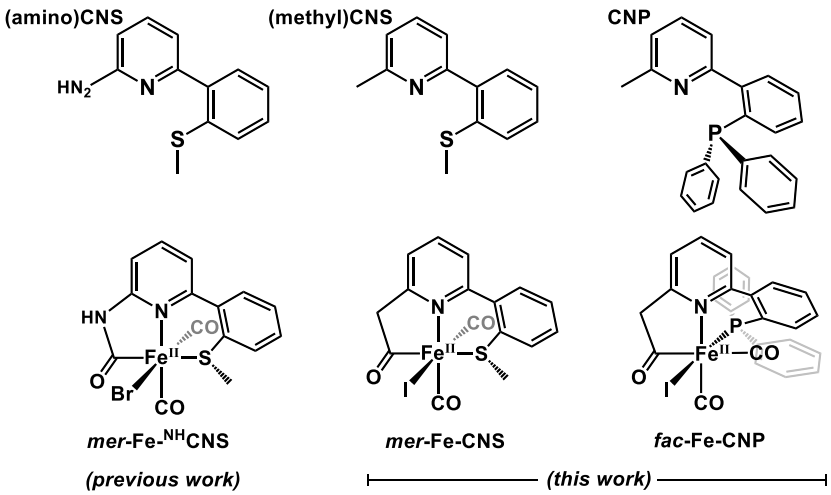


Scheme 4.3: Structures of the apo-ligands (**CNS** and **CNP**), our previous Fe-carbamoyl complex[193,194] and the Fe-acyl complexes (**Fe-CNS** and **Fe-CNP**) used in this work.

## 4.2 Result and Discussion

### 4.2.1 Syntheses

Both ligands, **CNS** and **CNP**, were synthesized from the same starting material, 2-bromo-6-methylpyridine. **CNS** was directly isolated following Suzuki coupling with 2-(methylthio)phenyl boronic acid in moderate yield (67%). For synthesizing **CNP**, 2-(2-bromophenyl)-6-methylpyridine was first synthesized via Suzuki coupling, followed by the diphenylphosphine insertion. For the insertion, rigorous air-free techniques were required to securely introduce the -$PPh_2$ moiety into the ligand. Full experimental procedures are described in Section 4.4.2.3.

Metalations to prepare the **Fe-CNS** and **Fe-CNP** complexes were performed in analogous fashion (Scheme 4.4). As reported previously, syntheses an acylmethylpyridyl-Fe(II) complexes typically proceed through harsh deprotonation of the methylpyridine moiety, followed by metalation with Fe(0) or Fe(II) carbonyls. The choice of an iron source—$Fe(CO)_5$ vs. $Na_2Fe(CO)_4$—depends on how the ligand is activated. When starting with methylpyridine-based ligands, it is activated by *n*BuLi at –10 °C first to form the lithiated species, then reacted with $Fe(CO)_5$ at low temperature (–78 to –25 °C) to generate a Fe(0) intermediate. This intermediate undergoes a migratory insertion at one carbonyl to generate the methylene-acyl-iron unit; finally, it is oxidized with $X_2$ (X = I or Br) to afford the desired Fe(II)-acyl complex.[86,88] The air-sensitive crude product was collected as a yellow-brown powder, and purification via alumina chromatography (performed in the $N_2$ glovebox) provided analytically pure and crystallographically defined samples.

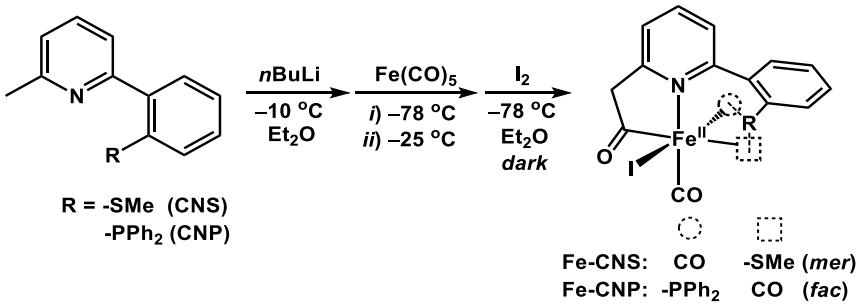


Scheme 4.4: Metalation of **CNS** and **CNP** ligand into the acylmethylpyridyl-Fe(II) complexes, **Fe-CNS** and **Fe-CNP**, respectively.

### 4.2.2 X-ray Structures

#### *4.2.2.1 CNP ligand*

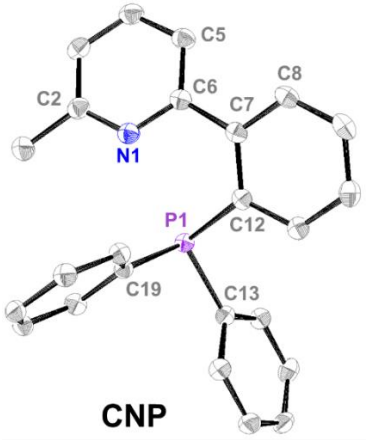


Figure 4.2: ORTEP diagram (50% thermal ellipsoids) of **CNP**. Hydrogen atoms are omitted for clarity. Color scheme: carbon (grey); nitrogen (blue); phosphorous (purple).

The X-ray structure of CNP (Figure 4.2) exhibits the C5-C6-C7-C8 torsion angle of 26.00(19)°. The three C–P bond distances are 1.8504(14), 1.8526(14) and 1.8301(13) Å for C12, C14 and C19, respectively. Three phenyl rings of the triphenylphosphine moiety have a pseudo-$C_3$ axis around P1, where all three rings are angled like a propeller in the same direction.

#### *4.2.2.2 Structural Comparisons of Metal Complexes*

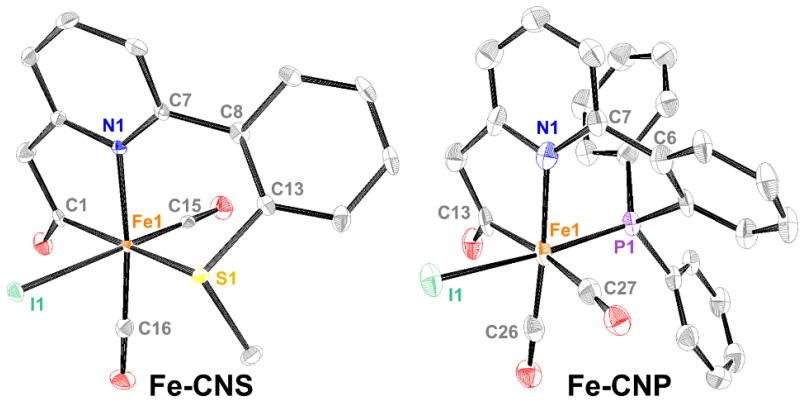


Figure 4.3: ORTEP diagram (50% thermal ellipsoids) of **Fe-CNS** (left) and **Fe-CNP** (right) exhibiting the *mer*-CNS or *fac*-CNP donor orientations, respectively. Hydrogen atoms are omitted for clarity. Color scheme: carbon (grey); nitrogen (blue); oxygen (red); sulfur (yellow); iron (orange); iodine (green); phosphorous (purple).

The crystal structures of the Fe-acyl thioether (**Fe-CNS**) and phosphine (**Fe-CNP**) complexes are depicted in Figure 4.3. In each case, the Fe(II) center is coordinated with one iodide, two carbonyls and one ligand (C, N and L donors). Notably, the ligation mode of the 'pincer' ligand is different in each complex – **Fe-CNS** exhibiting meridional binding, whereas **Fe-CNP** exhibits a facial coordination motif. In each case, one CO ligand occupies the position *trans* to the pyridine N, similar to the Hmd active site. However, the second carbonyl in each case is differentially located: *trans* to the iodide in **Fe-CNS**, and *trans* to the acyl-C donor in **Fe-CNP**. Each of the Fe–C(≡O) bond distances is approximately 1.77 Å, with the notable exception for the CO *trans* to the acyl moiety in Fe-CNP, which is nearly 0.1 Å longer (1.876(11) Å, Table 4.1). This is indicative of the strong σ-donor strength of the acyl-carbanion donor. The Fe–$C_{acyl}$ bond distances for **Fe-CNS** and **Fe-CNP** are not drastically different (1.945(3) and 1.974(10) Å, respectively). Regarding **Fe-CNP**, a literature search reveals that the average distance a Fe–$C_{acyl}$ bond with a *trans* CO is

roughly 1.976 Å,[87,180,188,195,196] which is consistent with the value of **Fe-CNP** (1.974(10) Å). The Fe–I distances for both complexes are nearly identical: 2.6958(5) and 2.6980(17) Å for **Fe-CNS** and **Fe-CNP**, respectively.

| **Selected bond lengths (Å)** | | | **Selected bond angles (◦)** | | |
|---|---|---|---|---|---|
| | **Fe-CNS** | **Fe-CNP** | | **Fe-CNS** | **Fe-CNP** |
| Fe–$N_{py}$ | 2.031(4) | 2.038(8) | $N_{py}$–Fe–$C_{acyl}$ | 85.19(17) | 82.9(4) |
| Fe–$C_{acyl}$ | 1.945(5) | 1.974(10) | $N_{py}$–Fe–S/P | ***S*** 87.80(11) | ***P*** 79.1(2) |
| Fe–S/P | ***S*** 2.3396(14) | ***P*** 2.202(3) | $N_{py}$–$C_{py}$–$C_{Ph}$–$C_{Ph'}$ | –41.2(7) | 38.9(13) |
| Fe–CO | ***trans-iodide*** 1.772(5) | ***trans-acyl*** 1.876(11) | **Ligand binding** | Meridional (pincer-type) | Facial |
| Fe–$CO_{trans-py}$ | 1.768(5) | 1.774(11) | ***trans* to acyl?** | S-Me | CO |
| Fe–I | 2.6958(7) | 2.6980(17) | ***trans* to $N^{py}$?** | CO | CO |

Table 4.1: Selected bond lengths and bond angle comparison between **Fe-CNS** and **Fe-CNP**.

In **CNS**, the $N_{py}$–Fe–$C_{acyl}$ ferracycle angle is 85.19(12)° (Table 4.1). The aryl unit coupled at the *ortho* position on the pyridine ring is twisted out of plane by –41.2(7)°, primarily due to the steric hindrance between the hydrogen atoms on the pyridine and aryl rings *ortho* to the coupling site. This 'flipped up' aryl group directs the thioether S to ligate to the Fe center *trans* to the acyl moiety, thus affording the *mer* coordination motif. In contrast, the *ortho* aryl unit of the **CNP** ligand rotates in the opposite direction, characterized by a +38.9(13)° torsion angle. This allows the bulkier -$PPh_2$ moiety (versus -SMe) to occupy the site *trans* to iodide, rather than *cis* to iodide as in **Fe-CNS**.

Based on these reasonings, an ideal ligand would exhibit a thiolate/thiol (instead of the thioether) with additional substituent(s) to provide a steric hindrance, which will induce a facial ligation.

#### *4.2.2.3 Parameters Leading to Mer versus Fac Coordination Motifs*

The unexpected and spontaneous facial ligation of **CNP** can be explained by closely examining and comparing both steric *and* electronic effects on the Fe-acyl complexes. In both complexes, the coordination of the acyl C, pyridine N, iodide and $CO^{trans\text{-}py}$ remains unchanged. Only two sites, those *trans* to iodide and *trans* to acyl (represented as dotted circle and dotted square in Scheme 4.4, respectively) are occupied by different donors – namely, the second CO and either $S^{Me}$ or $P^{Ph2}$. Also, space-filling models of both complexes (Figure 4.4, top row) reveal that, in fact, the iodide is the bulkiest donor atom (radius: 206 pm) among the six; iodide is also larger than the combined CO ligand. Therefore, iodide will preferentially occupy the least crowded coordination site (Complete space-filling models: Figure 4.4, bottom row). For **Fe-CNS**, the second bulkiest donor is the SMe unit, while in **Fe-CNP** it is $PPh_2$ moiety. Comparing -SMe and -$PPh_2$, the former has only one 'short' arm (methyl), which can easily be deflected away from the bulky iodide without changing the coordination site of the -SMe donor. On the other hand, -$PPh_2$ has two bulky substituents. Therefore, the bulky phosphine moiety cannot occupy the position *cis* to the bulkiest donor atom, iodide. Incidentally, the 'flexibility' of the *ortho*-aryl linkage facilitates binding of the -$PPh_2$ unit *trans* to the iodide, while retaining unperturbed Fe–P bond metrics (2.202(3) Å); the facial CNP ligation is the final result.

Deeper inspection of the donor strengths of -SMe versus -$PPh_2$ also provides insight into the geometric properties of the complexes. Among the **CNS** and **CNP** donor sets, the σ-donor strength is ordered as follows: acyl-C > -$PPh_2$ > $N_{py}$ > -SMe. Thus, the position *trans* from the acyl-C would be the most labile site due to its strong *trans* influence, thus dissuading the coordination of another strong σ-donor (such as -$PPh_2$). Therefore, the phosphine group rotates about the *ortho*-phenyl ring, locating the -$PPh_2$ moiety *cis* to the acyl site. However, in case of **CNS**, the -SMe unit is a weak σ-donor, not unlike the weakly

bound $H_2O$ molecule trans from acyl in the active site. Indeed, all of the previously reported iron-acyl-phosphine complexes[195–198] exhibit non-chelating phosphine ligand(s) at *cis* site(s). Similarly, all examples of iron-*carbamoyl* complexes that contain non-chelating phosphine ligands exhibit *cis*-phosphine(s), except for one case of a *trans* $PMe_3$ unit.[194,199] All of these data are consistent with the strong σ-donor effect of the acyl group, thus affording the *cis*-$PPh_2$ binding motif (and consequently, *fac*-CNP).

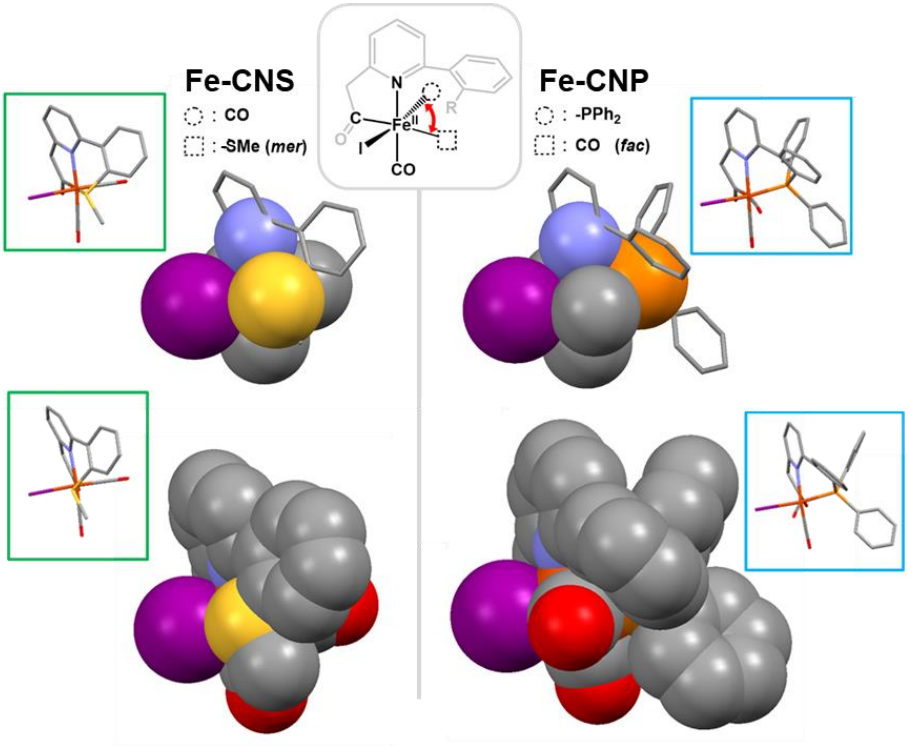


Figure 4.4: *Top row:* Structures of **Fe-CNS** and **Fe-CNP**, respectively, showing only the six donor atoms in space-filling model. *Bottom row:* Complete Space-filling models of **Fe-CNS** and **Fe-CNP**, respectively. Note that in each case, the bulkiest groups are located away from the site of iodide ligation. Each inset represents the capped-sticks model of the larger structure at the same angle. Color scheme: carbon (grey); nitrogen (blue); iodine (dark magenta); sulfur (yellow); phosphorous (orange). Hydrogen atoms are omitted for clarity.

### 4.2.3 Reactivity Studies

#### *4.2.3.1 Deprotonation*

In related non-biomimetic work on iron(II) pincers, it has been established that heterolytic cleavage of $H_2$ occurs via metal-ligand cooperation that utilizes the conjugate base of acidic methylene or amide linkers in the ligand framework.[82] These conjugate bases are 'dearomatized' due to the presence of a pyridonate anion (rather than pyridine) in the central position. In our biomimetic system, we found that the methylene linker protons serve an analogous role (Scheme 4.5).

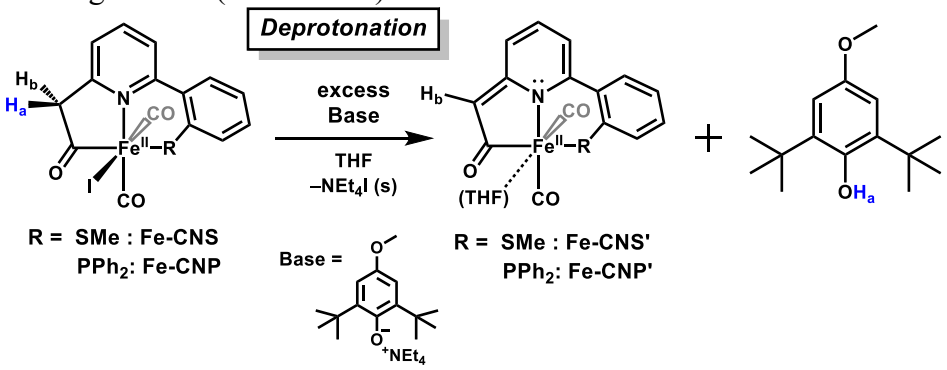


Scheme 4.5: Deprotonation of **Fe-CNS** or **Fe-CNP** with a bulky phenolate base. The hollow wedged bond shown in grey for one carbonyl group represent the position either trans from iodide (**Fe-CNS**) or trans from acyl (**Fe-CNP**).

Up to four equivalents of base was required for a complete conversion of **Fe-CNS** to **Fe-CNS'**. The progress was monitored by infrared spectroscopy, showing a clear transition of the carbonyl stretches (2015, 1957→1983, 1921 $cm^{-1}$) as well as the acyl stretch (1662→1587 $cm^{-1}$) (Figure 4.5, left). Under similar conditions, deprotonation of a methylene proton of **Fe-CNP** yielded the dearomatized species **Fe-CNP'**, exhibiting red shift of the carbonyls (2014, 1960→1987, 1936 $cm^{-1}$) and the acyl (1635→1586 $cm^{-1}$) stretches in infrared spectrum (Figure 4.5, right).

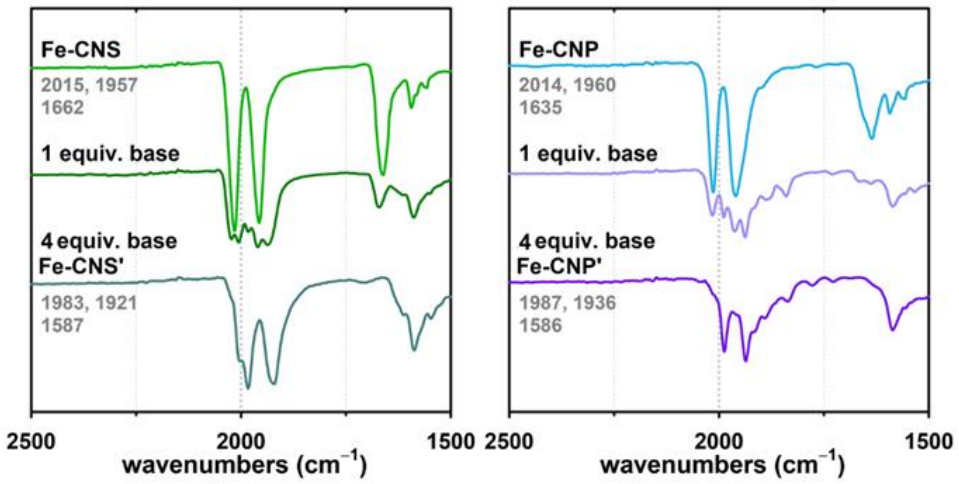


Figure 4.5: Infrared spectra of **Fe-CNS** (left) and **Fe-CNP** (right) deprotonation via bulky phenolate. Note that more than one equivalent of base is required for a complete deprotonation to **Fe-CNS'** or **Fe-CNP'**.

The methylene protons in these iron-acyl complexes are diastereotopic—their chemical environment is quite different, resulting two doublets in $^1$H NMR ($d_8$-THF) at 5.39 and 4.24 ppm ($H_a$ and $H_b$ respectively for **Fe-CNS**, in Figure 4.6A; for **Fe-CNP**, see Figure 4.8). Comparing the structures of the two complexes, the chemical environments of the 'front-side' protons adjacent to the iodide remain relatively similar, compared with distinct chemical environments of the 'back-side' protons (adjacent to CO versus -$PPh_2$ in **Fe-CNS** versus **Fe-CNP**). The nearly identical chemical shifts of 5.46 (**Fe-CNS**) and 5.44 (**Fe-CNP**) support the assignment of the downfield diastereotopic resonance to be $H_a$ in both cases. The more deshielded nature of $H_a$ indicates more susceptibility to deprotonation, and thus $H_a$ is likely the acidic proton in the reactivity studies detailed below.

Reactivity studies required the use of $d_8$-THF (versus $C_6D_6$) as a coordinating solvent and for improved solubility of reagents. Treatment of **Fe-CNS** ($^1$H NMR spectrum, Figure 4.6A) with a bulky phenolate base ($NEt_4^+$ salt of 2,6-di-tert-butyl-4-

methoxyphenolate) results in the disappearance of the diastereotopic resonances, indicating the formation of the dearomatized species **Fe-CNS'** (Figure 4.6B). As a result, the conjugate acid phenol is observed (δ O*H*: 5.70 ppm), and $NEt_4I$(s) is formed as precipitate. It is noted that an excess of phenolate (see assigned resonances in Figure 4.6B) remains observable due to the requirement for ~4 equiv to drive complete deprotonation (see IR section above, Figure 4.5, *left*). Similarly, as noted in the IR spectra (Figure 4.5, right), **Fe-CNP** also required ~4 equiv of base to complete deprotonation.

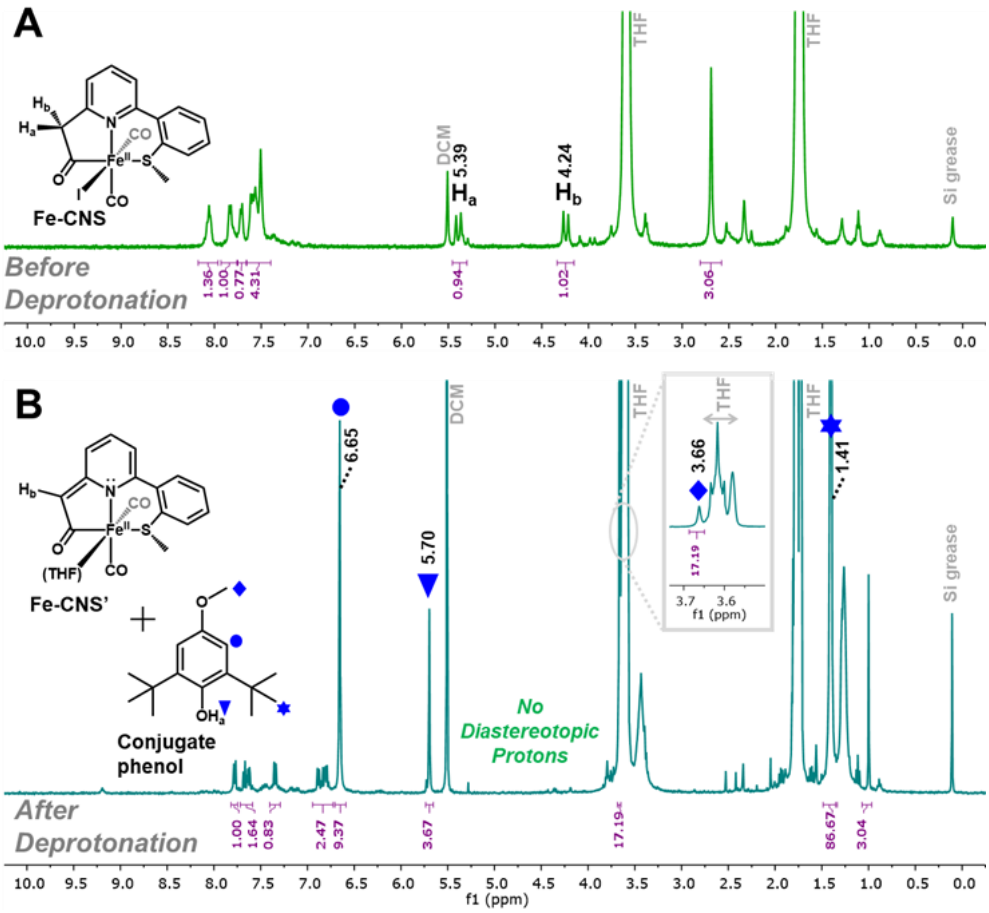


Figure 4.6: A: $^1$H NMR spectrum of **Fe-CNS** in $d_8$-THF. B: $^1$H NMR spectrum of deprotonated species **Fe-CNS'** and conjugate phenol + phenolate in $d_8$-THF. Non-integrated peaks are solvent peaks.

#### *4.2.3.2 $D_2$ Activation*

The deprotonated species **Fe-CNS'** was then placed under 5 atm of $D_2$ and the reaction monitored by $^2H$ NMR spectroscopy (Figure 4.7A). A new resonance at 5.39 ppm was observed within 30 min, which was assigned as the conjugate phenol-O*D* resonance; no Fe–*D* resonance ($D^-$) was observed (e.g., 0 to –30 ppm). Nonetheless, the observation of the $D^+$ resonance indicates activation of $D_2$ via heterolysis by the Fe-CNS system. Recent results from our group demonstrated that a bulky Lewis acid substrate (putative hydride acceptor) could be employed to stabilize and detect iron-hydride species in $^2H$ NMR experiments,[101] or serve as a hydride-accepting substrate.[102] Therefore, the same reaction was performed in the presence of the model substrate $^{Tol}Im[BAr^F]$, a bulky imidazolium salt that mimics the role of methenyl-$H_4MPT^+$ in the enzyme $H_2$ activation process. However, a nearly identical $^2H$ NMR spectrum was obtained in this case ($\delta$ -O*D* = 5.41 ppm; no Fe–*D* resonance observed), indicating that the $^{Tol}Im^+$ substrate (*a*) does not impede $H_2$ heterolysis, (*b*) does not aid in stabilizing the implicit iron-deuteride intermediate, and (*c*) does not serve as a hydride acceptor in this system.

For the deprotonated phosphine congener **Fe-CNP'**, the analogous reaction with $D_2$ (5 atm, no model substrate, $^2H$ NMR analysis) results in the same phenol-O*D* resonance ($D^+$); again, no Fe–*D* resonance was detected. Additionally, a new resonance at 7.77 ppm (Figure 4.7B) was evident. We hypothesized that this feature was diagnostic of a deuterated methenyl-*D* linkage (i.e. the deprotonated methylene). A similar spectrum was obtained in the presence of the model substrate ($^{Tol}Im^+$), indicating that (like the **Fe-CNS** system) the **Fe-CNP** deuteride is neither stabilized by nor active for hydride transfer with the model substrate. Provided the similar reactivities between **Fe-CNS** and **Fe-CNP**, a schematic of the proposed reaction cycle for $D_2$ activation is displayed in Scheme 4.6.

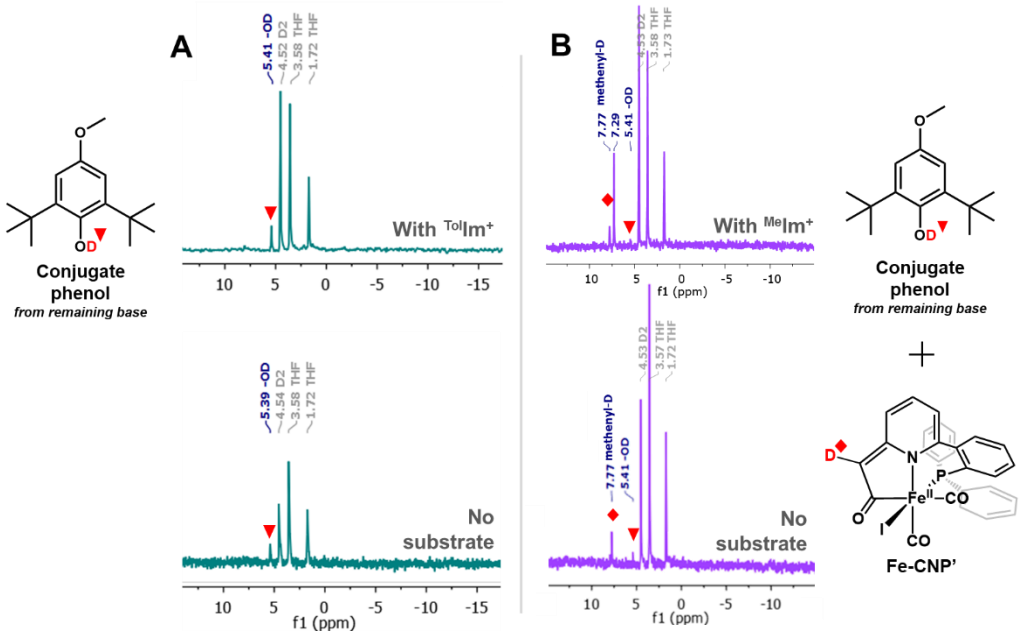


Figure 4.7: $^{2}H$ NMR spectra of $D_2$ activation by **Fe-CNS'** (A) or **Fe-CNP'** (B) with or without the presence of substrate ($Im^{+}$) in THF, exhibiting a resonance at 5.4 ppm from -O*D* of a conjugate phenol.

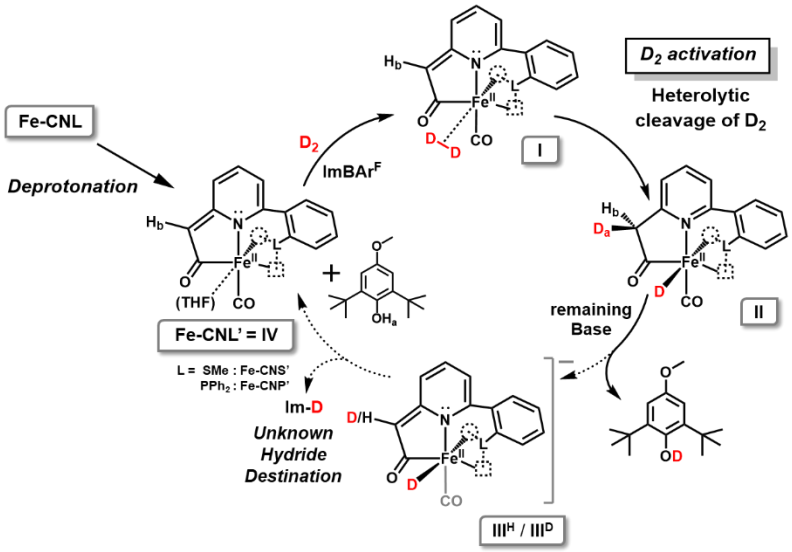


Scheme 4.6: A proposed mechanism of $D_2$ activation by **Fe-CNS'**/**Fe-CNP'**. The hollow wedged bond shown in grey for one carbonyl group represent the position either trans from iodide (**Fe-CNS'**) or trans from acyl (**Fe-CNP'**).

There is a plausible pathway to explain the new feature at 7.77 ppm (methenyl-*D*) in the **Fe-CNP** case. The iron-deuteride species **II** (resulting from $D_2$ activation, with methylene-$D_a$,$H_b$) may be re-deprotonated at $H_b$, thus affording the methenyl-$D_a$ anion $\mathbf{III^D}$. As this iron-deuteride species is not observable in the $^2$H NMR spectrum (no Fe–*D* resonance), the identity of the observed species is likely the 'post-hydride-transfer' product, $\mathbf{IV^D}$. The ultimate destination of the deuteride ($D^-$) has not yet been identified.

This proves that, at least for **Fe-CNP**, more than one round of cycle can take place, as a result of a slightly increased stability of species III with phosphine moiety (versus phenythioether) even in the absence of substrate stabilization. However, we still could not observe Fe–*D* signal from $^2$H NMR spectrum. In the presence of $^{Me}Im^+$ substrate, a preliminary $^2$H NMR spectrum (Figure 4.7B) exhibited the same methenyl-*D* feature at 7.77 ppm, a new feature at 7.29 ppm (undefined) and extremely weak phenol-O*D* 5.41 ppm. The use of $^{Me}Im^+$ substrate was with the intention of bringing the carbocation closer/making the carbocation more approachable to the Fe–*D* in the process of stabilization; however, even the use of less bulky $^{Me}Im^+$ did not lead to the detection of Fe–*D* resonance.

#### *4.2.3.3 Discussion*

Both meridional and facial Fe-acyl complexes (**Fe-CNS** and **Fe-CNP**, respectively) can activate $H_2$ when deprotonated. This indicates that in the presence of a formally deprotonated basic site on the ligand, the ability to activate $H_2$ does not depend on the binding mode of the ligand (*fac* versus *mer*). We have not acquired comparative kinetic data in the present work (both systems activate $D_2$ in <30 min) to provide more specific insight into the relative reactivities of **Fe-CNS'** versus **Fe-CNP'**. However, even if that data were acquired, the difference in donor type/strength between thioether-S and

diphenyl-P would preclude any conclusion regarding which tridentate orientation (*fac* versus *mer*) is preferable for efficient $D_2$ (or $H_2$) activation.

It is evident that the more indispensable factor that dictates the reactivity towards $H_2$ is the deprotonated methenyl(acyl) moiety, which acts as a pendent base during $H_2$ heterolysis. In the enzyme active site, the emergent postulate is that this role is accomplished by pyridone moiety (rather than the Cys-S as in [NiFe]). However, our system lacks the truly biomimetic and anionic pyridonate donor (i.e. the more stable deprotonated carboxamide resonance form), and instead employs the neutral pyridine as a substitute. Due to the pre-existing anionic charge in the (enzyme's) pyridone heterocycle, the methylene(acyl) p$K_a$ would be biologically inaccessible; its deprotonation would require the generation of a *di*-anionic (!) pyridone – unlikely. Therefore, *we are not claiming that the methylene/methenyl(acyl) interconversion is an active mechanism in the enzyme*. We do, however, the present system demonstrates the important utility of a pendant base in the vicinity of the iron center to drive $H_2$ heterolysis.

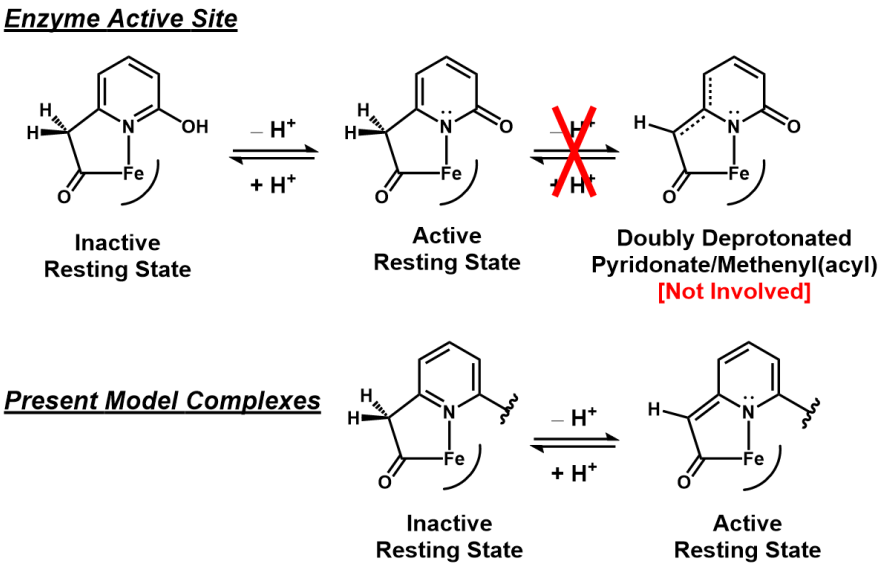


Scheme 4.7: Comparison of the enzyme active site versus the model complexes presented in this chapter, focusing on the pendant base.

By directly comparing the reactivity of **Fe-CNS**(acyl) with the published reactivity of its *carbamoyl* congener (i.e. -NH- linker in place of -$CH_2$- linker), namely [($C^{NH}$NS)Fe(CO)$_2$(Br)],[194] we postulate that the basicity of the carbamoyl unit ($sp^2$ NH with a lone pair) was not strong enough to promote $D_2$ heterolysis, as compared with the deprotonated methenyl(acyl) complexes in this work (**Fe-CN<u>L</u>'**). Another (functional) carbamoyl model reported by our group, [(Anth•$C^{NH}$NS)Fe(CO)$_2$(I)][101] does activate $H_2$ upon simple halide abstraction – i.e., without deprotonation. However, in this case the CNS ligation was strictly facial (via anthracene scaffold), which allows for an open coordination site *trans* from the Fe–C(acyl) bond. Kubas famously has stated that a strong *trans* σ donor promotes $H_2$ *heterolysis*, while a strong *trans* π-acceptor promotes $H_2$ *homolysis*.[3,7]

Thus, regarding $H_2$ activation, this work implies that the presence of an anionic pendant base on the ligand framework supercedes the *fac* versus *mer* ligation motif as a criterion for promoting $H_2$ activation. Based on previously published results,[101,102] it is then logical to postulate that the optimal scenario for maximizing catalytic efficiency would be to couple the presence of a pendant base with a facial ligation motif – with $H_2$ activation occurring at the coordination site *trans* to the Fe–C (acyl) bond. Such a scenario is thus exemplified by the evolution-tuned enzyme.

Regarding the hydride transfer, however, is not achieved in both *fac*-Fe-CNP' and *mer*-Fe-CNS'. We postulate that the presence of a π-accepting ligand (CO in **Fe-CNS'** and $PPh_2$ in **Fe-CNP'**) *trans* from the possible Fe–*D* unit is not favorable for the hydride to be transferred to a hydride acceptor. In the case of Hmd active site, a strongly σ-donating acyl group occupies that position, facilitating the hydride transfer by providing $e^-$ density from the *trans* position.

## 4.3 CONCLUSIONS

In summary, we were able to directly compare the electronic and steric effects on the binding mode of thioether versus triphenylphosphine moiety in Fe-acyl system by designing two asymmetric pincer ligands, **CNS** and **CNP**. **CNS** having thioether S is smaller in size and less σ-donating ligates meridionally, while **CNP** having bulkier and more strongly σ-donating triphenylphosphine P ligates facially. From reactivity studies, both **Fe-CNS** and **Fe-CNP**, regardless of the binding mode, activated $H_2$ when deprotonated in both the absence and presence of a model substrate. In this particular deprotonated Fe-acyl system, the binding mode of the ligand was not the important factor for the reactivity towards $H_2$ activation; rather, the presence of a pendant base (methenyl-acyl) was the most vital feature required for reactivity.

## 4.4 EXPERIMENTAL

### 4.4.1 Reagents and Procedures

$Fe(CO)_5$ and $Pd(PPh_3)_4$ were purchased from Strem Chemicals; 2-bromo-6-methylpyridine, $Pd(PPh_3)_2Cl_2$ from Oakwood Chemicals; 2-(methylthio)phenyl boronic acid from Boron Molecular and Matrix Scientific; 2-bromophenylboronic acid fromo Combi Blocks, Inc.; $I_2$ and $ClPPh_2$ from Acros Organics; 1.6 M *n*BuLi in hexanes and $D_2$ (99.8%) from Sigma-Aldrich; $K_2CO_3$ from Fisher Scientific.; Aluminum oxide (neutral, Brockmann I, 50–200 μm, 60 Å) from ACROS Organics; Silica (SiliaFlash® Irregular Silica Gels, 40–63 μm, 40 Å) from SiliCycle. The solvents dimethoxyethane (DME), ethyl acetate (EA) and 1,4-dioxane were purchased from Fisher Scientific and used without further purification. The solvents diethyl ether ($Et_2O$), dichloromethane (DCM), chloroform, tetrahydrofuran (THF) and pentane were procured from Fisher Scientific and dried over alumina columns using a Pure Process Technology solvent purification system, and stored over 3 Å molecular sieves until use. The deuterated solvent $CDCl_3$ was purchased from Cambridge Isotopes and used as received. Imidazolium ($Im^+$)[200] and the bulky phenolate base were synthesized following literature procedures. Infrared spectra were recorded on a Bruker Alpha spectrometer equipped with a diamond ATR crystal. $^1H$ and $^{31}P$ NMR spectra were collected using Varian DirecDrive 400 MHz, while $^2H$ NMR spectra were collected using 600 MHz. Elemental analyses were performed by Midwest Micro Lab.

### 4.4.2 Synthesis of Ligands

#### *4.4.2.1 2-Methyl-6-(2-(methylthio)phenyl)pyridine (CNS)*

A Suzuki coupling of 2-bromo-6-methylpyridine (4.0 g, 23 mmol) with 2-(methylthio)phenyl boronic acid (5.9 g, 35 mmol) was performed using 1 M $K_2CO_3$ (35

mmol) and *trans*-$Pd(PPh_3)_2Cl_2$ (816 mg, 1.2 mmol, 5 mol%) in 100 mL of DME. The slurry was heated at 85 °C for 24 h in a pressure vessel. The organic layer was collected by ethyl acetate (EA) extractions (3 × 100 mL) and dried over $Na_2SO_4$. Purification via column chromatography (EA:Hex = 1:8) afforded the product as pale yellow oil. Yield: 3.4 g (67%). $^1$H NMR ($CDCl_3$, δ in ppm): 7.64 (t 1H), 7.42 (d 1H), 7.34 (m 2H), 7.22 (t 1H), 7.13 (d 1H), 2.63 (s 3H), 2.39 (s 3H).

#### *4.4.2.2 2-(2-Bromophenyl)-6-methylpyridine*

A Suzuki coupling of 2-bromo-6-methylpyridine (3.27 g, 19.0 mmol) with 2-bromophenylboronic acid (4.20 g, 20.9 mmol, 1.1 equiv) was performed using $K_2CO_3$ (2.89 g, 20.9 mmol, 1.1 equiv) and $Pd(PPh_3)_4$ (769 mg, 0.66 mmol, 3.5 mol%) in 1,4-dioxane:$H_2O$ (3:1) mixture. The slurry was refluxed for 24 h. The organic layer was collected by EA extractions (3 × 100 mL) and dried over $Na_2SO_4$. Purification via column chromatography (EA:Hex = 1:8) afforded the product as pale yellow oil. Yield: 3.89 g (83%). $^1$H NMR ($CDCl_3$, δ in ppm): 7.64 (dd, t 2H), 7.51 (dd 1H), 7.37 (m 2H), 7.22 (dd 1H), 7.14 (dd 1H), 2.62 (s 3H).

#### *4.4.2.3 2-(2-(Diphenylphosphaneyl)phenyl)-6-methylpyridine (CNP)*

[Note: the synthetic conditions were modified from the work of Speiser et al.[201]] *Note: Rigorous air-free handling technique is required to isolate this product as the free phosphine (avoiding phosphine oxide).* A solution of *n*BuLi (1.6 M in hexanes, 16 mmol) was added dropwise into a freeze-pump-thawed solution of 2-(2-bromophenyl)-6-methylpyridine (3.97 g, 16 mmol) in THF at –78 °C. After stirring the solution at the same temperature for 1 h, $ClPPh_2$ (16 mmol) was added dropwise via syringe and let slowly come up to r.t. overnight. Degassed $H_2O$ was added via syringe, followed by multiple air-free $Et_2O$ extractions using cannula transfers. The organic layer was transferred to a $N_2$-purged

Schlenk flask containing $Na_2SO_4$ via cannula, and stirred for 30 min. The dried solution was then cannula transferred to a new Schlenk flask, and the volume was reduced under vacuum until a white powder was formed. The resulting yellow supernatant (impurities) was transferred into a separate Schlenk flask via cannula, and the remaining white powder (product) was washed several times with cold $Et_2O$, then dried under $N_2$. Storage of the supernatant and washes at –20 °C for 2 d afforded large colorless blocks suitable for X-ray diffraction. Yield: 2.94 g (52%). $^1$H NMR ($CDCl_3$, δ in ppm): 7.63 (m 1H), 7.53 (t 1H), 7.43 (td 1H), 7.3 (m 12H), 7.09 (dd 1H), 7.00 (d 1H), 2.31 (s 3H). $^{31}$P NMR ($CDCl_3$, δ in ppm): –10.9 (s). CCDC deposition #: 1590145.

### 4.4.3 Synthesis of Metal Complexes

#### *4.4.3.1 [Fe(CNS)I(CO)$_2$] (Fe-CNS)*

The **CNS** ligand (400 mg, 1.86 mmol) was dissolved in 10 mL of $Et_2O$ and degassed by freeze-pump-thaw method. Then it was cooled to –10 °C for the addition of *n*BuLi (1.6 M in hexanes, 1.86 mmol). After the addition, the reaction was stirred at r.t. for 45 min. After the formation of an orange slurry, a pre-chilled $Et_2O$ solution (3 mL) of $Fe(CO)_5$ (250 μL, 1.86 mmol) was added dropwise at –78 °C. The reaction mixture was stirred for about 1.5 h to reach –25 °C, then cooled down back to –78 °C for oxidation. Under dark, pre-chilled $Et_2O$ solution (7 mL) of $I_2$ (212 mg, 1.67 mmol) was added dropwise into the stirring solution via cannula transfer and kept at –78 °C for 2 h. A yellow-brown precipitate was isolated using an air-free filter tube and dried under $N_2$ (crude, 528 mg, 59%). A DCM solution of the crude product was then filtered through neutral alumina and layered with pentane at –25 °C to afford X-ray quality crystals (red-brown needles). $^1$H NMR ($CDCl_3$, δ in ppm): 7.36 (s 1H), 6.96 (s 1H), 6.82 (m 2H), 6.72 (t 1H), 6.61 (d 1H), 6.26 (d 1H), 5.46 (d 1H), 3.86 (d 1H), 2.00 (s 3H). Selected IR bands ($cm^{-1}$): 2032 ($\nu_{C\equiv O}$ vs), 1962 ($\nu_{C\equiv O}$

vs), 1662 ($\nu_{C=O}$ vs), 1583, 1572, 1474 (s), 1449, 1438 (s), 760, 744 (s). Elemental analysis for: calcd (Fe-CNS with residual solvents: 0.1 equiv DCM and 0.2 equiv pentane): C 40.75, H 2.92, N 2.78; found: C 40.90, H 2.80, N 2.41. CCDC deposition #: 1590122.

#### *4.4.3.2 [Fe(CNP)I(CO)$_2$] (Fe-CNP)*

The **CNP** ligand (500 mg, 1.42 mmol) was dissolved in 15 mL of $Et_2O$ and degassed by freeze-pump-thaw. The solution was cooled to –10°C for the addition of *n*BuLi (1.6 M in hexanes, 1.42 mmol). After the addition, the reaction was stirred at r.t. for 45 min. After the formation of an orange slurry, a pre-chilled $Et_2O$ solution (3 mL) of $Fe(CO)_5$ (191 $\mu$L, 1.42 mmol) was added dropwise at –78°C. The reaction mixture was stirred for about 1.5 h to reach –25°C, then again cooled to –78°C for oxidation. Under dark, pre-chilled $Et_2O$ solution (7 mL) of $I_2$ (0.162 g, 1.27 mmol) was added dropwise into the stirring solution and kept at –78°C for 2 h. A yellow-brown precipitate was isolated using an air-free filter tube, then dried under $N_2$ (crude, 615 mg, 78%). The crude was purified by dissolving in DCM and the loaded on short alumina (neutral) column in an $N_2$ atmosphere glovebox; the products were eluted using a series of solvents of increasing polarity (DCM→$CHCl_3$→THF). The final elution with THF produced a yellow solution, from which the product was collected via crystallization (vapor diffusion of pentane into the THF solution at r.t.). Small orange-brown clusters of X-ray quality crystals were generated after ~10 days. $^1$H NMR ($C_6D_6$, δ in ppm): 7.8–6.6 (m, 14H), 6.54 (d 1H), 6.46 (t 1H), 6.39 (d 1H), 5.44 (d 1H), 4.92 (d 1H); $^{31}$P NMR ($C_6D_6$, δ in ppm): 79.9 (s). Selected IR bands ($cm^{-1}$): 2011 ($\nu_{C\equiv O}$ vs), 1974 ($\nu_{C\equiv O}$ vs), 1637 ($\nu_{C=O}$ vs), 1590, 1473 (s), 1427, 1092 (s), 979, 765 (s), 742 (s), 691 (vs), 602 (vs), 565, 543, 509 (s). Elemental analysis for $C_{27}H_{19}FeINO_3P$, calcd: C 52.38, H 3.09, N 2.26; found: C 52.48, H 3.32, N 2.14. CCDC deposition #: 1590123.

### 4.4.4 X-ray Crystallography

Definitions used for calculating $R_w(F^2)$, R(F) and the goodness of fit, S, are given below. Tables of crystal data and refinement parameters and tables for bond lengths, angles and torsion angles are summarized in Appendix C.3.

$$R_w(F^2) = \sqrt{\frac{\sum w(|F_0|^2 - |F_C|^2)^2}{\sum w(|F_0|)^4}}$$

$$R(F) = \frac{\sum|F_0| - |F_C|}{\sum|F_0|} \quad \text{for reflections with } F_0 > 4(\sigma(F_0))$$

$$S = \frac{\sum w(|F_0|^2 - |F_C|^2)^2}{(n-p)}$$

#### *4.4.4.1 2-(2-(diphenylphosphaneyl)phenyl)-6-methylpyridine (CNP)*

Crystals grew as blocks from $Et_2O$ solution of **CNP** at –20°C. The analyzed crystal was cut from a larger crystal and had approximate dimensions of 0.23 × 0.11 × 0.09 mm. The data were collected on a Rigaku AFC12 diffractometer with a Saturn 724+ CCD using a graphite monochromator with Mo Kα radiation (λ = 0.71073 Å). The data were collected at 100 K using a Rigaku XStream low temperature device. Data reduction were performed using the Rigaku Americas Corporation's Crystal Clear version 1.40.[144] The structure was solved by direct methods using SIR2004[176] and refined by full-matrix least-squares on $F^2$ with anisotropic displacement parameters for the non-H atoms using SHELXL-2014/7.[152] Structure analysis was aided by use of the programs PLATON98[147] and WinGX.[148] The hydrogen atoms on carbon were calculated in ideal positions with isotropic displacement parameters set to 1.2 × $U_{eq}$ of the attached atom (1.5 × $U_{eq}$ for methyl hydrogen atoms).

The function, $\Sigma w(|F_0|^2 - |F_C|^2)^2$, was minimized, where $w = 1/[(\sigma(F_0))^2 + (0.0529*P)^2 + (3.6702*P)]$ and $P = (|F_0|^2 + 2|F_C|^2)/3$. $R_w(F^2)$ refined to 0.106, with R(F) equal to 0.039

and a goodness of fit, S, = 1.06. The data were checked for secondary extinction effects but no correction was necessary. Neutral atom scattering factors and values used to calculate the linear absorption coefficient are from the International Tables for X-ray Crystallography (1992).[149]

#### *4.4.4.2 [Fe(CNS)I(CO)$_2$] (Fe-CNS)*

Crystals grew as needles by layering pentane on the DCM solution of **Fe-CNS** at –25°C. The analyzed crystal was cut from a larger crystal and had approximate dimensions of 0.10 × 0.08 × 0.05 mm. The data were collected on a Rigaku AFC12 diffractometer with a Saturn 724+ CCD using a graphite monochromator with Mo Kα radiation (λ = 0.71073 Å). The data were collected at 153 K using a Rigaku XStream low temperature device. Data reduction were performed using the Rigaku Americas Corporation's Crystal Clear version 1.40.[144] The structure was solved by direct methods using SIR2004[176] and refined by full-matrix least-squares on $F^2$ with anisotropic displacement parameters for the non-H atoms using SHELXL-2014/7.[152] Structure analysis was aided by use of the programs PLATON98[147] and WinGX.[148] The hydrogen atoms on carbon were calculated in ideal positions with isotropic displacement parameters set to 1.2 × $U_{eq}$ of the attached atom (1.5 × $U_{eq}$ for methyl hydrogen atoms).

The function, $\Sigma w(|F_0|^2 - |F_C|^2)^2$, was minimized, where $w = 1/[(\sigma(F_0))^2 + (1.5194*P)]$ and $P = (|F_0|^2 + 2|F_C|^2)/3$. $R_w(F^2)$ refined to 0.043, with R(F) equal to 0.020 and a goodness of fit, S, = 1.15. The data were checked for secondary extinction effects but no correction was necessary. Neutral atom scattering factors and values used to calculate the linear absorption coefficient are from the International Tables for X-ray Crystallography (1992).[149]

#### *4.4.4.3 [Fe(CNP)I(CO)$_2$] (Fe-CNP)*

Crystals grew as small clusters of orange crystals by slow evaporation (THF/pentane). The analyzed crystal was cut from a cluster of crystals and had approximate dimensions of 0.11 × 0.06 × 0.06 mm. The data were collected on an Agilent Technologies SuperNova Dual Source diffractometer using a μ-focus Cu Kα radiation source (λ = 1.5418 Å) with collimating mirror monochromators. A total of 1064 frames of data were collected using w-scans with a scan range of 1° and a counting time of 9 seconds per frame with a detector offset of ± 41.4° and 25 seconds per frame with a detector offset of ± 112.0°. The data were collected at 100 K using an Oxford Cryostream low temperature device. Data collection, unit cell refinement and data reduction were performed using Agilent Technologies CrysAlisPro V 1.171.37.31.[150] The structure was solved by direct methods using SHELXT[151] and refined by full-matrix least-squares on $F^2$ with anisotropic displacement parameters for the non-H atoms using SHELXL-2014/7.[152] Structure analysis was aided by use of the programs PLATON98[147] and WinGX.[148] The hydrogen atoms were calculated in ideal positions with isotropic displacement parameters set to 1.2 × $U_{eq}$ of the attached atom (1.5 × $U_{eq}$ for methyl hydrogen atoms). The data crystal was twinned with twin law determined using CrysAlisPro.

The function, $\Sigma w(|F_0|^2 - |F_C|^2)^2$, was minimized, where $w = 1/[(\sigma(F_0))^2 + (0.1853*P)^2]$ and $P = (|F_0|^2 + 2|F_C|^2)/3$. $R_w(F^2)$ refined to 0.241, with R(F) equal to 0.093 and a goodness of fit, S, = 1.04. The data were checked for secondary extinction effects but no correction was necessary. Neutral atom scattering factors and values used to calculate the linear absorption coefficient are from the International Tables for X-ray Crystallography (1992).[149]

### 4.4.5 NMR Spectroscopy

#### *4.4.5.1 [Fe(CNP)I(CO)$_2$] (Fe-CNP)*

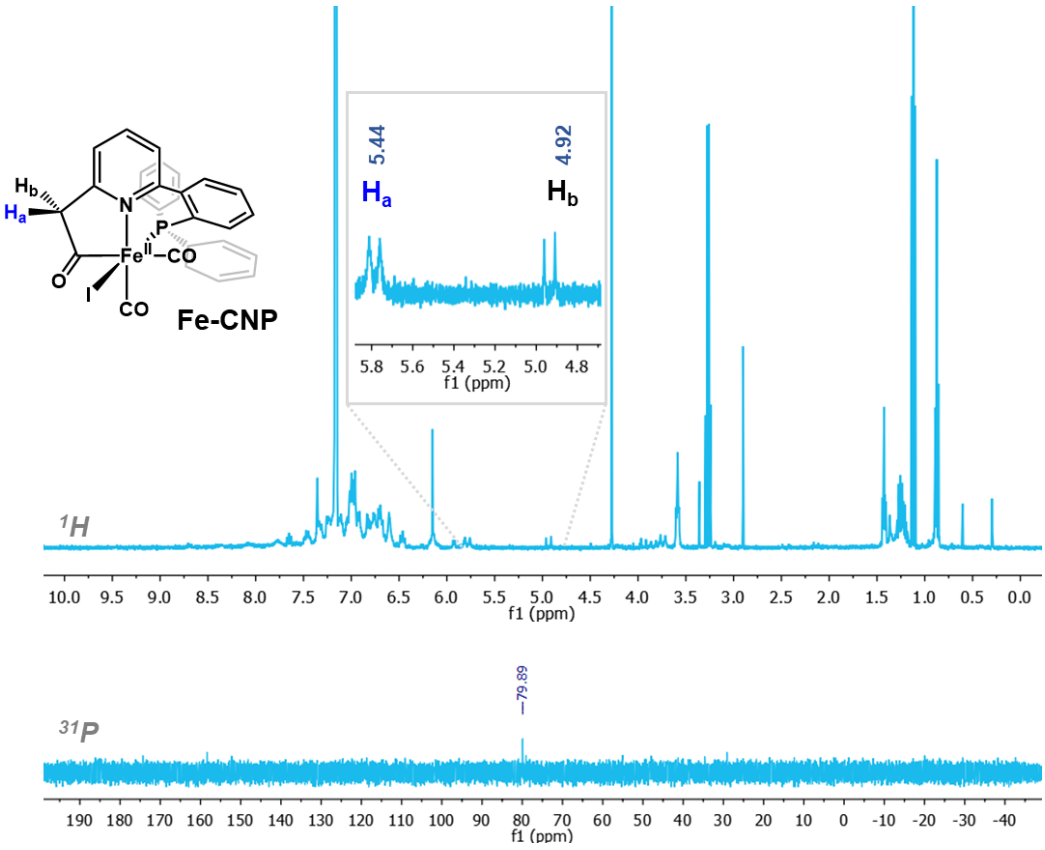


Figure 4.8: $^{1}$H (top) and $^{31}$P (bottom) NMR spectra for **Fe-CNP** in $C_6D_6$.

The $^{1}$H NMR spectrum of Fe-CNP in $C_6D_6$ (Figure 4.8) shows two diastereotopic protons at 5.44 and 4.92 ppm as doublets, and aromatic protons at 6.4–7.8 ppm region. The $^{31}$P NMR spectrum shows a single peak at 79.89 ppm for the phosphine P in the metal complex.

# Chapter 5: Thianthrene Scaffold: Flexibility-Reactivity Relationship

## 5.1 Introduction

### 5.1.1 Effect of Scaffold Flexibility on Reactivity

Metalloenzymes have dynamic motions, especially during catalysis. In the active site of a metalloenzyme, each donor atom almost always comes from different moieties such as different helices, sheets, domains, sub-units etc. In contrast, conventional bio-inspired small molecule mimics feature rather rigid/constrained scaffolds, mainly due to the difficulty replicating the vastly bigger protein structure with much 'smaller' molecules. Deeper investigation is necessary to decrease this gap between the flexible nature of a real enzymatic environment versus the rigidity of small molecule mimics' scaffold, as there are no critical, bioinorganic studies focusing on the effects of molecular motion on reactivity thus far.

Work by van Leeuwen on rhodium-anthranoid complexes revealed some correlation between the flexibility of scaffold and the catalysis: more flexible, anthranoid-supported rhodium complex displayed higher stability, and thus exhibited greater *n*:*i* (straight chain:branched) selectivity for hydroformylation compared to its more rigid counterparts with a linked bis-naphthyl framework. It is plausible to hypothesize that the extra flexibility on the scaffold could induce an enhanced accessibility to higher-in-energy (thus more reactive) intermediates, resulting greater reactivity.[97–99]

In case of Hmd, the activation of $H_2$ proceed through the conformational change (open/close) of the protein, which consequently give rise to dynamic movement of donor moieties on such as pyridone and cysteine-thiolate, as well as the substrates $H_2$ and $H_4MPT^+$. As a result of this 'flexibility', the energy barrier of the transition state(s) are likely lowered, thus the $H_2$ 'reactivity' is accomplished.

### 5.1.2 Thianthrene Versus Anthracene as Scaffold

The pioneering work by other Rose group members on anthracene-scaffold metal complexes are shown in Figure 5.1. A series of manganese complexes were synthesized by using symmetric/asymmetric anthracene-based ligands with pyridine and/or phenylthioether/thiolate substituents.[100] A variety of iron-anthracene complexes showed great possibility of mimicking the $H_2$ activation of Hmd.[101,102,192] These anthracene-based iron acyl/carbamoyl complexes reproduce the donor identities on the iron center, showing promising reactivities towards $H_2$.

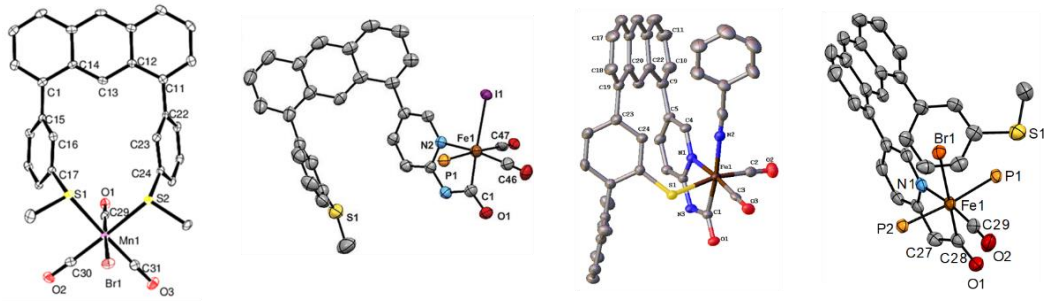


Figure 5.1: Previously studied anthracene-based manganese and iron complexes from our research group.[100–102,192]

However, the rigidity of the anthracene scaffold poorly imitates the actual active site's dynamic environment. Therefore, the main goal of this project was to investigate the effect of scaffold flexibility on the reactivity (more specifically, the rate of ligand substitution) of our group's iron-anthracene complexes towards $H_2$ activation by (*i*) enhancing flexibility on the scaffold through the use of thianthrene backbone and (*ii*) directly comparing the reactivity between the anthracene versions and the thianthrene analogues (Scheme 5.1).

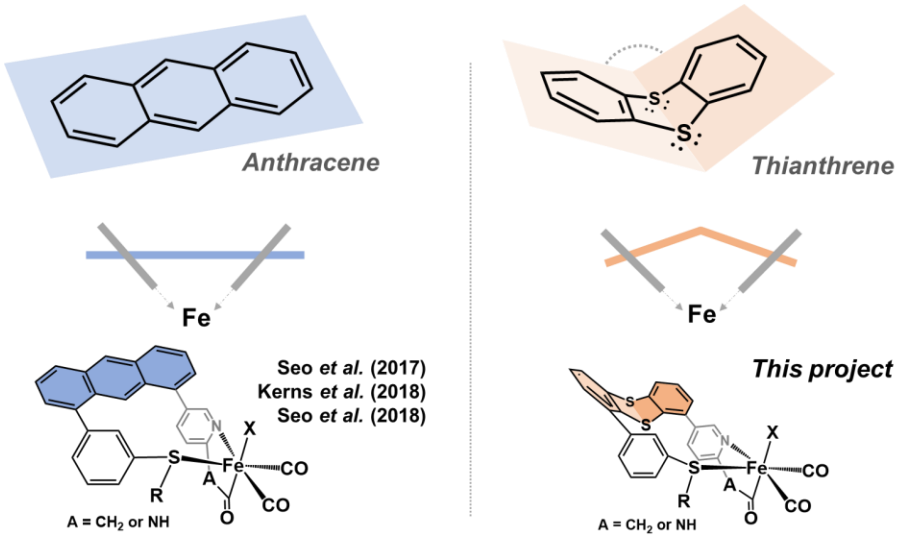


Scheme 5.1: Strategy of the thianthrene project, making the thianthrene versions of the anthracene-scaffolded iron-acyl/carbamoyl complexes.[101,102,192]

In contrast to essentially planar structure of anthracene, the structure of thianthrene is often described as 'butterfly' structure, based on its flapping motion about the S–S axis.[202–204] This flip-flop conformational change has a low energy barrier at equilibrium. From the crystal structure of thianthrene, the dihedral angle, or the 'butterfly angle', was found to be 128° at 295 K.[202] Even over a wide range of temperatures, this flapping motion is retained (from 127.14(3) to 130.37(3)° at temperatures from 125 to over 428 K).[202] In case of disubstituted thianthrene, namely 4,6-diphenylthianthrene, the observed butterfly angle was 124.7° (Figure 5.2). This is slightly more acute angle compared to the typical values for simpler thianthrenes (128-130°), and the two phenyl rings make an angle of 55.8° with respect to each other.[203]

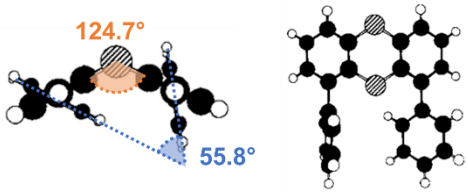


Figure 5.2: Chem3D™ representations of 4,6-diphenylthianthrene by Lovell *et al.*[203]

For comparative studies, thianthrene versions of the existing anthracene-scaffolded ligands was planned out (Figure 5.3). The ligands **Anth-$S_2$**, **Anth-$N_2$** and **Anth-$NS_{Me}$** were previously utilized for making Mn(I) carbonyl complexes,[100] whereas various types of **Anth-$N_AS_R$** were used for the synthesis of Fe(II) carbonyl complexes.[101,102,192] As this project is at its preliminary stage, **Thianth-$S_2$** and **Thianth-$N_2$** were the first two ligands to be synthesized and tested for complexation with a Mn(I) source for the direct comparisons with their corresponding anthracene counterparts, as well as some simple ligand substitution reactions (i.e. CO removal reaction using TMAO). Eventually, this project will aim to synthesize the iron-acyl/carbamoyl complexes of asymmetric-thianthrene ligand for investigation on structural and reactivity comparisons with their anthracene analogues (Scheme 5.1).

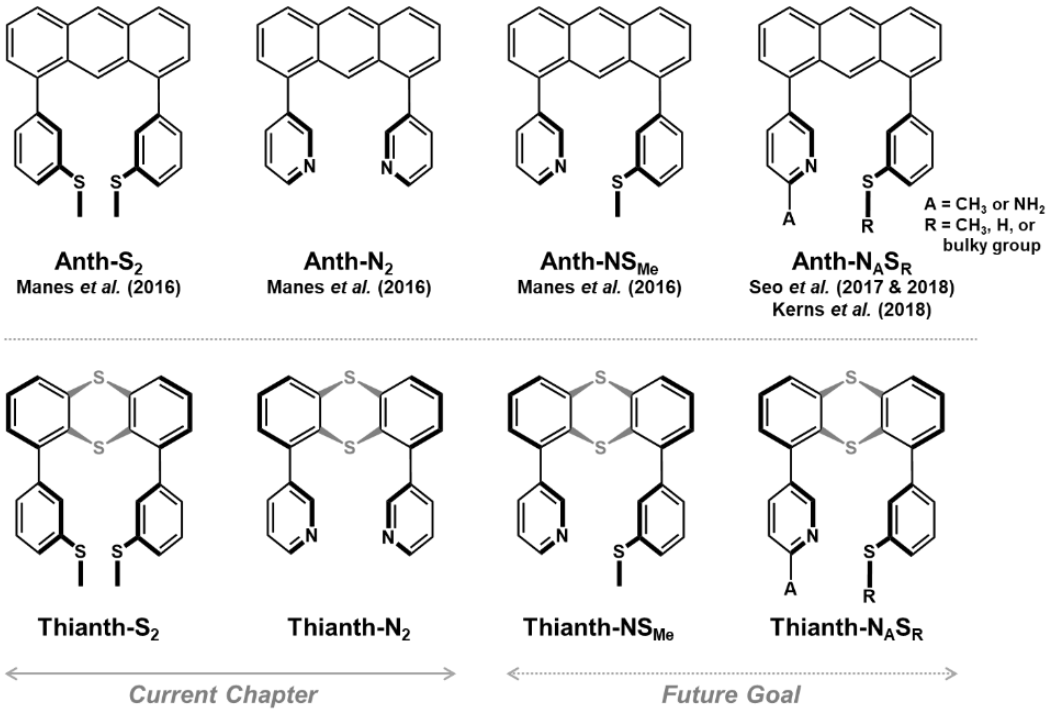


Figure 5.3: Series of previously studied anthracene-scaffolded ligands (top row) and the corresponding thianthrene-scaffolded ligands for this project (bottom row).

## 5.2 Results and Discussion

### 5.2.1 Synthesis Overview

#### *5.2.1.1 Ligand Synthesis*

The synthesis of the ligand **Thianth-S2** from thianthrene was inspired by the work of Lovell[203], Ogawa[205] and Sheikh et al.[204] with some modifications (Scheme 5.2). First, thianthrene was oxidized using 1.5 equivalents of purified *m*-chloroperoxobenzoic acid (*m*CPBA) to afford thianthrene 5-oxide (**Thianth-ox**) in 69% yield and some quantity of starting material after column purification. This step is easily scalable, up to 5 g scale of thianthrene. However, it should be only up to a reasonable scale, as using a large quantity of the oxidizing agent, *m*CPBA, could cause a safety hazard since it is a strong oxidizing agent that could cause fire upon contact with flammable material: it is potentially explosive. In consequence, purification of commercially obtained *m*CPBA (70-75%) is necessary because it contains up to 10% of *m*-chlorobenzoic acid and water for stabilization. Once purified, it is reasonably stable; however, it should be stored at relatively low temperature in a *plastic* container.

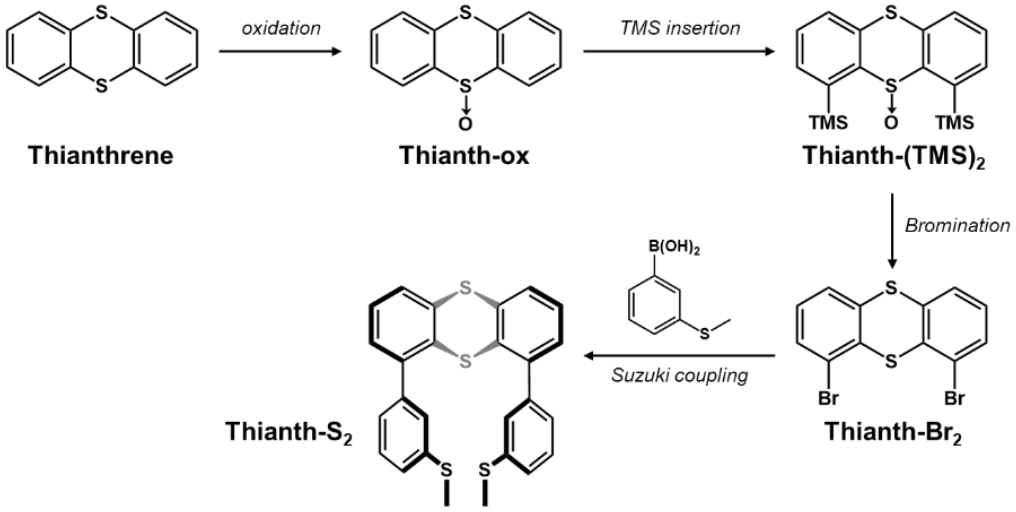


Scheme 5.2: Synthetic scheme for preparing **Thianth-Br2** from thianthrene.

The second step was the trimethylsilyl group addition, which required 2.5 equivalents of in situ generated lithium diisopropylamide (LDA) and 3.5 equivalents of trimethylsilyl chloride (TMS-Cl) to afford 50% of the pure 4,6-bis(trimethylsilyl)thianthrene 5-oxide (**Thianth-(TMS)$_2$**) as white solid. This was the most challenging step during the process of making the final ligand—when successful, the formation of white solid (pure product) is observed at the end of the work-up; upon failure, only a yellow oil is isolated due to side products such as mono- and/or tri-substituted thianthrene 5-oxides (4-(TMS) and 1,4,6-tris(TMS), respectively). Some of the possible reasons for the failure of the TMS insertion include using (*i*) deactivated LDA (by using either an old reagent directly from the bottle instead of in situ generation or using undistilled/degraded diisopropyl amine when making in situ LDA); (*ii*) not air-free TMS-Cl reagent; or (*iii*) some other as yet unidentified factors.

The third step was the simultaneous bromination and reduction of TMS groups and oxide, respectively, by reacting **Thianth-(TMS)$_2$** with $Br_2$ in distilled chloroform at room temperature. In the literature, $CCl_4$ has been used as solvent for this process; however, using chloroform still produced **Thainth-Br$_2$** with excellent yield (95%). However, the distillation of chloroform should not be neglected, since commercial chloroform contains up to 1% ethanol for stabilization, causing unwanted side reactions with $Br_2$. Therefore, removal of ethanol is the main purpose of the distillation. Lovell[203] and Ogawa[205] suggested a two-step process for making **Thainth-Br$_2$** (via reduction using AcCl/KI, followed by bromination using $Br_2$), whereas Sheikh[204] proposed the concurrent conversion (using $Br_2$ only). As the isolation of 4,6-bis(TMS)thianthrene was not necessary for this project, Sheikh's method was employed.

The last step was the Suzuki coupling of **Thianth-Br$_2$** with 3-(methylthio)phenyl boronic acid using $Pd(PPh_3)_4$ with $NaHCO_{3\,(aq)}$ in DME. This yielded **Thianth-S$_2$** as the

major product (92%) after column purification, which removed small amount of homocoupled side product, 3,3'-bis(methylthio)-1,1'-biphenyl. Several trials to couple a 3-pyridine moiety with **Thianth-Br$_2$** under similar conditions were not successful. It is possible that the sterically unhindered reagent, pyridine-3-ylboronic acid, deactivates Pd(0) catalyst by coordinating. In order to resolve the problem, Pd(dba)$_2$ was used with XPhos; however, this also did not afford any coupled product(s). Therefore, further investigations on the symmetric coupling of **Thianth-Br$_2$** with the pyridine moiety, as well as the asymmetric coupling with pyridine and thioether/thiolate are necessary in the long term, so that the direct comparison can be achieved with the anthracene-based Fe(II) complexes.[100–102,192]

#### *5.2.1.2 Synthesis of Mn(I) Complexes*

The complexation of the ligand **Thianth-S$_2$** with Mn(CO)$_5$Br was performed according to the previously reported procedure by our group, as shown in Scheme 5.3.[100] Although there is at present no X-ray structure evidence of the formation of **Mn-Thianth-S$_2$**, the product exhibited carbonyl stretches at 2015, 1933 and 1914 cm$^{-1}$, which are nearly identical to those of the anthracene version (2023, 1933 and 1918 cm$^{-1}$; Figure 5.3). This similarity indicates not only the formation of the thianthrene-analogue of **Mn-Anth-S$_2$** as the product, but also the negligible influence of scaffold flexibility on the donor strength of the donor atoms, and thus, the electronic environment on the metal center.

One contrast observed was that both the ligand **Thianth-S$_2$** and the complex **Mn-Thianth-S$_2$** showed enhanced solubility in organic solvents compared to their anthracene analogues. This can be explained with the X-ray structure of the **Mn-Anth-S$_2$**.[100] The measured distance of C13•••Mn1 is 6.405 Å (Figure 5.4). This means that the scaffold is

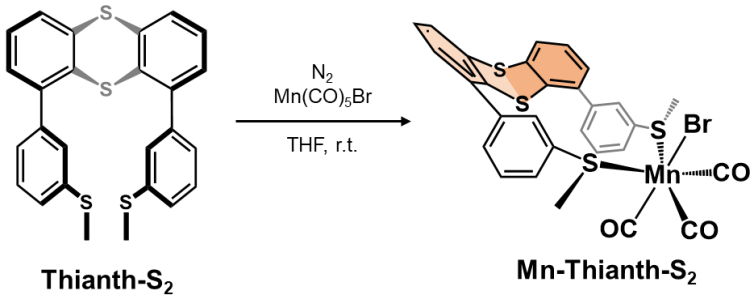


Scheme 5.3: Synthesis of **Mn-Thianth-S2** from **Thianth-S2** with $Mn(CO)_4Br$.

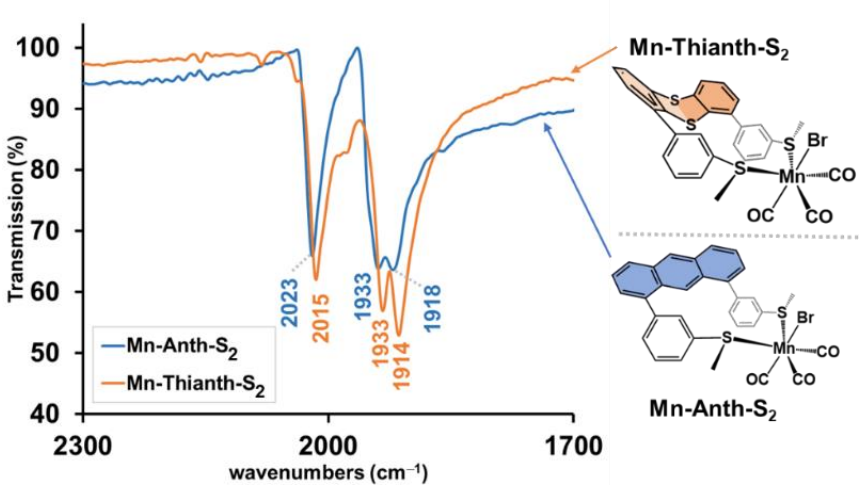


Figure 5.3: Infrared spectra of **Mn-Thianth-S2** (orange trace) and **Mn-Anth-S2**[100] (blue trace). Note the similarity of the CO stretches.

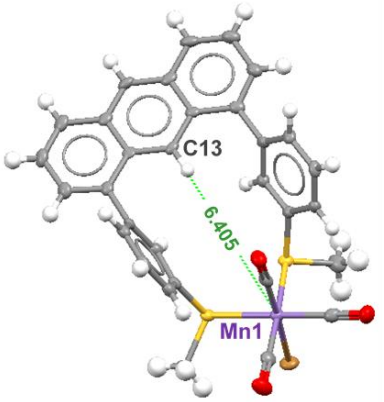


Figure 5.4: X-ray structure of **Mn-Anth-S2** showing the long-range distance between C13 and Mn1 of 6.405 Å.[100]

separated far enough from the metal center that the change in the scaffold's flexibility/dynamic does not greatly affect the structural and electronic environment on Mn(I) center. However, the flapping motion of thianthrene via two sulfur atoms may enhance the solubility of the ligand and the metal complex, compared to the anthracene versions. This was a desirable outcome since the anthracene-scaffolded ligands and metal complexes generally showed poor solubility in organic solvents, and therefore, by using the ligand **Thianth-S$_2$**, the solubility issue could be resolved without drastically changing the electronic environment of the metal center.

### 5.2.2 Reactivity Study

In order to compare the reactivity **Mn-Thianth-S$_2$** with **Mn-Anth-S$_2$**, CO removal via one equivalent of trimethylamine N-oxide (TMAO) was conducted on a THF solution of each complex. The CO removal (substitution with THF) reaction was chosen as a preliminary reactivity comparison study, based on its straightforward reaction and the feasibility of monitoring the progress by IR spectroscopy (Figure 5.5). At selected time points after the addition of TMAO, a small aliquot of the reaction was removed for drop-cast IR spectroscopy.

Both complexes showed an overall trend of the weakening of the CO stretch over time, though some exceptions (strengthening) were observed at certain stages of time. These outliers are likely due to the inconsistency of the concentration of the drop-casted sample for each IR measurement. Even with an effort to take out the same amount of the reaction mixture, the amount of compound that actually gets drop-casted can vary, which can cause the change of CO intensity in an unexpected direction. To reduce this issue, more reliable method such as solution IR spectroscopy or in situ IR spectroscopy should be attempted.

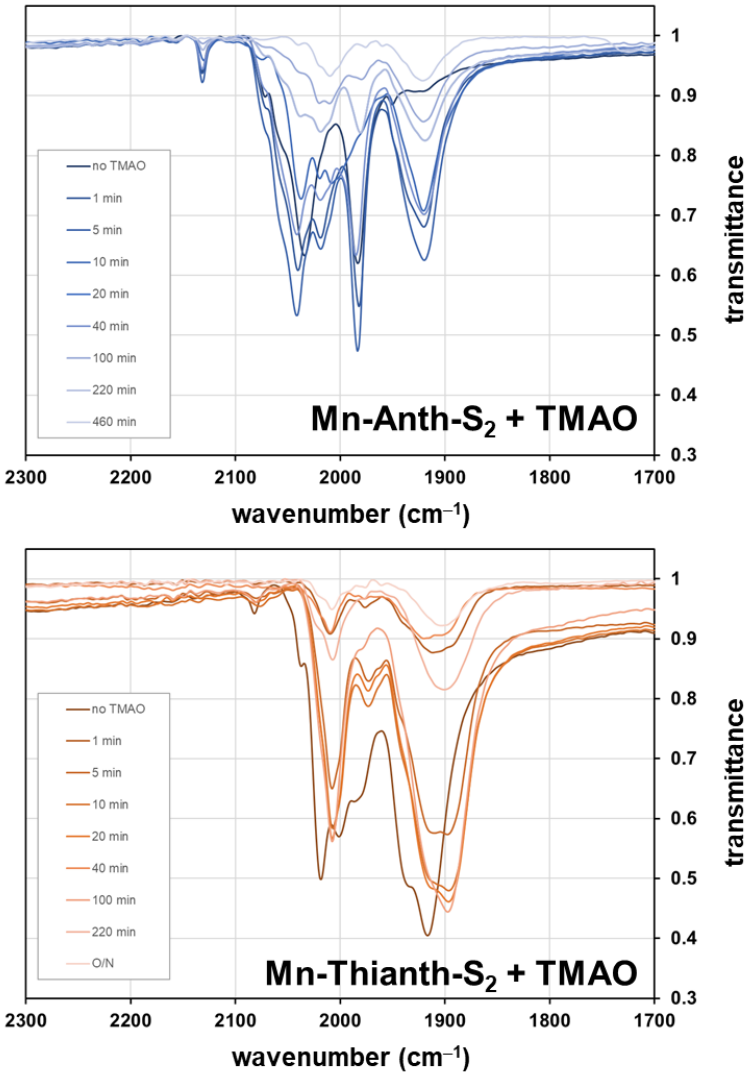


Figure 5.5: IR spectra of CO→THF substitution reaction over time using TMAO on **Mn-Anth-S2** (top) and **Mn-Thianth-S2** (bottom).

A preliminary kinetic study comparing the CO removal (substitution with THF) rates of **Mn-Anth-S2** with **Mn-Thianth-S2** is shown in Figure 5.6. The %CO substitution was deduced from the intensity of one of the carbonyl stretches from the IR spectra, where a strong CO stretch (low transmittance) represents low %CO substitution. It is notable that in case of **Mn-Thianth-S2**, approximately 95% CO substitution is observed 5 minutes after

the addition of TMAO, whereas **Mn-Anth-S$_2$** exhibits less than 20% CO substitution over much longer period of time. The negative % conversion values for **Mn-Anth-S$_2$** is probably due to, again, concentration change from solvent evaporation and/or difference in the amount of sample drop-casted for IR spectroscopy, as well as the variance in peak ν(CO) over time.

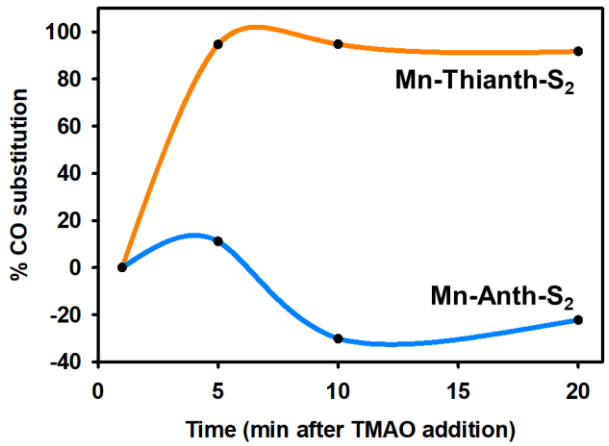


Figure 5.6: Kinetics of CO→THF substitution using TMAO for **Mn-Anth-S$_2$** (blue trace) and **Mn-Thianth-S$_2$** (orange trace).

### 5.3 Conclusion

In an effort to examine the hypothesis of flexibility-reactivity relationship, thianthrene-scaffold seems to be a good candidate for performing comparison studies with our existing anthracene-scaffolded metal complexes. Preliminary results show that by changing the scaffold from anthracene to thianthrene, the CO→THF substitution rate upon the addition TMAO as well as the solubility were improved, whereas the donor strengths of the donor atoms remained unchanged. Further investigation using a variety of thianthrene-scaffolded systems for comparative investigation is encouraging to unveil the effect of dynamic protein environment, presenting a new avenue for designing enzyme-inspired small molecules.

## 5.4 EXPERIMENTAL

### 5.4.1 Reagents and Procedures

Thianthrene was obtained from TCI Chemicals; 3-chloroperoxybenzoic acid was purchased from Acros Organics; bromine was purchased from Alfa Aesar. $Mn(CO)_5Br$ and $Pd(PPh_3)_4$ were purchased from Strem Chemicals. Diisopropylamine, n-BuLi (2.5 M in hexanes) and chlorotrimethylsilane were obtained from Sigma-Aldrich. The deuterated solvent $CDCl_3$ was purchased from Cambridge Isotopes and used as received. All ligand synthesis and metal complexation were performed under $N_2$ atmosphere. Once synthesized, the ligand and precursors were stable in ambient atmosphere.

### 5.4.2 Synthesis of Ligand and the Precursors

#### *5.4.2.1 Thianthrene 5-oxide (Thianth-ox)*

A batch of thianthrene (1.00 g, 4.62 mmol) was dissolved in 15 mL of DCM and cooled to 0 °C. Separately, 1.1 equivalent of purified *m*CPBA* (3-chloroperoxybenzoic acid, 0.878 g, 5.08 mmol) was dissolved in 15 mL of DCM, which was then cannula transferred into the thianthrene solution. Upon addition, white precipitate formed. After the reaction was stirred and maintained at 0 °C for 1 h, it was extracted with aqueous $NaHCO_3$ (3 × 15 mL) followed by $H_2O$ (2 × 20 mL) washes. The organic layer was dried over $Na_2SO_4$ then reduced under vacuum, which yielded white powder as a crude. Purification via column chromatography (EA:Hex = 1:5) afforded the product as colorless crystalline solid. Yield: 1.07 g (69%). When the reaction was scaled up to 5.00 g thianthrene, 3.09 g (58%) of the pure product was isolated. $^1$H NMR ($CDCl_3$, δ in ppm): 7.93 (dd 2H), 7.63 (dd 2H), 7.55 (dd 2H), 7.43 (td 2H).

*: Purification of commercially obtained *m*CPBA: 35.0 g of *m*CPBA (70-75%) was dissolved in 250 mL of dry $Et_2O$, then washed with buffer solution (410 mL of 0.1 M NaOH

combined with 250 mL of 0.2 M $KH_2PO_4$, then diluted up to 1 L to make pH 7.5; 3 × 150 mL). The organic layer was dried over $Na_2SO_4$ and *carefully* reduced under vacuum to afford pure *m*CPBA (24.5 g, 70%) as white chunks of solid. The product was stored in a plastic container and sealed with parafilm.

#### *5.4.2.2 4,6-Bis(trimethylsilyl)thianthrene 5-oxide (Thianth-(TMS)$_2$)*

A batch of **Thianth-ox** (2.00 g, 8.60 mmol) was dissolved in 25 mL of THF and cooled to –78 °C. Separately, a freshly generated LDA* (lithium diisopropylamine, 21.5 mmol, 2.5 equiv.) in THF was also cooled to –78 °C, then cannula transferred into the stirring solution of **Thianth-ox**, yielding a clear yellow solution. After the reaction was stirred for 3 h at –78 °C, the cooling bath was removed and the solution stirred at r.t. for 10 min to afford a brownish black solution, then cooled to –78 °C. Trimethylsilyl chloride (3.30 mL, 25.8 mmol, 3.0 equiv.), which was stored in the glove box, was added dropwise into the reaction via syringe. The reaction was allowed to warm to r.t. overnight, resulting a yellow solution, which was then quenched with 100 mL of $H_2O$. An additional 50 mL of chloroform was added, then washed with $H_2O$ (2 × 100 mL), followed by brine (2 × 100 mL). The organic layer was dried over $Na_2SO_4$ then reduced under vacuum, which yielded a white precipitate with yellow oil. The crude solid was washed with hexanes on filter to afford white solid as a pure product. Yield: 1.605 g (50%). $^1$H NMR ($CDCl_3$, δ in ppm): 7.72 (dd 2H), 7.63 (dd 2H), 7.44 (t 2H), 0.56 (s 18H).

*: *in situ* LDA (21.5 mmol) generation: To the stirring solution of distilled diisopropyl amine** (21.5 mmol, 3.01 mL) in 5 mL of THF at –78 °C, 2.5 M n-BuLi in hexanes (22.6 mmol, 9.03 mL) was added dropwise to generate a slightly hazy and off-white colored solution.

**: Diisopropyl amine could degrade over time in ambient condition without a SureSeal. Therefore, distillation is required if the reagent bottle has been opened for long time.

#### *5.4.2.3 1,9-Dibromothianthrene (Thianth-$Br_2$)*

In a 50 mL Schlenk flask with 30 mL of distilled* chloroform, **Thianth-$(TMS)_2$** (1.50 g, 3.98 mmol) was dissolved and purged with $N_2$. Under $N_2$, $Br_2$ (1.44 mL, 27.9 mmol, 7.0 equiv.) was added dropwise into the stirring solution via syringe, generating a dark orange-brown solution. After stirring under $N_2$ for 24 h avoiding direct light, the reaction was quenched with 15 mL of 1 M $Na_2SO_{3\,(aq)}$, followed by $H_2O$ washes (2 × 100 mL). A small amount of distilled chloroform was added, dried over $Na_2SO_4$, then reduced under vacuum to afford a yellow solid (white solid with yellow oil). The crude was dissolved in small amount of toluene and set up for slow evaporation overnight. Crystalline solids were washed with minimum amount of fresh toluene, followed by hexanes to yield white crystals as pure product. More product was collected from the washes, as well. Yield: 1.42 g (95%). $^1$H NMR ($CDCl_3$, δ in ppm): 7.54 (d 2H), 7.42 (dd 2H), 7.10 (t 2H).

*: to completely remove residual ethanol in commercial chloroform, which reacts with $Br_2$.

#### *5.4.2.4 1,9-Bis(3-(methylthio)phenyl)thianthrene (Thianth-$S_2$)*

For a Suzuki coupling, **Thainth-$Br_2$** (100 mg, 0.267 mmol) was dissolved in 10 mL of DME with $Pd(PPh_3)_4$ (19.0 mg, 0.016 mmol, 6.0 mol%) at r.t. for 10 min. Separately, 3-(methylthio)phenyl boronic acid (135 mg, 0.802 mmol, 3.0 equiv.) was dissolved in 5 mL of DME with 3 mL of 1 M $NaHCO_{3\,(aq)}$, degassed. This slurry was added to the **Thianth-$Br_2$** solution, then refluxed for 4 h with vigorous stirring. After solvent was removed, 15 mL of $H_2O$ was added, then extracted with $Et_2O$ (3 × 10 mL). The organic layer was washed with $H_2O$ and brine, dried over $MgSO_4$, and reduced under vacuum. Purification via column chromatography (hexanes) afforded the product as colorless crystalline solid. Yield: 113

mg (92%). $^{1}$H NMR ($CDCl_3$, δ in ppm): 7.56 (d 2H), 7.29 (t 2H), 7.22 (m 4H), 7.17 (t 2H), 7.13 (s 2H), 7.00 (d 2H), 2.43 (s 6H).

### 5.4.3 Synthesis of Metal Complex

#### *5.4.3.1 [Mn(Thianth-S$_2$)(CO)$_3$Br] (Mn-Thianth-S$_2$)*

The ligand **Thianth-S$_2$** (50.0 mg, 0.109 mmol) was dissolved in 5 mL of THF, yielding a yellow solution. Separately, $Mn(CO)_5Br$ (29,8 mg, 0.109 mmol) was dissolved in 5 mL of THF and added to the ligand solution dropwise under $N_2$ (glove box) at room temperature. After stirring overnight, the reaction was reduced under vacuum to generate yellowish-sage gooey foam. After addition of several mL of $Et_2O$, a sage solid precipitated out from the yellow solution. After filtering the slurry through Celite, the yellow filtrate was reduced under vacuum to afford bright yellow solid as a pure product. Yield: 40.8 mg (55%). Selected IR bands ($cm^{-1}$): 2015 (vs), 1933 (vs), 1914 (vs), 1561 (w), 1440 (m), 1384 (m), 1256 (s), 1087 (br, s), 1013 (br, s), 966 (s), 785 (vs), 748(s), 728 (s), 694 (vs), 669 (s), 624 (vs), 512 (m).

# Appendix A: Pyridone Project

## A.1 Introduction

The goal of this project was to incorporate the pyridone moiety, which is considered as a pendant base in the active site of [Fe] hydrogenase during the $H_2$ activation catalysis, into 3- or 4-donor chelate system (NNS or N4-type ligands, respectively) as shown in Scheme A.1.

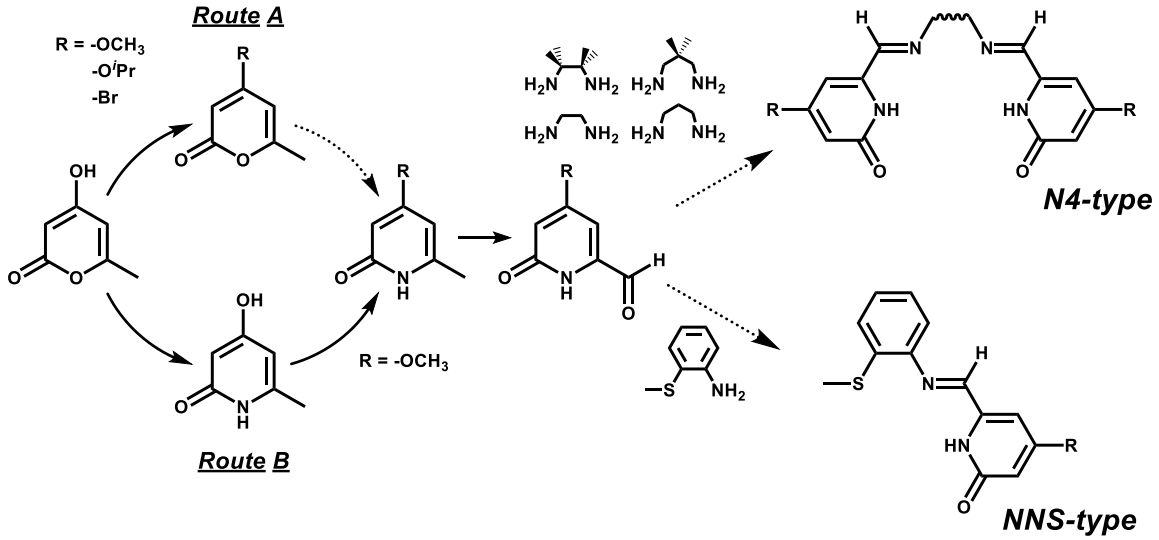


Scheme A.1: Overall scheme showing the goal of this project from 4-hydroxy-6-methyl-2-pyrone to N4-type or NNS-type ligands.

## A.2 Experimental

### A.2.1 Route A

Route A: First substitute the hydroxy proton of 4-hydroxy-6-methyl-2-pyrone with different R groups, then make the corresponding pyridones.

### *A.2.1.1 4-Bromo-6-methyl-2-pyrone*[206]

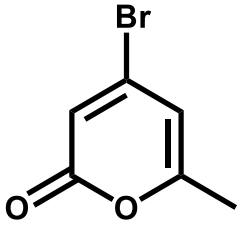


In 30 mL of DMF, 4-hydroxy-6-methyl-2-pyrone (1.00 g, 7.93 mmol) was dissolved and cooled down to 0 °C. Separately, 3 equiv. of $PBr_3$ (3.28 mL, 23.8 mmol) was dissolved in 30 mL of $Et_2O$ and added to the DMF solution of pyrone dropwise over the course of 1 h. The reaction changes from a transparent lemon-yellow solution to creamy white slurry with precipitate. Then, the reaction was refluxed at 60 °C for 20 h, which formed a very dark brown solution with dark orange precipitate. Once the reaction was cooled down, 100 mL of $H_2O$ was added and extracted with $Et_2O$ (6 × 150 mL), followed by $H_2O$ washes (3 × 100 mL). The organic layer was collected, dried over $Na_2SO_4$ and reduced under vacuum to generate a yellow solid. Purification via column chromatography (Hex:$Et_2O$=1:1) afforded the product as an ivory crystalline solid. Yield: 0.776 g (52%). $^1$H NMR ($CDCl_3$, δ in ppm): 6.46 (s 1H), 6.19 (s 1H), 2.25 (s 3H). Selected IR bands ($cm^{-1}$): 1713 (m), 1614 (m), 1542 (m), 1302 (m), 1259 (s), 1210 (m), 1128 (m), 1083 (s), 1041 (s), 1027 (s), 983 (s), 863 (s), 831 (s), 796 (vs), 726 (m), 625 (m), 579 (s), 513 (s).

### *A.2.1.2 4-Methoxy-6-methyl-2-pyrone*

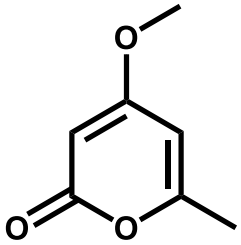


In 30 mL of acetone, 4-hydroxy-6-methyl-2-pyrone (2.00 g, 15.9 mmol) was dissolved. To the stirring slurry solution, $K_2CO_3$ (4.39 g, 31.8 mmol) and dimethylsulfate (1.71 mL, 18

mmol) were added sequentially. The slurry solution was refluxed for 3 h, which generated a slightly yellow solution with beige precipitate. Once cooled down, saturated $NH_4Cl_{(aq)}$ was added to the stirring solution until all precipitate dissolved. This solution was extracted with EA several times. The yellow organic layer was collected, dried over $Na_2SO_4$ and reduced under vacuum to afford light yellow solids. Purification via column chromatography (Hex:EA=3:1) afforded the product as lemon-yellow solid. Yield: 0.687 g (31%). $^1$H NMR ($CDCl_3$, δ in ppm): 5.78 (s 1H), 5.47 (s 1H), 3.79 (s 3H), 2.21 (s 3H). Selected IR bands ($cm^{-1}$): 1738 (m), 1715 (s), 1647 (vs), 1567 (vs), 1462 (s), 1434 (m), 1406 (s), 1325 (m), 1249 (vs), 1148 (s), 1047 (m), 1026 (s), 938 (s), 867 (m), 823 (vs), 817 (vs), 569 (vs).

***A.2.1.3 4-Isopropoxy-6-methyl-2-pyrone***

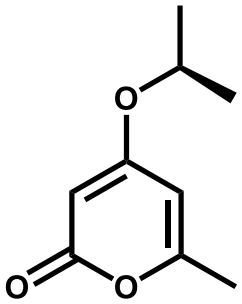


In 50 mL of DMF, 4-hydroxy-6-methyl-2-pyrone (4.00 g, 31.8 mmol) was dissolved. To the stirring slurry solution, $K_2CO_3$ (8.77 g, 63.6 mmol) and isopropylbromide (3.56 mL, 38 mmol) were added sequentially. The slurry solution was refluxed for 4 h, which generated a yellow solution with beige precipitate. Once cooled down, saturated $NH_4Cl_{(aq)}$ was added to the stirring solution until all precipitate dissolved. This solution was extracted with EA several times. The yellow organic layer was collected, dried over $Na_2SO_4$ and reduced under vacuum to generate white and yellow solids. Purification via column chromatography (Hex:EA=5 to 7:1) afforded white transparent crystals with yellow oil. A

final wash with hexanes afforded the product as white transparent crystals. Yield: 2.52 g (47%). $^{1}$H NMR ($CDCl_3$, δ in ppm): 5.71 (s 1H), 5.35 (s 1H), 4.49 (septet 1H), 2.18 (s 3H), 1.32 (d 6H). Selected IR bands ($cm^{-1}$): 1736 (m), 1711 (s), 1648 (vs), 1555 (vs), 1412 (s), 1257 (s), 1147 (s), 1137 (s), 1102 (s), 1032 (m), 998 (m), 908 (m), 857 (vs), 843 (vs), 803 (vs).

### A.2.2 Route B

Route B: First convert 4-hydroxy-6-methyl-2-pyrone into its corresponding pyridone, then substitute the hydroxy proton with different R groups.

#### *A.2.2.1 4-Hydroxy-6-methyl-2-pyridone*

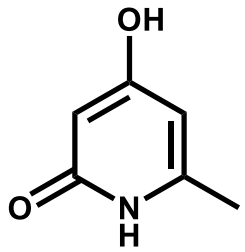


[Note: The procedure was followed by the literature by Demuner et al.[207]] In 250 mL of $NH_4OH$, 4-hydroxy-6-methyl-2-pyrone (20.0 g, 159 mmol) was dissolved, which provided a yellow transparent solution. After the reaction was refluxed for 8 h at 75 °C, it was cooled in an ice bath while stirring, generating a green solution within minutes. The addition of saturated $NaHSO_{4(aq)}$ to decrease the pH from ~8 to 3, which generated a thick yellowish gray slurry. Vacuum filtration followed by $H_2O$ wash afforded the pure product in quantitative yield. $^{1}$H NMR ($(CD_3)_2SO$, δ in ppm): 10.97 (s 1H), 10.41 (s 1H), 5.58 (m 1H), 5.32 (d 1H), 2.06 (d 3H). Selected IR bands ($cm^{-1}$): 1633 ($\nu_{C=O}$ vs), 1660 (vs), 1448 (m), 1351 (m), 1265 (s), 1232 (vs), 1172 (m), 901 (m), 829 (vs), 627 (m), 595 (s), 534 (vs), 512 (s), 408 (m).

*A.2.2.2 4-Methoxy-6-methyl-2-pyridone*

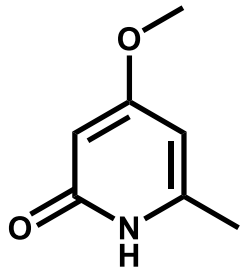


In 20 mL acetone, 4-hydroxy-6-methyl-2-pyridone (8.00 g, 63.9 mmol) was dissolved. To the stirring solution, $KHCO_3$ (12.8 g, 128 mmol) was added and heated for 15 min at 45 °C. Then, dimethylsulfate (7.21 mL, 1.2 equiv., 76.7 mmol) was added and refluxed for 10 h at 75 °C, which generated a slightly yellow solution with white precipitate. After the reaction was cooled down, saturated $NH_4Cl_{(aq)}$ was added and extracted with EA. The organic layer was dried over $Na_2SO_4$ and reduced under vacuum to generate light yellow solid as a crude product, which was washed with EA on the filter and dried to afford a pale yellow cream-colored solid as a pure product. Yield: 1.84 g (21%). $^1$H NMR ($(CD_3)_2SO$, δ in ppm): 11.05 (s 1H), 5.66 (s 1H), 5.50 (s 1H), 3.67 (s 3H), 2.07 (s 3H). Selected IR bands ($cm^{-1}$): 1638 ($\nu_{C=O}$ vs), 1450 (vs), 1431 (s), 1385 (m), 1233 (vs), 1200 (m), 1159 (s), 1053 (m), 940 (m), 919 (m), 824 (vs), 636 (m), 586 (s), 551 (vs).

**A.2.3 4-Methoxy-6-pyridone-2-carbaldehyde**

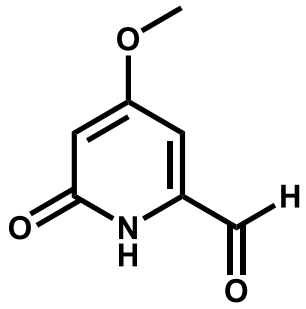


A batch of 4-methoxy-6-methyl-2-pyridone (500 mg, 3.59 mmol) was dissolved in 1,4-dioxane and $SeO_2$ (700 mg, 1.8 equiv., 6.31 mmol) was added. After the reaction was

heated at 100-110 °C for 1 h, the reaction mixture was filtered through Celite with a layer of $Na_2SO_4$ with more dioxane to remove $SeO_2$ that became gray. The yellow filtrate was then reheated at 100-110 °C with a second batch of $SeO_2$ (700 mg). This was repeated until the 4$^{th}$ addition of $SeO_2$ (total of 2.80 g = 7.2 equiv. $SeO_2$ added). The dioxane solution was cooled and reduced under vacuum to afford a crude product as brick-red sticky solids. Yield: 620 mg (quantitative, selenium impurity not removed). $^1$H NMR ($(CD_3)_2SO$, δ in ppm for the desired product): 9.53 (s 1H), 6.72 (s 1H), 6.06 (s 1H), 3.79 (s 3H). Selected IR bands ($cm^{-1}$): 1702 ($\nu_{CH=O}$ m), 1622 ($\nu_{C=O}$ vs), 1554 (m), 1443 (m), 1416 (m), 1342 (m), 1268 (m), 1230 (vs), 1148 (s), 1031 (s), 960 (m), 931 (s), 906 (s), 842 (m), 829 (vs), 621 (m), 553 (s), 458 (s).

**A.2.4 Pyridone-N4 Ligand**

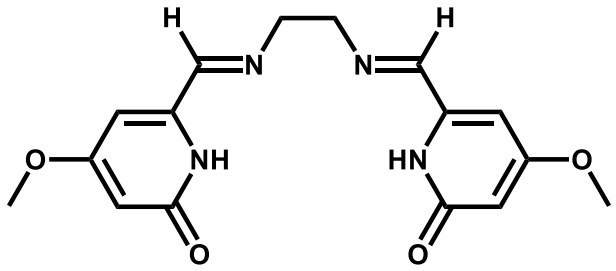


A batch of 4-methoxy-6-pyridone-2-carbaldehyde (2.50 g, 16.3 mmol) was dissolved in 25 mL MeOH, then filtered to generate an orangish-brown solution. To this solution, pre-dissolved ethylenediamine (0.546 mL, 8.16 mmol) solution of MeOH (~5 mL) was added dropwise, providing the color change to almost black with hint of yellow. The reaction was stirred overnight at room temperature. By gently blowing $N_2$, red-brown solids were observed, which presumably is the selenium byproduct from the previous reaction of making 4-methoxy-6-pyridone-2-carbaldehyde. Even after multiple filtrations, the red brown solid was not completely removable from the reaction mixture. $^1$H NMR ($(CD_3)_2SO$, δ in ppm for the desired product): 8.02 (s 2H), 5.98 (s 2H), 5.55 (s 2H), 4.74 (s 4H), 3.75

(s 6H). Selected IR bands ($cm^{-1}$): 1637 ($\nu_{C=O}$ vs), 1610 (vs), 1582 (m), 1437 (m), 1406 (m), 1376 (vs), 832 (s), 822 (s).

**A.2.5 Pyridone-NNS Ligand**

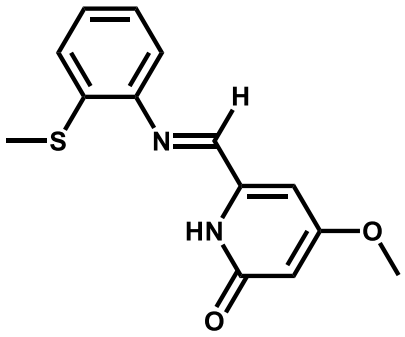


A batch of 4-methoxy-6-pyridone-2-carbaldehyde (96.2 mg, 0.628 mmol) was dissolved in 8 mL MeOH and filtered to generate a transparent orange solution. Separately, 2-methylthioaniline (0.0787 mL, 0.628 mmol or more) was dissolved in 1.5 mL of MeOH, then added dropwise into the aldehyde solution. The reaction was stirred overnight at room temperature, which afforded an orange solution with small amount of brown precipitate. The crude $^1H$ NMR spectrum was acquired to show the mixture of 2-methylthioaniline and the NNS ligand present, with no sign of 4-methoxy-6-pyridone-2-carbaldehyde. Attempts to isolate the NNS ligand from the crude product was unsuccessful. $^1H$ NMR of the crude product, listing the peaks for only the NNS ligand ($(CD_3)_2SO$, δ in ppm): 10.15 (br), 8.296 (s 1H, imine), 7.28 (m 3H), 7.153 (m 2H), 5.949 (s 1H), 3.788 (s 3H, -OMe), 2.413 (s 3H, -SMe). Selected IR bands ($cm^{-1}$): 1674 ($\nu_{C=O}$ vs), 1645 (s), 1607 (m), 1469 (m), 1452 (s), 1438 (m), 1379 (m), 1232 (vs), 1210 (s), 1154 (m), 965 (m), 954 (m), 860 (m), 812 (s), 760 (m), 736 (s), 725 (m), 587 (m).

## A.3 CONCLUSION

For synthesizing substituted pyridone from 4-hydroxy-6-methyl-2-pyrone, synthetic route B was successful, which makes the hydroxy-pyridone first, then substitute the hydroxy group with other alkyl groups, rather than making the substituted pyrone first.

Converting the methyl group of 4-methoxy-6-methyl-2-pyridone into aldehyde required sequential addition of $SeO_2$ (total of 7.2 equivalents) over 4 additions, removing the decomposed $SeO_2$ each time. However, residues of $SeO_2$ could not be completely removed from the product even after the following condensation reactions, which interrupted the clean isolation of **pyridone-N4** and **pyridone-NNS** ligands (only spectroscopically characterized via $^1H$ NMR). Improved experimental procedure for removing the $SeO_2$ residue seems critical for the project.

# Appendix B: Spectra and Plots

## B.1 Chapter 2 Spectra

### B.1.1 ($\mu$-OH)-($\mu$-$\eta^1$-$O_2$)-[$(enN_4)_2Co_2$]$(BF_4)_3$ (**1**$(BF_4)_3$)

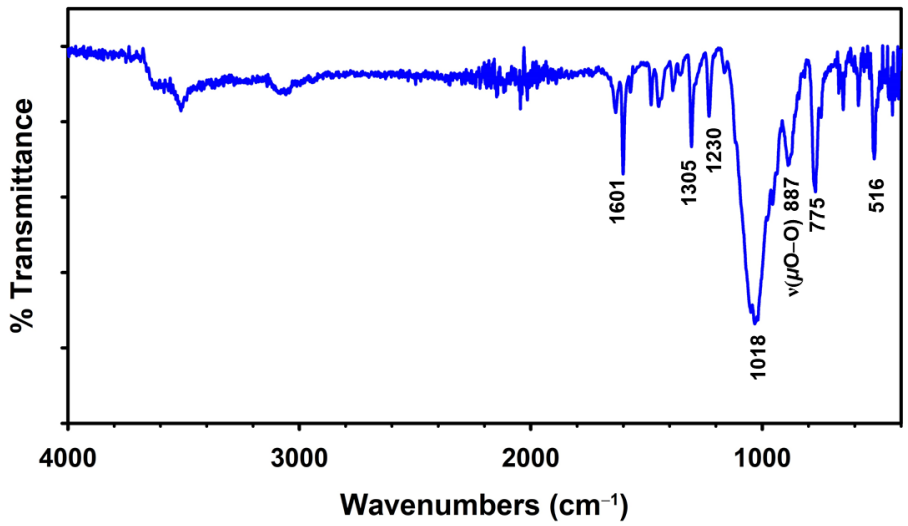


Figure B.1: Infrared spectrum of **1**$(BF_4)_3$.

### B.1.2 ($\mu$-OH)-($\mu$-$\eta^1$-$O_2$)-[$(enN_4)_2Co_2$]$(ClO_4)_3$ (**1**$(ClO_4)_3$)

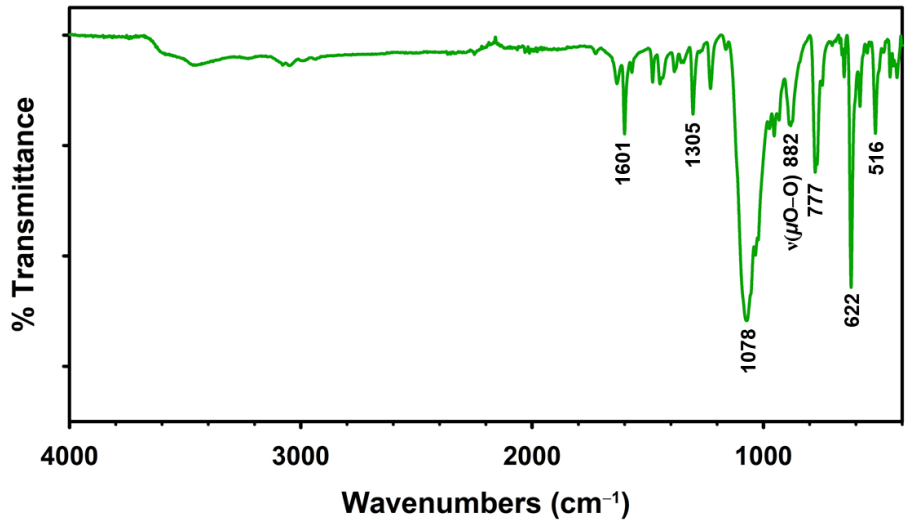


Figure B.2: Infrared spectrum of **1**$(ClO_4)_3$.

### B.1.3 ($\mu$-OH)-($\mu$-$\eta^1$-$O_2$)-[($enN_4$)$_2$$Co_2$]($PF_6$)$_3$ (1($PF_6$)$_3$)

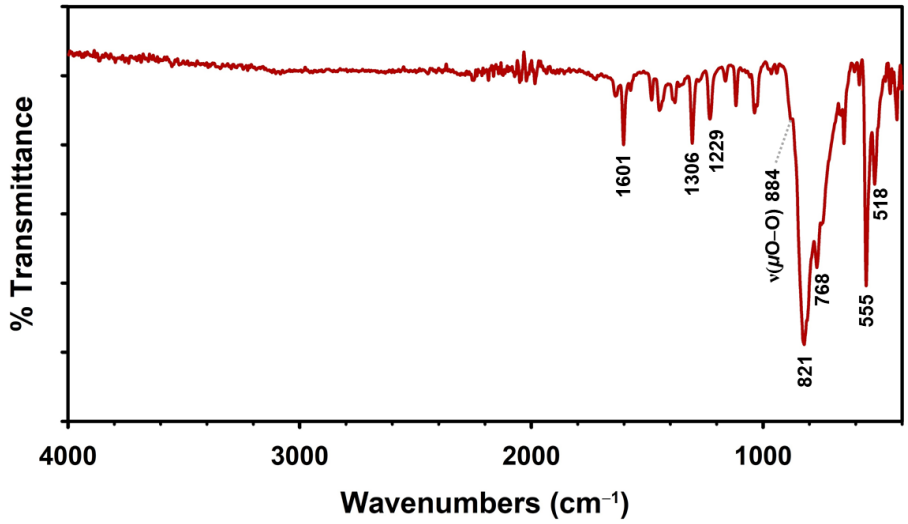


Figure B.3: Infrared spectrum of **1($PF_6$)$_3$**.

## B.2 CHAPTER 3 PLOTS

### B.2.1 [$Co_2$(μ-F)($pnN_4$-PhCl)$_2$($OH_2$)(MeCN)]($BF_4$)$_3$ ($F^1$)

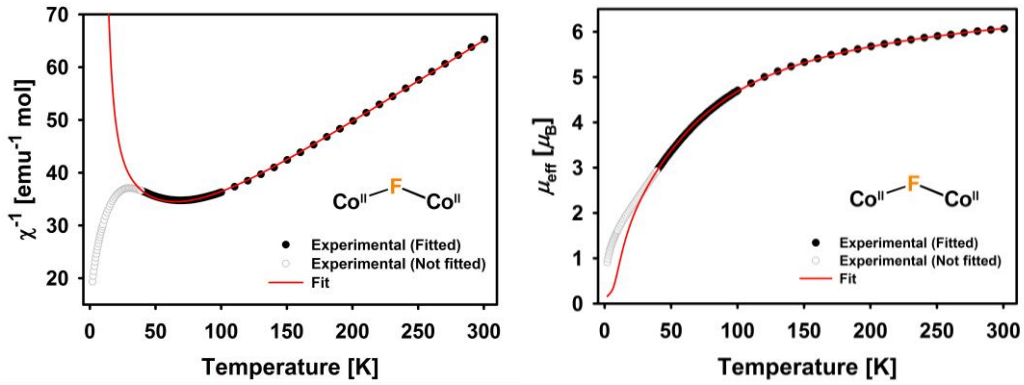


Figure B.4: The reciprocal χ vs T (left) and $\mu_{eff}$ vs T (right) plots for complexes **$F^1$** obtained 1000 G; filled circles represent experimental data that is well-modeled by the magnetic simulation (red line). Open black circles are experimental data that deviates from the simulation.

### B.2.2 $[Co_2(\mu\text{-}F)_2(pnN_4\text{-}PhCl)_2](BF_4)_2$ ($F^2$)

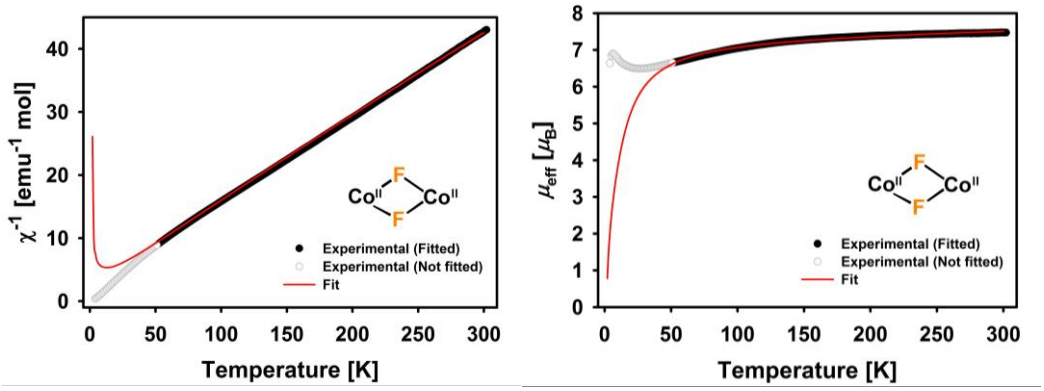


Figure B.5: The reciprocal χ vs T (left) and $\mu_{eff}$ vs T (right) plots for complexes $\mathbf{F^2}$ obtained 1000 G; filled circles represent experimental data that is well-modeled by the magnetic simulation (red line). Open black circles are experimental data that deviates from the simulation.

## B.3 Chapter 5 Spectrum

### B.3.1 $[Mn(Thianth\text{-}S_2)(CO)_3Br]$ (Mn-Thianth-$S_2$)

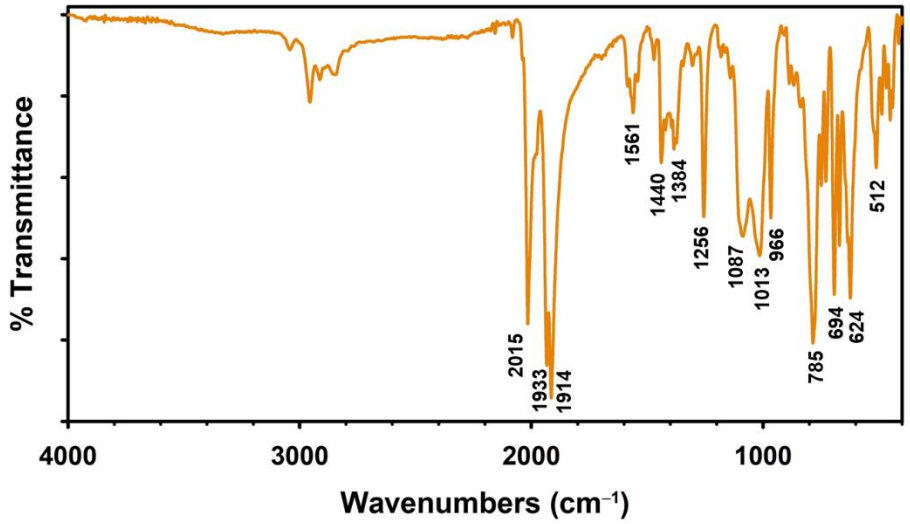


Figure B.6: Infrared spectrum of **Mn-Thianth-$S_2$**.

# Appendix C: Crystal Data and Refinement Parameters

## C.1 Chapter 2 structures

| | **1(BF$_4$)$_3$**<br>$\mu$-OH,$\mu$-O$_2$-[Co(enN$_4$)]$_2$<br>(BF$_4$)$_3$·2MeCN·H$_2$O | **1(ClO$_4$)$_3$**<br>$\mu$-OH,$\mu$-O$_2$-[Co(enN$_4$)]$_2$<br>(ClO$_4$)$_3$·2MeCN·H$_2$O | **1(PF$_6$)$_3$**<br>$\mu$-OH,$\mu$-O$_2$-[Co(enN$_4$)]$_2$<br>(PF$_6$)$_3$·2MeCN·H$_2$O |
|---|---|---|---|
| formula | $C_{32}H_{35.67}B_3Co_2F_{12}N_{10}O_{3.34}$ | $C_{32}H_{37}Cl_3Co_2N_{10}O_{16}$ | $C_{32}H_{86}Co_2F_5N_{21}O_{18}P_{12}$ |
| FW | 992.02 | 1041.93 | 1637.71 |
| color | Black | Black | Black |
| habit | Parallelepiped | Parallelepiped | Needles |
| size (mm) | 0.48 × 0.26 × 0.21 | 0.26 × 0.16 × 0.12 | 0.32 × 0.15 × 0.08 |
| $T$ (K) | 153(2) | 153(2) | 100(2) |
| λ (Å) | 0.71073 | 0.71075 | 1.54184 |
| lattice | Triclinic | Triclinic | Monoclinic |
| space group | $P\bar{1}$ | $P\bar{1}$ | $P\,2_1/c$ |
| $a$ (Å) | 10.372(2) | 10.4878(12) | 13.6014(3) |
| $b$ (Å) | 13.560(2) | 13.613(2) | 37.0347(6) |
| $c$ (Å) | 16.459(3) | 16.729(2) | 18.1234(3) |
| $\alpha$ (deg) | 75.856(3) | 75.920(3) | 90 |
| $\beta$ (deg) | 73.453(4) | 73.078(2) | 102.633(2) |
| $\gamma$ (deg) | 68.595(3) | 68.687(2) | 90 |
| $V$ (Å$^3$) | 2040.2(6) | 2103.2(5) | 8908.2(3) |
| $Z$ | 2 | 2 | 4 |
| $d_{calc}$ (g/cm$^3$) | 1.615 | 1.645 | 1.221 |
| $\mu$ (mm$^{-1}$) | 0.917 | 1.061 | 5.563 |
| GOF on $F^2$ | 1.163 | 1.084 | 1.027 |
| $R$ indices<br>[$I>2\sigma(I)$] | R1 = 0.0634<br>$w$R2 = 0.1672 | R1 = 0.0455<br>$w$R2 = 0.1078 | R1 = 0.0656<br>$w$R2 = 0.1708 |
| $R$ indices<br>all data | R1 = 0.0743<br>$w$R2 = 0.1761 | R1 = 0.0521<br>$w$R2 = 0.1113 | R1 = 0.0865<br>$w$R2 = 0.1894 |

Table C.1: Crystal data and refinement parameters for **1(BF$_4$)$_3$**, **1(ClO$_4$)$_3$** and **1(PF$_6$)$_3$**.

## C.2 CHAPTER 3 STRUCTURES

| | **F¹** $[Co_2(\mu\text{-}F)(pnN_4\text{-}PhCl)_2(OH_2)(MeCN)](BF_4)_3$ | **F²** $[Co_2(\mu\text{-}F)_2(pnN_4\text{-}PhCl)_2](BF_4)_2$ | **3** $[Co_2(pnN_4)_3](BF_4)_4\cdot(MeCN)_3\cdot(H_2O)$ | **4** $[Co(py)_4(MeCN)_2](BF_4)_2$ | **5(ClO₄)₂** $[Co(pnN_3\text{-}OMe^*)_2](ClO_4)_2$ |
|---|---|---|---|---|---|
| formula | $C_{60}H_{55}B_3Cl_4Co_2F_{13}N_{11}O$ | $C_{27}H_{22}BCl_2CoF_5N_4$ | $C_{51}H_{57}B_4Co_2F_{16}N_{15}O$ | $C_{24}H_{26}B_2CoF_8N_6$ | $C_{20}H_{30}Cl_2CoN_6O_{10}$ |
| FW | 1485.24 | 638.12 | 1363.23 | 631.06 | 644.33 |
| color | Reddish pink | Reddish pink | Red | Pink | Reddish pink |
| habit | Parallelepiped | Parallelepiped | Needles | Hexagon | Needles |
| size (mm) | 0.56 × 0.46 × 0.32 | 0.15 × 0.08 × 0.07 | 0.19 × 0.16 × 0.14 | 0.43 × 0.39 × 0.35 | 0.54 × 0.19 × 0.16 |
| $T$ (K) | 100(2) | 100(2) | 100(2) | 100(2) | 100(2) |
| λ (Å) | 0.71073 | 0.71073 | 0.71073 | 0.71073 | 0.71073 |
| lattice | Monoclinic | Orthorhombic | Monoclinic | Cubic | Monoclinic |
| space group | $C$ 2/c | $P$ $2_12_12$ | $I$ m | $P$ $n\bar{3}n$ | $P$ $2_1/c$ |
| $a$ (Å) | 23.665(2) | 14.8605(15) | 10.700(2) | 16.3992(7) | 9.9009(5) |
| $b$ (Å) | 14.6648(13) | 21.329(2) | 16.893(4) | 16.3992(7) | 17.9640(8) |
| $c$ (Å) | 18.7222(17) | 8.3041(10) | 17.361(4) | 16.3992(7) | 15.9921(9) |
| $\alpha$ (deg) | 90.000 | 90.000 | 90.000 | 90.000 | 90.000 |
| $\beta$ (deg) | 102.917(3) | 90.000 | 98.845(6) | 90.000 | 105.467(2) |
| $\gamma$ (deg) | 90.000 | 90.000 | 90.000 | 90.000 | 90.000 |
| $V$ (Å$^3$) | 6332.9(10) | 2632.1(5) | 3100.8(12) | 4410.3(6) | 2741.3(2) |
| $Z$ | 4 | 4 | 2 | 6 | 4 |
| $d_{calc}$ (g/cm$^3$) | 1.558 | 1.61 | 1.460 | 1.426 | 1.561 |
| $\mu$ (mm$^{-1}$) | 0.783 | 0.917 | 0.633 | 0.659 | 0.884 |
| GOF on $F^2$ | 1.073 | 1.098 | 1.046 | 1.189 | 1.010 |
| $R$ indices $[I>2\sigma(I)]$ | R1 = 0.0452<br>$w$R2 = 0.1089 | R1 = 0.064<br>$w$R2 = 0.116 | R1 = 0.0550<br>$w$R2 = 0.1101 | R1 = 0.125<br>$w$R2 = 0.389 | R1 = 0.0355<br>$w$R2 = 0.0746 |
| $R$ indices all data | R1 = 0.0521<br>$w$R2 = 0.1124 | R1 = 0.078<br>$w$R2 = 0.121 | R1 = 0.0738<br>$w$R2 = 0.1203 | R1 = 0.136<br>$w$R2 = 0.396 | R1 = 0.0568<br>$w$R2 = 0.0855 |

Table C.2: Crystal data and refinement parameters for **F¹**, **F²**, **3**, **4** and **5(ClO₄)₂**. *: hydrolyzed **pnN₄-OMe** ligand.

## C.3 CHAPTER 4 STRUCTURES

| | **Fe-CNS** [Fe(CNS)(CO)$_2$I] | **Fe-CNP** [Fe(CNP)(CO)$_2$I] | **CNP** $CH_3C_5H_3NC_6H_4P(C_5H_5)_2$ |
|---|---|---|---|
| formula | $C_{16}H_{12}FeINO_3S$ | $C_{27}H_{19}FeINO_3P$ | $C_{24}H_{20}NP$ |
| FW | 481.08 | 619.15 | 353.38 |
| color | Red | Orange | Colorless |
| habit | Block/Needles | Clusters | Prism |
| size (mm) | 0.10 × 0.08 × 0.05 | 0.11 × 0.06 × 0.06 | 0.23 × 0.11 × 0.09 |
| *T* (K) | 153(2) | 173(2) | 100(2) |
| λ (Å) | 0.71073 | 1.54184 | 0.71073 |
| lattice | Orthorhombic | Triclinic | Monoclinic |
| space group | $P\,2_12_12_1$ | *P* -1 | *C 2/c* |
| *a* (Å) | 7.2977(6) | 10.6272(14) | 18.569(3) |
| *b* (Å) | 10.7837(8) | 10.846(2) | 11.9238(18) |
| *c* (Å) | 20.6626(16) | 12.1679(18) | 17.980(3) |
| *α* (deg) | 90.00 | 66.269(16) | 90 |
| *β* (deg) | 90.00 | 72.377(12) | 112.260(3) |
| *γ* (deg) | 90.00 | 79.914(14) | 90 |
| *V* (Å$^3$) | 1626.1(2) | 1221.4(4) | 3684.2(10) |
| *Z* | 4 | 2 | 8 |
| $d_{calc}$ (g/cm$^3$) | 1.965 | 1.683 | 1.274 |
| *μ* (mm$^{-1}$) | 2.967 | 15.736 | 0.156 |
| GOF on $F^2$ | 1.151 | 1.039 | 1.056 |
| *R* indices [$I>2\sigma(I)$] | R1 = 0.0201<br>*w*R2 = 0.0424 | R1 = 0.0930<br>*w*R2 = 0.2335 | R1 = 0.0386<br>*w*R2 = 0.1001 |
| *R* indices all data | R1 = 0.0210<br>*w*R2 = 0.0426 | R1 = 0.1049<br>*w*R2 = 0.2414 | R1 = 0.0453<br>*w*R2 = 0.1059 |

Table C.3: Crystal data and refinement parameters for **Fe-CNS, Fe-CNP** and **CNP**.

## References


(1) Winter, C.-J. *Int. J. Hydrogen Energy* **2009**, *34* (14), S1–S52.

(2) Shima, S.; Thauer, R. K. *Chem. Rec.* **2007**, *7* (1), 37–46.

(3) Kubas, G. J. *Acc. Chem. Res.* **1988**, *21* (3), 120–128.

(4) Blaser, H.-U.; Malan, C.; Pugin, B.; Spindler, F.; Steiner, H.; Studer, M. *Adv. Synth. Catal.* **2003**, *345* (1+2), 103–151.

(5) Morris, R. H. *Chem. Soc. Rev.* **2009**, *38* (8), 2282.

(6) Hefner, R. A. *Int. J. Hydrogen Energy* **2002**, *27* (1), 1–9.

(7) Kubas, G. J. *Chem. Rev.* **2007**, *107* (10), 4152–4205.

(8) Sordakis, K.; Tang, C.; Vogt, L. K.; Junge, H.; Dyson, P. J.; Beller, M.; Laurenczy, G. *Chem. Rev.* **2018**, *118* (2), 372–433.

(9) He, T.; Pachfule, P.; Wu, H.; Xu, Q.; Chen, P. *Nat. Rev. Mater.* **2016**, *1* (12).

(10) Li, H. W.; Yan, Y.; Orimo, S. I.; Züttel, A.; Jensen, C. M. *Energies* **2011**, *4* (1), 185–214.

(11) Zhu, Q.-L.; Xu, Q. *Energy Environ. Sci.* **2015**, *8* (2), 478–512.

(12) Klerke, A.; Christensen, C. H.; Nørskov, J. K.; Vegge, T. *J. Mater. Chem.* **2008**, *18* (20), 2304.

(13) Moury, R.; Moussa, G.; Demirci, U. B.; Hannauer, J.; Bernard, S.; Petit, E.; van der Lee, A.; Miele, P. *Phys. Chem. Chem. Phys.* **2012**, *14* (5), 1768–1777.

(14) Peng, B.; Chen, J. *Energy Environ. Sci.* **2008**, 479–483.

(15) Grasemann, M.; Laurenczy, G. *Energy Environ. Sci.* **2012**, *5* (8), 8171.

(16) Mellmann, D.; Sponholz, P.; Junge, H.; Beller, M. *Chem. Soc. Rev.* **2016**, *45* (14), 3954–3988.

(17) Eppinger, J.; Huang, K.-W. *ACS Energy Lett.* **2017**, *2* (1), 188–195.

(18) Johnson, T. C.; Morris, D. J.; Wills, M. *Chem. Soc. Rev.* **2010**, *39* (1), 81–88.

(19) Tai, C.-C.; Chang, T.; Roller, B.; Jessop, P. G. *Inorg. Chem.* **2003**, *42* (23), 7340–7341.

(20) Federsel, C.; Boddien, A.; Jackstell, R.; Jennerjahn, R.; Dyson, P. J.; Scopelliti, R.; Laurenczy, G.; Beller, M. *Angew. Chemie - Int. Ed.* **2010**, *49* (50), 9777–9780.

(21) Badiei, Y. M.; Wang, W. H.; Hull, J. F.; Szalda, D. J.; Muckerman, J. T.; Himeda, Y.; Fujita, E. *Inorg. Chem.* **2013**, *52* (21), 12576–12586.

(22) Watari, R.; Kayaki, Y.; Hirano, S. I.; Matsumoto, N.; Ikariya, T. *Adv. Synth. Catal.* **2015**, *357* (7), 1369–1373.

(23) Brunner, H.; Zettlmeier, W. *Handbook of enantioselective catalysis with transition metal compounds, Volumes 1-2*; VCH, 1993: the Unversity of Michigan, 1993.

(24) Brown, J. M. In *Comprehensive Asymmetric Catalysis*; Jacobson, E. N., Pfaltz, A., Yamamoto, H., Eds.; Springer: Berlin, 1999; p 121.

(25) Ohkuma, T., Kitamura, M., Noyori, R. In *Catalytic Asymmetric Synthesis*; Ojima, I., Ed.; Wiley-VCH: New York, 2000; p 1.

(26) Ye, G.; Gong, Y.; Lin, J.; Li, B.; He, Y.; Pantelides, S. T.; Zhou, W.; Vajtai, R.; Ajayan, P. M. *Nano Lett.* **2016**, *16* (2), 1097–1103.

(27) Tian, L.; Yan, X.; Chen, X. *ACS Catal.* **2016**, *6* (8), 5441–5448.

(28) Hou, R.; Chang, K.; Chen, J. G.; Wang, T. *Top. Catal.* **2015**, *58*, 240–246.

(29) Zahedi, R.; Taromi, F. A.; Mirjahanmardi, S. H.; Haghighi, M. N.; Jadidi, K.; Jamjah, R. *Adv. Polym. Technol.* **2016**, *37* (1), 144–153.

(30) Sampson, M. D.; Kubiak, C. P. *J. Am. Chem. Soc.* **2016**, *138* (4), 1386–1393.

(31) Xu, J. D.; Chang, Z. Y.; Zhu, K. T.; Weng, X. F.; Weng, W. Z.; Zheng, Y. P.; Huang, C. J.; Wan, H. L. *Appl. Catal. A Gen.* **2016**, *514*, 103–113.

(32) Le Roux, E.; De Mallmann, A.; Merle, N.; Taoufik, M.; Anwander, R. *Organometallics* **2015**, *34* (20), 5146–5154.

(33) Spatzal, T.; Aksoyoglu, M.; Zhang, L.; Andrade, S. L. A.; Schleicher, E.; Weber, S.; Rees, D. C.; Einsle, O. *Science* **2011**, *334* (6058), 940–940.

(34) Happe, T.; Hemschemeier, A. *Trends Biotechnol.* **2014**, *32* (4), 170–176.

(35) Proskurowski, G.; Lilley, M. D.; Seewald, J. S.; Früh-Green, G. L.; Olson, E. J.;

Lupton, J. E.; Sylva, S. P.; Proskurowski, D. S. K.; Kelley, D. S. *Science* **2008**, *319* (2008), 319–607.

(36) Takai, K.; Gamo, T.; Tsunogai, U.; Nakayama, N.; Hirayama, H.; Nealson, K. H.; Horikoshi, K. *Extremophiles* **2004**, *8* (4), 269–282.

(37) Tian, F.; Toon, O. B.; Pavlov, A. A.; De Sterck, H. *Science* **2005**, *308* (5724), 1014–1017.

(38) Wachtershauser, G. *Proc. Natl. Acad. Sci.* **1990**, *87* (1), 200–204.

(39) Vignais, P. M.; Billoud, B.; Meyer, J. *Anal. Biochem.* **1994**, *217* (2), 220–230.

(40) Vignais, P. M.; Billoud, B. *Chem. Rev.* **2007**, *107* (10), 4206–4272.

(41) Tamagnini, P.; Axelsson, R.; Lindberg, P.; Oxelfelt, F.; Wünschiers, R.; Lindblad, P. *Microbiol. Mol. Biol. Rev.* **2002**, *66* (1), 1–20.

(42) Tamagnini, P.; Leitão, E.; Oliveira, P.; Ferreira, D.; Pinto, F.; Harris, D. J.; Heidorn, T.; Lindblad, P. *FEMS Microbiol. Rev.* **2007**, *31* (6), 692–720.

(43) Fontecilla-Camps, J. C.; Volbeda, A.; Cavazza, C.; Nicolet, Y. *Chem. Rev.* **2007**, *107* (10), 4273–4303.

(44) Volbeda, A.; Charon, M.-H.; Piras, C.; Hatchikian, E. C.; Frey, M.; Fontecilla-Camps, J. C. *Nature*. 1995, pp 580–587.

(45) Higuchi, Y.; Yagi, T.; Yasuoka, N. *Structure* **1997**, *5* (2), 1671–1680.

(46) Montet, Y.; Amara, P.; Volbeda, A.; Vernede, X.; Hatchikian, E. C.; Field, M. J.; Frey, M.; Fontecilla-Camps, J. C. *Nat. Struct. Biol.* **1997**, *4* (7), 523–526.

(47) Garcin, E.; Vernede, X.; Hatchikian, E. C.; Volbeda, A.; Frey, M.; Fontecilla-Camps, J. C. *Structure* **1999**, *7* (5), 557–566.

(48) Matias, P. M.; Soares, C. M.; Saraiva, L. M.; Coelho, R.; Morais, J.; Le Gall, J.; Carrondo, M. A. *J. Biol. Inorg. Chem.* **2001**, *6* (1), 63–81.

(49) Nicolet, Y.; Piras, C.; Legrand, P.; Hatchikian, C. E.; Fontecilla-Camps, J. C. *Structure* **1999**, *7* (1), 13–23.

(50) Peters, J. W.; Lanzilotta, W. N.; Lemon, B. J.; Seefeldt, L. C. *Science* **1998**, *282* (5395), 1853–1858.

(51) Lubitz, W.; Ogata, H.; Rüdiger, O.; Reijerse, E. *Chem. Rev.* **2014**, *114* (8), 4081–

4148.

(52) Afting, C.; Hochheimer, A.; Thauer, R. K. *Arch. Microbiol.* **1998**, *169* (3), 206–210.

(53) Zirngibl, C.; van Dongen, W.; Schwörer, B.; von Bünau, R.; Richter, M.; Klein, A.; Thauer, R. K. *Eur. J. Biochem.* **1992**, *208*, 511–520.

(54) Buurman, G.; Shima, S.; Thauer, R. K. *FEBS Lett.* **2000**, *485* (2–3), 200–204.

(55) Lyon, E. J.; Shima, S.; Buurman, G.; Chowdhuri, S.; Batschauer, A.; Steinbach, K.; Thauer, R. K. *Eur. J. Biochem.* **2004**, *271* (1), 195–204.

(56) Shima, S.; Lyon, E. J.; Thauer, R. K.; Mienert, B.; Bill, E. *J. Am. Chem. Soc.* **2005**, *127* (29), 10430–10435.

(57) Shima, S.; Pilak, O.; Vogt, S.; Schick, M.; Stagni, M. S.; Meyer-Klaucke, W.; Warkentin, E.; Thauer, R. K.; Ermler, U. *Science* **2008**, *321*, 572–575.

(58) Hiromoto, T.; Ataka, K.; Pilak, O.; Vogt, S.; Stagni, M. S.; Meyer-Klaucke, W.; Warkentin, E.; Thauer, R. K.; Shima, S.; Ermler, U. *FEBS Lett.* **2009**, *583* (3), 585–590.

(59) Hiromoto, T.; Warkentin, E.; Moll, J.; Ermler, U.; Shima, S. *Angew. Chemie - Int. Ed.* **2009**, *48* (35), 6457–6460.

(60) Lyon, E. J.; Shima, S.; Boecher, R.; Thauer, R. K.; Grevels, F.-W.; Bill, E.; Roseboom, W.; Albracht, S. P. J. *J. Am. Chem. Soc.* **2004**, *126* (43), 14239–14248.

(61) Shima, S.; Lyon, E. J.; Sordel-Klippert, M.; Kauß, M.; Kahnt, J.; Thauer, R. K.; Steinbach, K.; Xie, X.; Verdier, L.; Griesinger, C. *Angew. Chemie - Int. Ed.* **2004**, *43* (19), 2547–2551.

(62) Korbas, M.; Vogt, S.; Meyer-Klaucke, W.; Bill, E.; Lyon, E. J.; Thauer, R. K.; Shima, S. *J. Biol. Chem.* **2006**, *281* (41), 30804–30813.

(63) Pilak, O.; Mamat, B.; Vogt, S.; Hagemeier, C. H.; Thauer, R. K.; Shima, S.; Vonrhein, C.; Warkentin, E.; Ermler, U. *J. Mol. Biol.* **2006**, *358* (3), 798–809.

(64) Svetlitchnyi, V.; Dobbek, H.; Meyer-Klaucke, W.; Meins, T.; Thiele, B.; Römer, P.; Huber, R.; Meyer, O. *Proc. Natl. Acad. Sci. U. S. A.* **2004**, *101* (2), 446–451.

(65) Ragsdale, S. W. *J. Inorg. Biochem.* **2007**, *101* (11–12), 1657–1666.

(66) Schrauzer, G. N.; Lee, L. P. *J. Am. Chem. Soc.* **1970**, *92* (6), 1551–1557.

(67) Schrauzer, G. N.; Parshall, G. W.; Wonchoba, E. R. In *Inorganic Synthesis*; Jolly, W. L., Ed.; 1968; Vol. XI, pp 61–70.

(68) Toscano, P. J.; Marzilli, L. G. In *Progress in Inorganic Chemistry*; Lippard, S. J., Ed.; John Wiley & Sons, Inc., 1984; pp 105–204.

(69) Tsumaki, T. *Bull. Chem. Soc. Jpn.* **1938**, *13* (2), 252–260.

(70) Cho, Y. I.; Joseph, D. M.; Rose, M. J. *Inorg. Chem.* **2013**, *52* (23), 13298–13300.

(71) Cho, Y. I.; Ward, M. L.; Rose, M. J. *Dalt. Trans.* **2016**, *45* (34), 13466–13476.

(72) Bauer, G.; Hu, X. *Inorg. Chem. Front.* **2016**, *3* (6), 741–765.

(73) Lawrence, M. A. W.; Green, K. A.; Nelson, P. N.; Lorraine, S. C. *Polyhedron* **2017**, *143*, 11–27.

(74) Albrecht, M.; Van Koten, G. *Angew. Chemie - Int. Ed.* **2001**, *40* (20), 3750–3781.

(75) Zhang, J.; Gandelman, M.; Herrman, D.; Leitus, G.; Shimon, L. J. W.; Ben-David, Y.; Milstein, D. *Inorganica Chim. Acta* **2006**, *359* (6), 1955–1960.

(76) Langer, R.; Leitus, G.; Ben-David, Y.; Milstein, D. *Angew. Chemie - Int. Ed.* **2011**, *50* (9), 2120–2124.

(77) Zell, T.; Ben-David, Y.; Milstein, D. *Angew. Chemie - Int. Ed.* **2014**, *53* (18), 4685–4689.

(78) Rivada-Wheelaghan, O.; Dauth, A.; Leitus, G.; Diskin-Posner, Y.; Milstein, D. *Inorg. Chem.* **2015**, *54* (9), 4526–4538.

(79) Zell, T.; Milstein, D. *Acc. Chem. Res.* **2015**, *48*, 1979–1994.

(80) Butschke, B.; Feller, M.; Diskin-Posner, Y.; Milstein, D. *Catal. Sci. Technol.* **2016**, *6* (12), 4428–4437.

(81) Garg, J. A.; Chakraborty, S.; Ben-David, Y.; Milstein, D. *Chem. Commun.* **2016**, *52* (30), 5285–5288.

(82) Bauer, G.; Kirchner, K. A. *Angew. Chemie - Int. Ed.* **2011**, *50* (26), 5798–5800.

(83) Bichler, B.; Holzhacker, C.; Stöger, B.; Puchberger, M.; Veiros, L. F.; Kirchner, K. A. *Organometallics* **2013**, *32* (15), 4114–4121.

(84) Gorgas, N.; Stöger, B.; Veiros, L. F.; Pittenauer, E.; Allmaier, G.; Kirchner, K. A.

*Organometallics* **2014**, *33*, 6905–6914.

(85) Bichler, B.; Glatz, M.; Stöger, B.; Mereiter, K.; Veiros, L. F.; Kirchner, K. A. *Dalt. Trans.* **2014**, *43* (39), 14517–14519.

(86) Song, L.-C.; Xie, Z.-J.; Wang, M.-M.; Zhao, G.-Y.; Song, H.-B. *Inorg. Chem.* **2012**, *51* (14), 7466–7468.

(87) Song, L.-C.; Hu, F.-Q.; Zhao, G.-Y.; Zhang, J.-W.; Zhang, W.-W. *Organometallics* **2014**, *33* (22), 6614–6622.

(88) Chen, D.; Scopelliti, R.; Hu, X. *Angew. Chemie - Int. Ed.* **2010**, *49* (41), 7512–7515.

(89) Fischer, E. O.; Maasböl, A. *Angew. Chemie - Int. Ed.* **1964**, *3* (8), 580–581.

(90) Manes, T. A.; Rose, M. J. *Coord. Chem. Rev.* **2017**, *353*, 295–308.

(91) Zhou, J.; Hu, Z.; Münck, E.; Holm, R. H. *J. Am. Chem. Soc.* **1996**, *118* (8), 1966–1980.

(92) Li, Y.; Cao, R.; Lippard, S. J. *Org. Lett.* **2011**, *13* (19), 5052–5055.

(93) Grossman, O.; Azerraf, C.; Gelman, D. *Organometallics* **2006**, *25* (2), 375–381.

(94) Kaganovsky, L.; Gelman, D.; Rueck-Braun, K. *J. Organomet. Chem.* **2010**, *695* (2), 260–266.

(95) Marlier, E. E.; Tereniak, S. J.; Ding, K.; Mulliken, J. E.; Lu, C. C. *Inorg. Chem.* **2011**, *50* (19), 9290–9299.

(96) Ding, K.; Miller, D. L.; Young, V. G.; Lu, C. C. *Inorg. Chem.* **2011**, *50* (6), 2545–2552.

(97) van Leeuwen, P. W. N. M.; Kamer, P. C. J.; Reek, J. N. H. *Pure Appl. Chem.* **1999**, *71* (8), 1443–1452.

(98) Dierkes, P.; van Leeuwen, P. W. N. M. *J. Chem. Soc. Dalt. Trans.* **1999**, 1519–1529.

(99) Freixa, Z.; van Leeuwen, P. W. N. M. *Dalt. Trans.* **2003**, *77*, 1890.

(100) Manes, T. A.; Rose, M. J. *Inorg. Chem.* **2016**, *55* (11), 5127–5138.

(101) Seo, J.; Manes, T. A.; Rose, M. J. *Nat. Chem.* **2017**, *9*, 552–557.

(102) Kerns, S. A.; Magtaan, A.-C.; Vong, P. R.; Rose, M. J. *Angew. Chemie Int. Ed.* **2018**, *57*, 2855–2858.

(103) Hoffman, B. M.; Petering, D. H. *Proc. Natl. Acad. Sci.* **1970**, *67* (2), 637–643.

(104) Fremy, E. *Ann. der Chemie und Pharm.* **1852**, *83* (2), 227–249.

(105) Gibbs, W. *Proc. Am. Acad. Arts Sci.* **1876**, *11*, 1–51.

(106) Vortmann, G.; Verbindungen, D. **1885**, 404–445.

(107) Vortmann, G. *Berichte der Dtsch. Chem. Gesellschaft* **1877**, *10* (2), 1451–1459.

(108) Vortmann, G. *Berichte der Dtsch. Chem. Gesellschaft* **1882**, *15* (2), 1890–1903.

(109) Vortmann, G.; Blasberg, O. *Berichte der Dtsch. Chem. Gesellschaft* **1889**, *22* (2), 2648–2655.

(110) Jörgensen, S. M. *J. für Prakt. Chemie* **1885**, *31* (1), 49–93.

(111) Jörgensen, S. M. *Zeitschrift für Anorg. Chemie* **1894**, *5* (1), 147–196.

(112) Jörgensen, S. M. *Zeitschrift für Anorg. Chemie* **1898**, *17* (1), 455–479.

(113) Maquenne, L. *Comptes Rendus* **1883**, *96*, 344.

(114) Mascetti, E. *Zeitschrift für Anorg. Chemie* **1900**, *24* (1), 188–190.

(115) Werner, A. *Justus Liebig's Ann. der Chemie* **1910**, *375* (1), 1–144.

(116) Werner, A.; Mylius, A. *Zeitschrift für Anorg. Chemie* **1898**, *16* (1), 245–267.

(117) Spingler, B.; Scanavy-Grigorieff, M.; Werner, A.; Berke, H.; Lippard, S. J. *Inorg. Chem.* **2001**, *40*, 1065–1066.

(118) Bianchini, C.; Zoellner, R. W. *Adv. Inorg. Chem.* **1996**, *44*, 263–339.

(119) Sykes, A. G.; Weil, J. A. In *Progress in Inorganic Chemistry*; Edwards, J. O., Ed.; John Wiley & Sons, Inc.: Hoboken, NJ, USA, 1970; Vol. 13, pp 1–106.

(120) Simplicio, J.; Wilkins, R. G. *J. Am. Chem. Soc.* **1969**, *91* (6), 1325–1329.

(121) Mori, M.; Weil, J. a.; Ishiguro, M. *J. Am. Chem. Soc.* **1968**, *90* (3), 615–621.

(122) *Tables of Interatomic Distances, The Chemical Society (London) Special Publication No. 11*; 1958.

(123) Halverson, F. *J. Phys. Chem. Solids* **1962**, *23* (3), 207–214.

(124) Bogucki, R. F.; McLendon, G.; Martell, A. E. *J. Am. Chem. Soc.* **1976**, *98* (11), 3202–3205.

(125) Vad, M. S.; Johansson, F. B.; Seidler-Egdal, R. K.; McGrady, J. E.; Novikov, S. M.; Bozhevolnyi, S. I.; Bond, A. D.; McKenzie, C. J. *Dalt. Trans.* **2013**, *42* (27), 9921–9929.

(126) Calligaris, M.; Nardin, G.; Randaccio, L.; Ripamonti, A. *J. Chem. Soc. A Inorganic, Phys. Theor.* **1970**, *0*, 1069–1074.

(127) Fallab, S. *Angew. Chemie Int. Ed. English* **1967**, *6* (6), 496–507.

(128) Calligaris, M.; Nardin, G.; Randaccio, L. *J. Chem. Soc. D Chem. Commun.* **1969**, *0*, 763–764.

(129) Floriani, C.; Calderazzo, F. *J. Chem. Soc. A Inorganic, Phys. Theor.* **1969**, *0*, 946–953.

(130) Bekâroğlu, O.; Fallab, S. *Helv. Chim. Acta* **1963**, *46* (6), 2120–2125.

(131) Ludovici, C.; Fröhlich, R.; Vogtt, K.; Mamat, B.; Lübben, M. *Eur. J. Biochem.* **2002**, *269* (10), 2630–2637.

(132) MacArthur, R.; Sucheta, A.; Chongt, F. F. S.; Einarsdottir, O. E. *Proc. Natl. Acad. Sci.* **1995**, *92* (August), 8105–8109.

(133) Wasylenko, D. J.; Palmer, R. D.; Schott, E.; Berlinguette, C. P. *Chem. Commun.* **2012**, *48* (15), 2107.

(134) Wasylenko, D. J.; Ganesamoorthy, C.; Borau-Garcia, J.; Berlinguette, C. P. *Chem. Commun.* **2011**, *47* (14), 4249.

(135) Askarizadeh, E.; Yaghoob, S. B.; Boghaei, D. M.; Slawin, A. M. Z.; Love, J. B. *Chem. Commun.* **2010**, *46* (5), 710–712.

(136) Givaja, G.; Volpe, M.; Edwards, M. A.; Blake, A. J.; Wilson, C.; Schröder, M.; Love, J. B. *Angew. Chemie Int. Ed.* **2007**, *46* (4), 584–586.

(137) McAlpin, J. G.; Surendranath, Y.; Dincă, M.; Stich, T. A.; Stoian, S. A.; Casey, W. H.; Nocera, D. G.; Britt, R. D. *J. Am. Chem. Soc.* **2010**, *132* (20), 6882–6883.

(138) Surendranath, Y.; Kanan, M. W.; Nocera, D. G. *J. Am. Chem. Soc.* **2010**, *132* (46), 16501–16509.

(139) Zehnder, M.; Thewalt, U.; Fallab, S. *Helv. Chim. Acta* **1976**, *59* (6), 2290–2294.

(140) Thewalt, U.; Struckmeier, G. *Zeitschrift für Anorg. und Allg. Chemie* **1976**, *419* (2), 163–170.

(141) Fallab, S.; Zehnder, M.; Thewalt, U. *Helv. Chim. Acta* **1980**, *63* (6), 1491–1498.

(142) Mäcke, H.; Zehnder, M.; Thewalt, U.; Fallab, S. *Helv. Chim. Acta* **1979**, *62* (6), 1804–1815.

(143) Banerjee, S.; Gangopadhyay, J.; Lu, C.-Z.; Chen, J.-T.; Ghosh, A. *Eur. J. Inorg. Chem.* **2004**, *2004* (12), 2533–2541.

(144) *Crystal Clear 1.40* (**2008**). Rigaku Americas Corportion, The Woodlands, TX.

(145) Altomare, A.; Burla, M. C.; Camalli, M.; Cascarano, G. L.; Giacovazzo, C.; Guagliardi, A.; Moliterni, A. G. G.; Polidori, G.; Spagna, R. *SIR97*, A program for crystal structure solution. *J. Appl. Cryst.* **1999**, *32*, 115-119.

(146) Sheldrick, G. M. *SHELXL97,* Program for the Refinement of Crystal Structures. *Acta Cryst*. **2008**, *A64*, 112-122.

(147) Spek, A. L. *PLATON*, A Multipurpose Crystallographic Tool, Utrecht University, Utrecht, The Netherlands. *Acta Cryst.* **2009**, *D65*, 148-155.

(148) Farrugia, L. J. *WinGX* 1.64. An Integrated System of Windows Programs for the Solution, Refinement and Analysis of Single Crystal X-ray Diffraction Data. *J. Appl. Cryst.* **1999***, 32*, 837-838.

(149) International Tables for X-ray Crystallography (**1992**). Vol. C, Tables 4.2.6.8 and 6.1.1.4, Wilson, A. J. C., Boston: Kluwer Academic Press.

(150) *CrysAlisPro V 1.171.38.43f* (**2013**), Agilent Technologies.

(151) Sheldrick, G. M. *SHELXT,* An Integrated Space Group and Crystal Structure Determination Program. *Acta Cryst.* **2015**, *A71*, 3-8.

(152) Sheldrick, G. M. *SHELXL-2016/6*. *Acta Cryst.* **2015**, *C71*, 9-18.

(153) Rietmeijer, F. J.; van Albada, G. A.; de Graaff, R. A. G.; Haasnoot, J. G.; Reedijk, J. *Inorg. Chem.* **1985**, *24* (d), 3597–3601.

(154) Rietmeijer, F. J.; Haasnoot, J. G.; Den Hartog, A. J.; Reedijk, J. *Inorg. Chim. Acta* **1986**, *113*, 147–155.

(155) Reger, D. L.; Pascui, A. E.; Smith, M. D.; Jezierska, J.; Ozarowski, A. *Inorg. Chem.* **2012**, *51* (Ii), 11820–11836.

(156) Meyer, F.; Heinze, K.; Nuber, B.; Zsolnai, L. *J. Chem. Soc. Dalt. Trans.* **1998**, No. 3, 207–213.

(157) Reedijk, J.; Jansen, J. C.; van Koningsveld, H.; van Kralingen, C. G. *Inorg. Chem.* **1978**, *17* (7), 1990–1994.

(158) Dugan, T. R.; Sun, X.; Rybak-akimova, E. V; Olatunji-ojo, O.; Cundari, T. R.; Holland, P. L. *J. Am. Chem. Soc.* **2011**, *291* (I), 12418–12421.

(159) Gobeze, W. A.; Milway, V. A.; Moubaraki, B.; Murray, K. S.; Brooker, S. *Dalt. Trans.* **2012**, *41* (32), 9708.

(160) Gobeze, W. A.; Milway, V. A.; Chilton, N. F.; Moubaraki, B.; Murray, K. S.; Brooker, S. *Eur. J. Inorg. Chem.* **2013**, *2013* (25), 4485–4498.

(161) Inomata, M.; Suenaga, Y. *Acta Crystallogr. Sect. E Struct. Reports Online* **2014**, *70* (ii), m359–m360.

(162) Tomat, E.; Cuesta, L.; Lynch, V. M.; Sessler, J. L. *Inorg. Chem.* **2007**, *46* (16), 6224–6226.

(163) Musgrave, T. R.; Lin, T. S. *J. Coord. Chem.* **1973**, *2* (4), 323–324.

(164) Guichelaar, M. A.; van Hest, J. A. M.; Reedijk, J. *Inorg. Nucl. Chem. Lett.* **1974**, *10* (11), 999–1004.

(165) Reger, D. L.; Foley, E. a; Watson, R. P.; Pellechia, P. J.; Smith, M. D.; Grandjean, F.; Long, G. J. *Inorg. Chem.* **2009**, *48* (22), 10658–10669.

(166) Substitution of $[Co(II)(OH_2)_6](ClO_4)_2$ or $[Co(II)(OH_2)_6](PF_6)_2$ into the analogous conditions reactions for isolation of $\mathbf{F^1}$, $\mathbf{F^2}$ and **3** did not lead to any isolable product to date, thus suggesting (in the latter case) that P–F bond cleavage does not occur under the tested conditions.

(167) Fenton, H.; Tidmarsh, I. S.; Ward, M. D. *Dalton Trans.* **2009**, No. 21, 4199–4207.

(168) Lumsden, S. E. A.; Durgaprasad, G.; Thomas Muthiah, K. A.; Rose, M. J. *Dalt. Trans.* **2014**, *43* (28), 10725–10738.

(169) Zhu, Q.; Nelson, K. J.; Shum, W. W.; DiPasquale, A.; Rheingold, A. L.; Miller, J. S. *Inorg. Chim. Acta* **2009**, *362* (2), 595–598.

(170) Reedijk, J.; Jansen, J. C.; van Koningsveld, H.; van Kralingen, C. G. *Inorg. Chem.* **1978**, *17* (7), 1990–1994.

(171) Vela, J.; Smith, J. M.; Yu, Y.; Ketterer, N. a.; Flaschenriem, C. J.; Lachicotte, R. J.; Holland, P. L. *J. Am. Chem. Soc.* **2005**, *127* (21), 7857–7870.

(172) Rietmeijer, F. J.; De Graaff, R. A. G.; Reedijk, J. *Inorg. Chem.* **1984**, *23* (5), 151–156.

(173) Lee, S. C.; Holm, R. H. *Inorg. Chem.* **1993**, *32* (22), 4745–4753.

(174) Humphrey, S. M.; Weldon, G. F.; Wood, P. T. *J. Nanosci. Nanotechnol.* **2010**, *10* (1), 34–48.

(175) Figgis, B. N. *Introduction to Ligand Fields*; Interscience Publishers, 1966.

(176) Altomare, A.; Burla, M. C.; Camalli, M.; Cascarano, G. L.; Giacovazzo, C.; Guagliardi, A.; Moliterni, A. G. G.; Polidori, G.; Spagna, R. *SIR2004.* A program for crystal structure solution. *J. Appl. Cryst.*, **2005**, *38*, 381-388.

(177) Hiromoto, T.; Warkentin, E.; Moll, J.; Ermler, U.; Shima, S. *Angew. Chemie Int. Ed.* **2009**, *48* (35), 6457–6460.

(178) Shima, S.; Vogt, S.; Göbels, A.; Bill, E. *Angew. Chemie - Int. Ed.* **2010**, *49* (51), 9917–9921.

(179) Turrell, P. J.; Wright, J. A.; Peck, J. N. T.; Oganesyan, V. S.; Pickett, C. J. *Angew. Chemie - Int. Ed.* **2010**, *49* (41), 7508–7511.

(180) Chen, D.; Scopelliti, R.; Hu, X. *Angew. Chemie - Int. Ed.* **2011**, *50* (25), 5671–5673.

(181) Wodrich, M. D.; Hu, X. *Eur. J. Inorg. Chem.* **2013**, *2013* (22–23), 3993–3999.

(182) Hu, B.; Chen, D.; Hu, X. *Chem. - A Eur. J.* **2014**, *20* (6), 1677–1682.

(183) Shima, S.; Chen, D.; Xu, T.; Wodrich, M. D.; Fujishiro, T.; Schultz, K. M.; Kahnt, J.; Ataka, K.; Hu, X. *Nat. Chem.* **2015**, *7* (12), 995–1002.

(184) He, L.-P.; Chen, T.; Gong, D.; Lai, Z.; Huang, K.-W. *Organometallics* **2012**, *31* (14), 5208–5211.

(185) Chen, T.; He, L.-P.; Gong, D.; Yang, L.; Miao, X.; Eppinger, J.; Huang, K.-W. *Tetrahedron Lett.* **2012**, *53* (33), 4409–4412.

(186) He, L.-P.; Chen, T.; Xue, D.-X.; Eddaoudi, M.; Huang, K.-W. *J. Organomet. Chem.* **2012**, *700*, 202–206.

(187) Min, S.; Rasul, S.; Li, H.; Grills, D. C.; Takanabe, K.; Li, L. J.; Huang, K.-W. *Chempluschem* **2016**, *81* (2), 166–171.

(188) Song, L.-C.; Zhao, G.-Y.; Xie, Z.-J.; Zhang, J.-W. *Organometallics* **2013**, *32* (9), 2509–2512.

(189) Chen, D.; Scopelliti, R.; Hu, X. *Angew. Chemie - Int. Ed.* **2012**, *51* (8), 1919–1921.

(190) Bart, S. C.; Lobkovsky, E.; Chirik, P. J. *J. Am. Chem. Soc.* **2004**, *126* (42), 13794–13807.

(191) Lagaditis, P. O.; Sues, P. E.; Sonnenberg, J. F.; Wan, K. Y.; Lough, A. J.; Morris, R. H. *J. Am. Chem. Soc.* **2014**, *136* (4), 1367–1380.

(192) Seo, J.; Kerns, S. A.; Sullivan, E.; Rose, M. J. *Submitted to J. Am. Chem. Soc.*; 2018.

(193) Xie, Z.-L.; Durgaprasad, G.; Ali, A. K.; Rose, M. J. *Dalt. Trans.* **2017**, 10814–10829.

(194) Durgaprasad, G.; Xie, Z.-L.; Rose, M. J. *Inorg. Chem.* **2016**, *55* (2), 386–389.

(195) Xu, T.; Yin, C. J. M.; Wodrich, M. D.; Mazza, S.; Schultz, K. M.; Scopelliti, R.; Hu, X. *J. Am. Chem. Soc.* **2016**, *138* (10), 3270–3273.

(196) Song, L.; Xu, K.; Han, X.; Zhang, J. *Inorg. Chem.* **2016**, *55*, 1258−1269.

(197) Hu, B.; Chen, X.; Gong, D.; Cui, W.; Yang, X.; Chen, D. *Organometallics* **2016**, *35*, 2993–2998.

(198) Zhao, D.; Xu, Y.; Guo, Y.; Song, H.; Tang, L. *J. Organomet. Chem.* **2015**, *791*, 303–310.

(199) Turrell, P. J.; Hill, A. D.; Ibrahim, S. K.; Wright, J. A.; Pickett, C. J. *Dalt. Trans.* **2013**, *42*, 8140–8146.

(200) Kalz, K. F.; Brinkmeier, A.; Dechert, S.; Mata, R. A.; Meyer, F. *J. Am. Chem. Soc.* **2014**, *136* (47), 16626–16634.

(201) Speiser, F.; Braunstein, P.; Saussine, L. *Organometallics* **2004**, *23* (11), 2633–2640.

(202) Larson, S. B.; Simonsen, S. H.; Martin, G. E.; Smith, K.; Puig-Torres, S. *Acta Crystallogr. Sect. C Cryst. Struct. Commun.* **1984**, *C40* (1), 103–106.

(203) Lovell, J. M.; Beddoes, R. L.; Joule, J. A. *Tetrahedron* **1996**, *52* (13), 4745–4756.

(204) Sheikh, M. C.; Iwasawa, T.; Nakajima, A.; Kitao, A.; Tsubaki, N.; Miyatake, R.; Yoshimura, T.; Morita, H. *Synth.* **2014**, *46* (1), 42–48.

(205) Ogawa, S.; Muraoka, H.; Sato, R. *Tetrahedron Lett.* **2006**, *47* (15), 2479–2483.

(206) Fairlamb, I. J. S.; Marrison, L. R.; Dickinson, J. M.; Lu, F. J.; Schmidt, J. P. *Bioorganic Med. Chem.* **2004**, *12* (15), 4285–4299.

(207) Demuner, A. J.; Valente, V. M. M.; Barbosa, L. C. A.; Rathi, A. H.; Donohoe, T. J.; Thompson, A. L. *Molecules* **2009**, *14* (12), 4973–4986.

# Vita

Yae In Cho was born in Daegu, South Korea, and mostly raised in Busan, South Korea. Before attending The University of Texas at Austin, she attended Pusan National University, Busan, South Korea, where she earned a Bachelor of Science in Chemistry, with summa cum laude, in 2012. She joined Rose research group in 2012 as the first member of the group.

Permanent address (or email): yaeincho@gmail.com

This dissertation was typed by the author.